

Growth, magnetic properties and interface effects of Fe and Fe-oxide ultrathin films on BaTiO₃(001) substrates

Dissertation

zur Erlangung des akademischen Grades
Doctor rerum naturalium (Dr. rer. nat.)

vorgelegt von

Remya Kunjuveetil Govind

geboren am 06.03.1984
in Thiruvalla, Kerala, Indien



am Institut für Physik
der Naturwissenschaftlichen Fakultät II
der Martin-Luther-Universität Halle-Wittenberg

Zweite überarbeitete Version

Gutachter:

1. PD Dr. Karl-Michael Schindler
Martin-Luther-Universität Halle-Wittenberg
2. Prof. Dr. Kathrin Dörr
Martin-Luther-Universität Halle-Wittenberg
3. Prof. Dr. Clemens Laubschat
Technische Universität Dresden

Eröffnung des Promotionsverfahrens: 17. Juli 2013

Öffentliche Verteidigung: 27. November 2013

To the sweet memories
of my dearest Achan

Contents

List of figures	8
List of tables	9
1 Introduction	11
2 Theoretical aspects of main experimental techniques	15
2.1 X-ray absorption spectroscopy	15
2.1.1 Measurement methods	19
2.2 X-ray magnetic circular dichroism	20
2.2.1 Analysis of XMCD spectra	22
2.3 X-ray magnetic linear dichroism	24
2.4 X-ray photoemission spectroscopy	24
3 Experimental	27
3.1 Experimental apparatus and techniques	27
3.2 Materials and methods of preparation	33
3.2.1 BaTiO ₃ (001)	33
3.2.2 Fe	34
3.2.3 Fe ₃ O ₄	35
4 Growth and magnetism of Fe films on BaTiO₃(001)	37
4.1 Introduction	37
4.2 Characterisation of BaTiO ₃ (001)	39
4.2.1 Low-energy electron diffraction investigations	39
4.2.2 X-ray absorption spectroscopy studies	41
4.2.3 Resonant photoemission spectroscopy measurements	43
4.3 Growth of ultrathin Fe films on BaTiO ₃ (001)	47
4.3.1 Results of LEED investigations	47
4.3.2 Interface stability	49
4.4 Investigations of Magnetic properties	52
4.4.1 Thickness dependence	52
4.4.2 Direction dependence	58
4.4.3 Magnetization loops	64
4.4.4 Temperature Dependence	65

4.4.5	Induced magnetic moments at Ti atoms	67
4.5	Conclusions	68
5	Fabrication and magnetism of ordered Fe islands on BaTiO₃(001)	71
5.1	Introduction	71
5.2	Effect of annealing the Fe film: Morphological changes	72
5.2.1	Auger electron spectroscopy	72
5.2.2	Faceting: LEED investigations	74
5.2.3	SEM and EDX spectroscopy investigations	76
5.3	Interface effects	81
5.4	Magnetic properties of Fe islands	82
5.4.1	Magneto-Optic Kerr Effect	82
5.4.2	X-ray Magnetic Circular Dichroism	84
5.5	Conclusions	88
6	Growth and magnetic properties of Fe ultrathin films on BaTiO₃ layers	89
6.1	Introduction	89
6.2	Characterization of BaTiO ₃ (100) layers	90
6.3	Investigation of interface stability	94
6.4	Magnetic properties of Fe films on BaTiO ₃ (100)/Pt(100)	96
6.4.1	Thickness dependence	96
6.4.2	Azimuthal angle dependence	99
6.5	Conclusions	103
7	Growth and magnetic properties of ultrathin Fe₃O₄ films on BaTiO₃(001)	105
7.1	Introduction	105
7.2	Fe ₃ O ₄ thin films on BaTiO ₃ (001) studied with XAS	106
7.3	Magnetic properties of Fe ₃ O ₄ films	108
7.3.1	Effect of annealing and oxygen pressure	109
7.3.2	Magnetic anisotropy	111
7.3.3	Thickness dependence	112
7.3.4	XMLD	114
7.4	Conclusions	116
8	Summary and future perspectives	117
	Literature	121

List of Figures

2.1	Schematic of X-ray absorption	17
2.2	Schematic of fluorescence decay and X-ray photoelectron ejection	18
2.3	Schematic representation of XMCD	21
2.4	Illustration of spin and orbital magnetic moment calculation procedure .	23
3.2	Experimental geometry of XMCD measurements	32
3.3	Structure model of BaTiO ₃	33
3.4	Schematic of samples investigated	35
4.1	Structure model and LEED images of a clean BaTiO ₃ (001) single crystal surface	40
4.2	X-ray absorption spectra measured from a BaTiO ₃ (001) single crystal . .	42
4.3	RPES of BaTiO ₃ obtained with Ti 2 <i>p</i> core level energies	44
4.4	XAS at Ti <i>L</i> _{2,3} edges compared to RPES intensity enhancement spectra .	47
4.5	Structure model and LEED images of Fe films on BaTiO ₃ (001)	48
4.6	XAS measurements from Fe/BaTiO ₃ (001)	50
4.7	Thickness dependence of Fe 2 <i>p</i> X-ray photoemission spectra	51
4.8	Fe <i>L</i> _{2,3} XAS and XMCD spectra measured from a 5.3 MLE Fe film	53
4.9	XAS and XMCD spectra of a 10.6 MLE Fe film	54
4.10	Thickness dependence of XMCD spectra	55
4.11	Direction dependence of XMCD asymmetry	59
4.12	Variation of Fe <i>L</i> _{2,3} XMCD as a function of film thickness	60
4.13	Magnetization curves	64
4.14	Temperature dependence of XMCD	66
4.15	XAS and XMCD spectra at Ti <i>L</i> _{2,3} edges	68
5.1	Auger electron spectra of an 8 MLE Fe film	73
5.2	LEED images obtained from 26 MLE Fe film after annealing	74
5.3	LEED images obtained from 8 MLE Fe film after annealing	75
5.4	SEM images obtained from a 26 MLE Fe film	77
5.5	SEM image recorded from the 773 K annealed Fe film	78
5.6	EDX spectra	78
5.7	SEM images obtained after annealing to 973 K	79
5.8	SEM image and schematic of a representative Fe nanoisland	80
5.9	Interface stability investigated with XA spectra	81

5.10	MOKE loops of Fe film on BaTiO ₃ as a function of annealing temperature	83
5.11	Variation of the coercive field and Kerr ellipticity upon annealing	83
5.12	(a) XAS and (b) XMCD spectra at Fe $L_{2,3}$ edges	85
6.1	XA spectra of the (a) Ti $L_{2,3}$, (b) Ba $M_{4,5}$ and (c) O K edges of BaTiO ₃ layers	91
6.2	XA spectra measured after evaporation of Fe layers on BaTiO ₃ /Pt	95
6.3	The XAS and XMCD spectra measured at the Fe $L_{2,3}$ edges of an 8 MLE Fe film	97
6.4	Thickness dependence of XMCD of Fe films on BaTiO ₃ /Pt	98
6.5	SRT studied by azimuthal angle dependence of XMCD	100
7.1	XAS at the (a) Fe $L_{2,3}$ and (b) O K edges from an Fe ₃ O ₄ film	107
7.2	XAS at the Fe $L_{2,3}$ edges published in literature	108
7.3	XAS at the (a) Ti $L_{2,3}$ and (b) Ba $L_{4,5}$ edges	109
7.4	Effect of annealing and oxygen pressure	110
7.6	Thickness dependence of XMCD.	113
7.7	Fe $L_{2,3}$ XAS and XMLD spectra of a 2.6 nm Fe ₃ O ₄ film	115

List of Tables

4.1	Thickness dependence of magnetic moments of Fe films on BaTiO ₃ . . .	56
4.2	Direction dependence of magnetic moments of Fe films on BaTiO ₃ estimated as a function of thickness	61
4.3	Direction dependence of calculated effective spin and orbital moments of Fe films on BaTiO ₃	61
4.4	Calculated effective spin and orbital moments of Fe thin films	63
4.5	Magnetic moments calculated from XMCD measurements at 150 K . . .	66
5.1	Dependence of magnetic moments on the annealing temperature	85
6.1	Features and associated energies at the Ti $L_{2,3}$ edges	91
6.2	Features and associated energies at the Ba $M_{4,5}$ edges	92
6.3	Features and associated energies at the O K edge	92
6.4	Thickness dependence of magnetic moments in the Fe films on BaTiO ₃ /Pt	98
6.5	Azimuthal angle dependence of magnetic moments in a 6.5 MLE Fe film on BaTiO ₃ /Pt	101
6.6	Azimuthal angle dependence of magnetic moments in an 8.5 MLE Fe film on BaTiO ₃ /Pt	101
7.1	Magnetic moments per Fe atom calculated from Fe ₃ O ₄ films on BaTiO ₃ .	114

1 Introduction

Magnetic materials play an inevitable role in modern day information technology due to the applications in sensors, memories, read heads etc. Progress in these fields require size reduction along with the exploration of new properties. Reduction in size and dimensions of magnetic materials can lead to significant improvement in properties along with constraints for a perfect control of their fabrication. Dimension reductions such as from bulk to thin films induce the presence of interfaces, surfaces and structural defects, that can act as the origin of new magnetic configurations. Magnetic films in the ultrathin size regime behave as two-dimensional magnetic systems and give rise to modified magnetic properties due to the reduction in dimensions and symmetry and hence they are strongly correlated to morphology, dimension and thickness. The knowledge about local structural, chemical and magnetic properties of these objects is essential in optimizing their characteristics.

The aim of this thesis is to investigate the growth, the interface effects and the magnetic properties of ultrathin ferro- and ferrimagnetic films on ferroelectric substrates such as BaTiO_3 . These systems are examples of two-phase materials which offer the possibility to combine desired ferroic properties and are expected to show a multiferroic effect due to the coupling of different ferroic orders across the interface.

Suitable experimental methods employed in this thesis to study the interface electronic structure and magnetic properties in thin film magnetic materials are X-ray absorption spectroscopy (XAS) and X-ray magnetic circular dichroism (XMCD) due to the surface sensitivity and elemental specificity combined with the possibility of the quantitative determination of orbital and spin magnetic moments especially of individual constituents in a compound [1, 2, 3, 4, 5, 6, 7]. The improvement of data evaluation techniques and advances at the theoretical front have helped in the successful implementation of XAS and XMCD for the determination of magnetic properties.

The focus of the first part of this thesis is on the growth, interface effects and magnetic properties of ultrathin Fe films on well characterized single crystal $\text{BaTiO}_3(001)$ substrates. The effect of the substrate surface structure on the oxidation and magnetic properties of Fe ultrathin films will be addressed in this part. In addition, the effect of growth as well as film thickness on the magnetic properties will also be established. A magnetoelectric effect induced by interface bonding was predicted across Fe/ BaTiO_3 multilayers [8] and ferroelectric control of magnetism was later demonstrated across a BaTiO_3/Fe interface [9]. A ferromagnetic-to-ferrimagnetic transition of magnetic order with increasing Fe thickness has been predicted with first-principles

electronic-structure calculations of Fe films on TiO_2 terminated surfaces of BaTiO_3 or PbTiO_3 [10]. A similar effect has also been found in first principles XMCD calculations of Fe ultrathin films on BaTiO_3 where characteristic structures were observed in the XMCD spectra and attributed to changes at the Fe/ BaTiO_3 interface structure [11]. These predictions serve as the motivation to investigate the magnetic properties of Fe ultrathin films on BaTiO_3 surfaces experimentally.

Since the magnetic properties of thin films are closely related to the structure and morphology, any change in these properties will lead to changes in magnetism. This particularly interesting aspect in the study of thin films, i.e., the effect of annealing on the morphology and magnetic properties will be addressed in the second part.

The substitution of single crystal BaTiO_3 substrates with BaTiO_3 layers will be beneficial for multiferroic switching applications due to the comparatively low voltages required for switching the polarization of BaTiO_3 layers. Knowledge of the magnetic properties of Fe films on BaTiO_3 layers is therefore essential in successfully employing these materials for technological applications and this forms the focus of the third part. The reported switching of Ni magnetization in Ni/ BaTiO_3 hybrid structures using the electric field dependence of the magnetic coercivity [12] makes the study of magnetic properties of Fe on $\text{BaTiO}_3/\text{Pt}(100)$ interesting since magnetoelectric coupling is predicted due to a polarization-induced change in the magnetization at the interface in this system [13]. Magnetic properties and the interface stability of Fe ultrathin films on BaTiO_3 layers will be investigated in this part in order to compare it to the Fe films on BaTiO_3 single crystals.

The effect of BaTiO_3 substrate and interface interaction on the magnetic properties if the magnetic layer is ferrimagnetic, forms the focus of the final part. The suggested magnetoelectric effect at the $\text{Fe}_3\text{O}_4/\text{BaTiO}_3$ interface due to interface bonding [14] is motivational to study the magnetic properties and interface effects of Fe_3O_4 ultrathin films on BaTiO_3 single crystals.

The present thesis is organized into eight chapters. The next chapter describes the theoretical aspects concerning the main experimental techniques employed in this thesis. Chapter 3 provides a description of the experimental apparatus and methods along with a brief description of materials investigated and their methods of preparation. Experimental results are presented and discussed in the next four chapters. In the first part of chapter 4, the detailed investigations on the electronic structure and long range order of BaTiO_3 single crystal substrates are presented. In the second part of chapter 4, the growth and magnetic properties of ultrathin Fe films on BaTiO_3 single crystal substrates are studied which elucidate the thickness dependent in-plane spin reorientation transition. In chapter 5, the dependence of magnetic properties on the morphological transformations of Fe film due to annealing is shown. Chapter 6 presents the results of magnetic property investigations of Fe films on BaTiO_3 layer substrate and thickness dependent spin reorientation transition of Fe films. The final results chapter (chapter 7) focuses on the growth and magnetic properties of e-beam evaporated Fe oxide

ultrathin films. Chapter 8 discusses the summary of the present work with a future outlook.

2 Theoretical aspects of main experimental techniques

In this chapter, the theoretical aspects of the main experimental techniques employed in this thesis such as X-ray absorption spectroscopy (XAS), X-ray magnetic circular dichroism (XMCD), X-ray Magnetic Linear Dichroism (XMLD) and X-ray photoelectron spectroscopy (XPS) are briefly described.

2.1 X-ray absorption spectroscopy

When an electromagnetic radiation, with oscillating electric and magnetic fields, such as X-rays hit a sample, the electric field of the radiation interacts with the electrons of the atoms. Consequently, the incident X-rays may get absorbed through the excitation of the electrons in the sample or get scattered elastically or inelastically.

Upon interaction of X-rays with matter, the X-ray intensity I decays exponentially as given by Beer's law:

$$I_d = I_0 e^{-\mu d} \quad (2.1)$$

where d is the depth of the sample, I_0 is the incident intensity, I_d is the attenuated intensity after the radiation passes through the sample and μ stands for the linear X-ray absorption coefficient.

The X-ray absorption cross section σ is defined as the number of photons absorbed per atom divided by the number of incident photons per unit area. The absorption coefficient is related to the absorption cross section via $\sigma = \mu / \rho$, where ρ is the density of atoms.

X-ray absorption spectroscopy measures the excitation of an electron from the deep core state to a previously unoccupied bound state or the continuum. If we consider the excitation of a core electron with an initial state $|i\rangle$ and energy E_i to a final state $|f\rangle$, by the absorption of an X-ray photon with energy $E = \hbar\omega$, the final state has an energy $E_f = E_i + \hbar\omega$.

The absorption cross section in a photoelectric absorption process (σ_a) is defined as the ratio of the transition rate (electron transition probability per unit time) to the incident flux of photons.

$$\sigma_a = W_{i \rightarrow f} / \Phi_0 \quad (2.2)$$

where, $W_{i \rightarrow f}$ is the transition probability per unit time [sec^{-1}] and Φ_0 is the incident photon flux [number of photons/ cm^2s].

In first order time dependent perturbation theory, the transition probability per unit time $W_{i \rightarrow f}$, from a state $|i\rangle$ to a state $|f\rangle$ is described by Fermi's Golden rule:

$$W_{i \rightarrow f} = \frac{2\pi}{\hbar} |\langle f | T_{i \rightarrow f} | i \rangle|^2 \delta(E_f - E_i - \hbar\omega) \quad (2.3)$$

where $T_{i \rightarrow f}$ denotes the interaction operator and $\delta(E_f - E_i - \hbar\omega)$ is the energy conservation term. In the first order the interaction operator $T_{i \rightarrow f}$ is equal to the interaction Hamiltonian \mathcal{H}_{int} . Thus the probability of transitions per unit time of the system due to perturbations from one energy Eigen state into a continuum of energy Eigen states can be calculated using equation 2.3.

For X-ray absorption, \mathcal{H}_{int} couples the electron and photon fields and hence consists of the product of the electron momentum operator \mathbf{p} and the vector potential \mathbf{A} (of X-rays). With m_e the mass of electron, c the velocity of light and e the electron charge ,

$$\mathcal{H}_{int} = \frac{e}{m_e c} \mathbf{p} \cdot \mathbf{A} \quad (2.4)$$

The vector field for the X-rays \mathbf{A} is given in the form of a plain wave of electromagnetic radiation which can be written as [15],

$$\mathbf{A} = \mathbf{e}_q A_0 \cos(kx - \omega t) = \frac{1}{2} \mathbf{e}_q A_0 e^{i(kx - \omega t)} + c.c. \quad (2.5)$$

where \mathbf{e}_q is the unit vector for polarization \mathbf{q} , \mathbf{k} is the wave vector, x is the displacement, ω is the frequency and t is the time.

By substituting for \mathbf{A} in Equation. 2.4, the interaction Hamiltonian can be obtained as [15],

$$\mathcal{H}_{int} \propto \sum_q (\mathbf{e}_q \cdot \mathbf{p}) e^{i\mathbf{k} \cdot \mathbf{r}} \quad (2.6)$$

By doing a Taylor expansion of $e^{i\mathbf{k} \cdot \mathbf{r}}$ and neglecting further terms after the second term, the first two terms of the \mathcal{H}_{int} become [15],

$$\mathcal{H}_{int} \propto \sum_q [(\mathbf{e}_q \cdot \mathbf{p}) + i(\mathbf{e}_q \cdot \mathbf{p})(\mathbf{k} \cdot \mathbf{r})] \quad (2.7)$$

The first term of Equation 2.7 refers to the dipole transition and second term gives the electric quadrupole transition. In this equation, the \mathbf{k} dependence can be eliminated by neglecting further terms of the expansion. \mathbf{p} can be expressed in terms of the length operator \mathbf{r} as $\mathbf{p} = m/i\hbar[\mathbf{r}, \mathcal{H}]$ where \mathcal{H} is the atomic Hamiltonian.

Hence, the \mathcal{H}_{int} finally takes the form [15],

$$\mathcal{H}_{int} \propto \sum_q (\mathbf{e}_q \cdot \mathbf{r}) \quad (2.8)$$

By substituting for \mathcal{H}_{int} in Fermi's Golden rule (Eq. 2.3) gives,

$$T_{if} \propto \frac{2\pi}{\hbar} |\langle f | (\mathbf{e}_q \cdot \mathbf{r}) | i \rangle|^2 \delta(E_f - E_i - \hbar\omega) \quad (2.9)$$

This equation gives the transition probability of electrons in polarization dependent X-ray absorption per unit time in the dipole approximation in the most general form. Using this equation, the absorption cross sections can be calculated by knowing the incident photon flux.

A schematic of X-ray absorption process is shown in Fig. 2.1. The X-rays with an energy, $E = \hbar\omega$ excite an electron from the core levels to the unoccupied states as shown in Fig. 2.1.

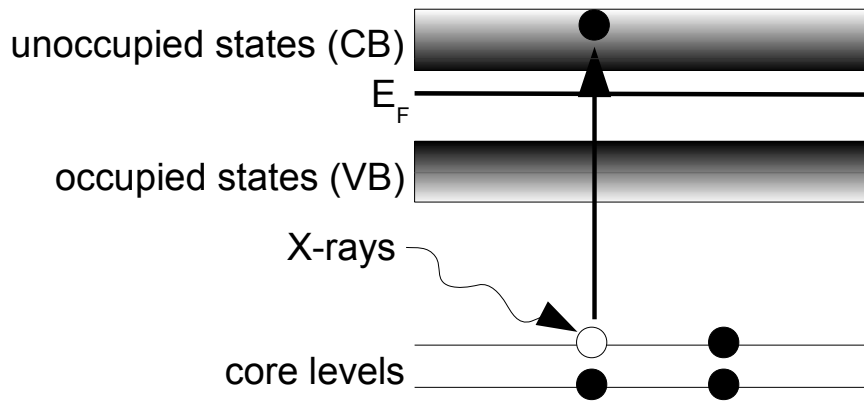


Figure 2.1: Schematic of X-ray absorption.

The creation of the core hole leaves the atom in a highly excited state. The relaxation of core holes occur via radiative or non-radiative processes. Auger electron spectroscopy is based on the non-radiative decay of core holes while X-ray emission spectroscopy is based on the radiative decay of core holes. In the radiative decay, an electron from a higher subshell compensates the core hole and the corresponding energy difference is emitted as a photon possessing a different energy than the incoming X-ray photon [15].

In Auger electron decay, the core hole is filled by an electron from a higher subshell and the resultant energy difference is transferred to another electron in the atom, which gets ejected. Hence the final state consists of two holes after the Auger electron emission. But, in this case, the final state has a lower energy than the initial state (after X-ray absorption) which had one hole in the core level [15]. An Auger process is named according to the shells involved, for example, the *LMM* Auger transition involves the initial core hole in the *L* shell, relaxation of an electron from an *M* shell and consequent ejection of electron from the *M* shell. The creation of a photoelectron which forms the basis for X-ray photoelectron spectroscopy as well as Auger electron emission and fluorescence emission are schematically depicted in Fig. 2.2. The kinetic energy of an emitted Auger electron is independent of the initial excitation energy. Auger processes

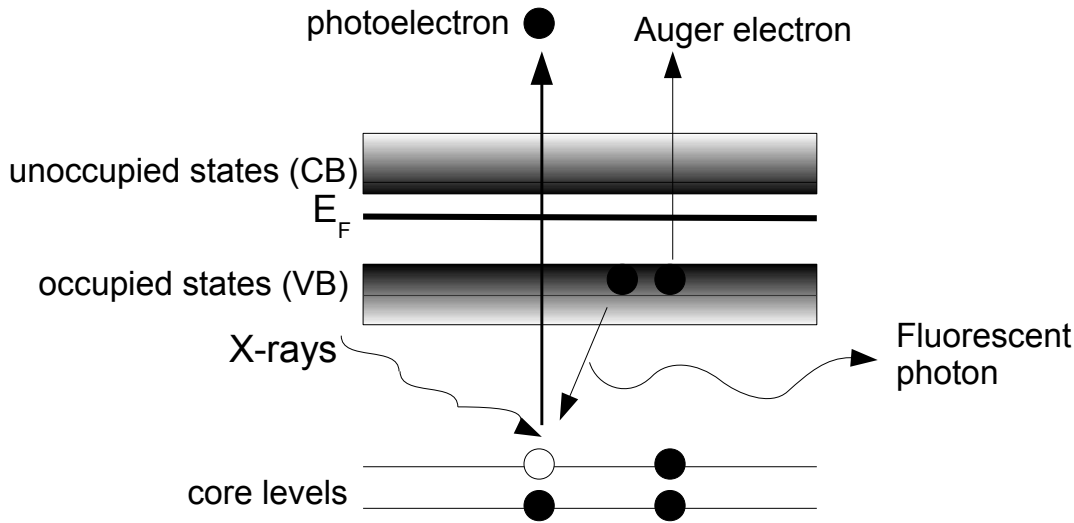


Figure 2.2: Schematic representation of fluorescence decay, Auger electron emission and X-ray photoelectron ejection.

in which the initial core hole as well as the relaxing electron have the same principal quantum number are termed as Coster-Kronig (CK) and super-Coster-Kronig (sCK) Auger transitions.

The photoabsorption transitions are governed by selection rules and the final states can be found out for different transitions using selection rules. The dipole selection rules for the photoabsorption electric dipole transitions are: $\Delta l = \pm 1$, $\Delta s = 0$, $\Delta j = 0, \pm 1$ and $\Delta m_l = +1$ for left circular polarization, $\Delta m_l = -1$ for right circular polarization and $\Delta m_l = 0$ for linear polarization of light, where l is the orbital angular momentum quantum number, s is the spin quantum number, m_l is the magnetic quantum number and j is the total angular momentum quantum number. Examples of allowed transitions for $3d$ metals include $2p \rightarrow 3d, 4s$. Selection rules for quadrupole transitions allow $\Delta L = \pm 2, 0$, but these transitions are much weaker than the dipole transitions.

X-ray absorption spectrum In X-ray absorption spectroscopy, the absorption cross sections are plotted as a function of absorbed photon energy. At certain photon energies, the absorption increases considerably compared to the background. These energies are termed as absorption edges. The absorption edges are named according to the quantum number of the core hole produced in the transition [15].

An X-ray absorption spectrum is generally divided into four regions depending on the energy. The first one is the pre-edge region, with $E < E_0$, where E is the energy

of the incident beam and E_0 is the energy at the absorption edge. The features in the pre-edge region usually have only small intensities and are attributed to electron transitions from the core level to the higher unfilled or half-filled orbitals (e.g., $s \rightarrow p$, or $p \rightarrow d$).

X-ray absorption near edge structure (XANES) occurs in the energy range given by $E = E_0 \pm 10 \text{ eV}$. The features in this region result from the transitions of core electrons to unoccupied energy levels. Another region is near edge X-ray absorption fine structure (NEXAFS), which is 10 eV up to 50 eV above the edge ($E - E_0$ is small) and occurs due to the multiple scattering of ejected photoelectrons by atoms of the first and higher coordinating shells. The extended X-ray absorption fine structure (EXAFS) starts approximately from 50 eV and continues up to 1000 eV ($E - E_0$ is large) above the edge. This energy region is dominated by single scattering of the photoelectrons by the nearest neighbouring atoms.

2.1.1 Measurement methods

Three most important methods are employed for detection of X-ray absorption in solids and they are transmission, X-ray fluorescence and electron yield (EY). In transmission method, X-rays are transmitted through the sample and due to the loss of photons through core electron excitation to empty states, the transmitted X-ray intensity drops at the absorption edge. This method is best suited for the studies of thin foils [16].

Fluorescence yield method is based on the fluorescence decay of the core hole. Fluorescence decay is already shown in Fig. 2.2 and described therein. The core holes produced after absorption are filled by valence electrons accompanied by the emission of photons. For core levels below 1 keV, Auger decay is predominant and fluorescence decay increases with further increase in energy. Thus, for 3d metals, the core levels are dominated by Auger decay and K edges show strong fluorescence decay. This method is not well suited especially for the study of surfaces because the photon created as the result of fluorescence decay has a mean free path of the same order as that of the incoming X-ray, thus the surface effects are mostly excluded [15].

In the electron yield (EY) method, the absorbed photons create core holes that are filled by Auger electron emission. The total number of emitted electrons is directly proportional to the absorption probability. The emitted electron yield can be simply measured as a current with an ammeter which measures the electrons flowing back to the sample from ground. EY detection directly gives a spectrum that is proportional to the X-ray absorption coefficient or the absorption cross-section because the yield is directly proportional to the probability of X-ray absorption. This method is well suited for measurements on surfaces because of the high sensitivity to the near surface region and layers. In total electron yield (TEY), all electrons emerging from the sample are detected and since the electrons interact more strongly with solids than X-rays do, the

electrons emerging out are more from the surface. The probing depth of total electron yield depends on the material studied and is typically in the range of 3-10 nm [15].

In EY, the energy of the escaped electrons can be detected with the help of an electron energy analyzer and this is known as partial electron yield (PEY) detection. PEY is found to be surface sensitive especially below 1 keV which is due to electron scattering and this also gives less background compared to TEY. The detection method chosen for the experiments described in this thesis is total electron yield (TEY) since the experiments deal with the surface layers of the sample. The consistency of TEY measurements was checked by measuring in partial electron yield (PEY) also. It is observed that the two methods yield similar results.

2.2 X-ray magnetic circular dichroism

In magnetic metals, a difference in majority and minority valence spin states exist. This spin polarization of unoccupied states created due to the exchange interaction in the valence states leads to an energetic shift between the two partial densities of states. By using a spin dependent absorption process, the measurement of intensity difference corresponding to the difference between the number of spin-up and spin-down holes, i.e., the magnetic moment, is feasible. This forms the basis for XMCD spectroscopy [16].

X-ray magnetic circular dichroism is defined as the difference in absorption for left and right circularly polarized X-rays due to the magnetism of the sample and can be represented as [16],

$$\Delta I = I_{\uparrow\downarrow} - I_{\uparrow\uparrow} \quad (2.10)$$

In the simplest approach, a one-electron model where the valence states exhibit a Stoner splitting (due to exchange interaction) along with a two-step approach can be used to understand XMCD. In the first step, circularly polarized X-rays interact with magnetic material producing spin polarized photoelectrons from a localized atomic inner shell of the material with a spin and orbital momentum as a consequence of the conservation of angular momentum of the incident X-rays. In the second step, the spin split valence state serves as the detector for the spin of the excited photoelectrons [16].

The XMCD effect depends mainly on three factors (1) degree of circular polarization (2) the expectation value of the magnetic moment of the 3d shell (3) the angle between the directions of the photon angular momentum and the magnetic moment [16].

The sample magnetization direction M and the photon spin or angular momentum are made collinear in order to obtain maximum XMCD effect. Experimentally, XMCD is measured either by changing the angular momentum of incoming light by keeping the magnetization constant or by fixing the X-ray photon spin direction and switching the magnetization direction of the sample. [16]

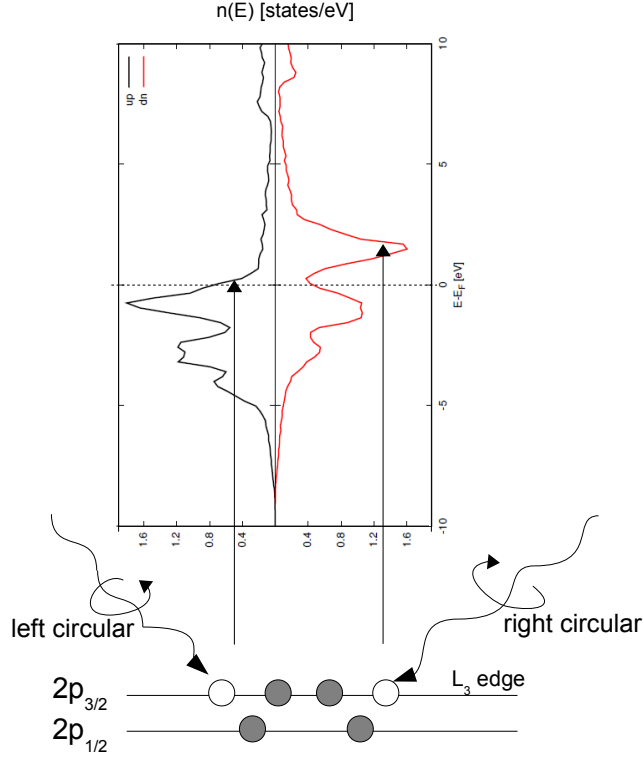


Figure 2.3: Schematic representation of the XMCD process at the $L_{2,3}$ edges of Fe as an example as described in [16]. Fe DOS is adopted from [11].

A schematic of XMCD is depicted in Fig. 2.3 with bulk Fe as an example. The $3d$ band in Fe is split into spin up and spin down bands as shown in Fig. 2.3. The circularly polarized X-rays produce spin polarized photoelectrons from the core level due to spin orbit coupling. The $3d$ valence states in Fe are spin split which act as a detector to the spin polarized photoelectrons. The different light polarizations probe different valence $3d$ states. At the Fe L_3 edge, the left circular light probes the spin up $3d$ states with respect to the direction of the magnetization which gets reversed for the L_2 edge due to the sign reversal of spin orbit coupling [16]. Hence a dichroism effect originates with different light polarizations.

XMCD spectroscopy can be used to evaluate the spin and orbital magnetic moments of magnetic materials with the application of sum rules. Sum rules are equations based on integrated spectra and for XMCD, it involves projections of the spin $\langle S_z \rangle$ and orbital $\langle L_z \rangle$ angular momentum of the absorbing species. According to the XMCD sum rules by Thole and Carra [17, 18], the orbital and spin moments of ferro and ferrimagnets can be determined from the XAS and XMCD spectra.

The sum rule for the orbital moment as derived by Thole and co-workers is given by [17],

$$\rho \equiv \frac{\int_{edge} d\omega (\mu^+ - \mu^-)}{\int_{edge} d\omega (\mu^+ + \mu^- + \mu^0)} = \frac{1}{2} \frac{c(c+1) - l(l+1) - 2}{l(l+1)(4l+2-n)} \langle L_z \rangle \quad (2.11)$$

where $4l + 2 - n$ represents the number of holes in the valence shell, $\mu^0 = (\mu^+ + \mu^-)/2$, μ^+ is the absorption spectra with the magnetic field parallel to the photon angular momentum vector.

The spin sum rule from Carra and co-workers is given as [18],

$$\delta = \frac{\int_{j+} d\omega(\mu^+ - \mu^-) - [(c+1)/c] \int_{j-} d\omega(\mu^+ - \mu^-)}{\int_{j++j-} d\omega(\mu^+ + \mu^- + \mu^0)} = \frac{l(l+1) - 2 - c(c+1)}{3c(4l+2-n)} \langle S_z \rangle + \frac{l(l+1)[l(l+1) + 2c(c+1) + 4] - 3(c-1)_2(c+2)_2}{6lc(l+1)(4l+2-n)} \langle T_z \rangle \quad (2.12)$$

2.2.1 Analysis of XMCD spectra

The orbital as well as spin moments of magnetic materials can be calculated from the integrated areas of XMCD and isotropic XAS according to the sum rules. The procedure of extraction of spin and orbital magnetic moments from the XMCD spectra according to Chen et al. [5] is explained in Fig. 2.4 using Fe $L_{2,3}$ edges XAS as well as XMCD spectra as an example. Figure 2.4(top) shows the photon flux normalized TEY absorption spectra of Fe films on BaTiO₃ measured at the Fe $L_{2,3}$ edges in grazing incidence. The difference spectrum (XMCD) is shown in Fig. 2.4(bottom) after correcting for the incomplete photon polarization as well as the angle of light incidence.

In order to make use of the equations in 2.11 and 2.12, the linear polarized spectral absorption cross section is required. It is calculated as $[\mu_+ + \mu_-]/2$, where μ_+ and μ_- are the absorption cross sections obtained with left and right circular polarizations of X-rays.

The integral for the whole range of L_2 and L_3 edges are determined from the integrated XMCD spectrum. This integral value is labelled as ' q '. The integration of L_3 edge alone is slightly erroneous since some of the L_3 signal might overlap with that of L_2 . However, the integral for L_3 is determined by placing the cut off at the onset of the L_2 white line. The value is labelled as ' p ' and is marked accordingly in Fig. 2.4.

L_2 and L_3 edge jumps are removed from the spectrum by a simple no parameter step function with the edge jumps in the step function placed at the maximal energy of the edges. The height of the edge jumps were in the ratio 2/3 (1/3) for $L_3(L_2)$ edges. The sum spectrum along with the edge jump to be removed and the integral are shown in Fig. 2.4(middle). The value obtained after integration of the sum spectra is termed as ' r ' and is shown in Fig. 2.4(middle).

For the results explained in this thesis, the 3d electron occupation number is assumed to be 6.61 for Fe based on theoretical calculations [19, 5]. By substituting the integral values as p , q and r in equations 2.11 and 2.12, the expressions for orbital and spin magnetic moments in 3d transition metals can be modified as,

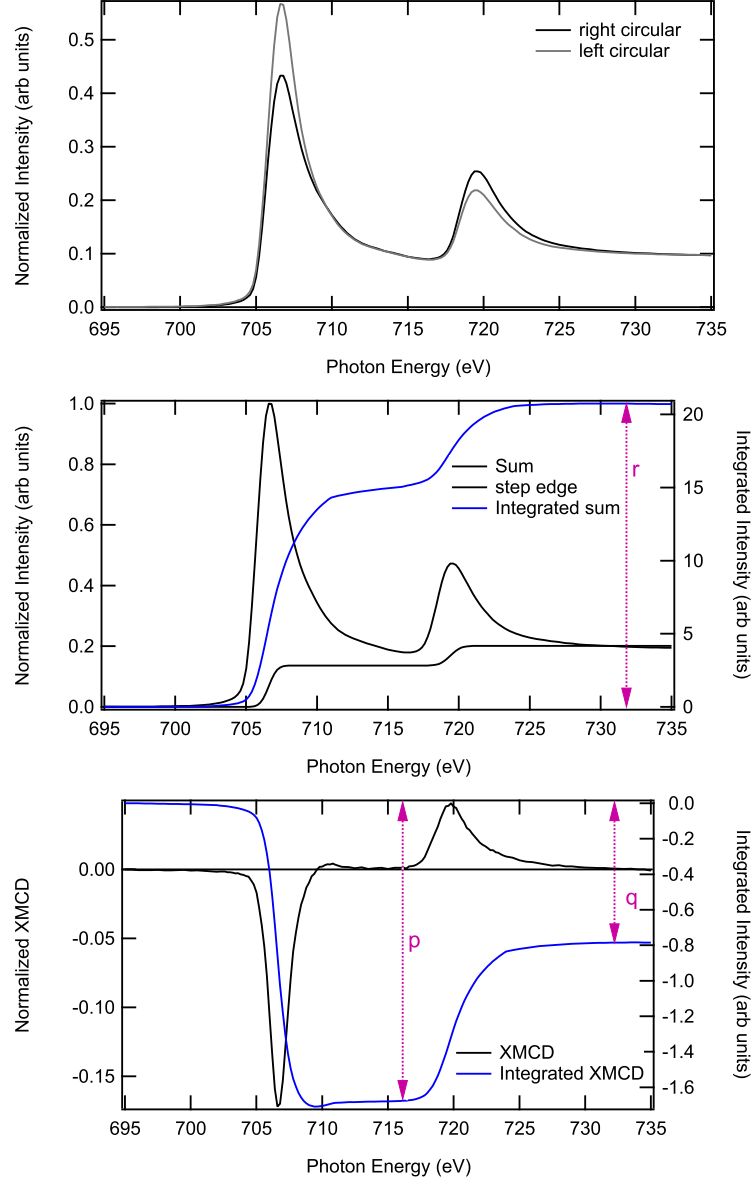


Figure 2.4: Illustration of spin and orbital magnetic moment calculation procedure as explained by Chen et al. [5]. Fe $L_{2,3}$ edge absorption spectra measured with different polarizations of light (top), resultant XAS spectra and integral (middle), resultant XMCD spectra and integral (bottom). The different labels p,q and r are explained in the text.

$$m_{orb} = -4q(10 - n_{3d})/3r \quad (2.13)$$

and,

$$m_{spin} = -(6p - 4q)(10 - n_{3d})/r \quad (2.14)$$

where n_{3d} is the electron occupation number in the valence shell.

This procedure for the calculation of magnetic moments shows excellent agreement with the predicted theoretical values as well as gyromagnetic measurements [5].

2.3 X-ray magnetic linear dichroism

X-ray magnetic linear dichroism effect is defined as the difference in X-ray absorption intensity with the electric vector of the linear polarized X-rays aligned parallel and perpendicular to the spin direction of the sample [16]. The XMLD difference intensity is given by,

$$\Delta I = I_{\parallel} - I_{\perp} \quad (2.15)$$

XMLD effect stems from the unequal spectral contribution from charge anisotropies induced by the exchange and spin–orbit interactions which cause a uniaxial spin alignment relative to the easy magnetic axis of a magnetically ordered sample. In XMLD effect, the measured anisotropy is the result of nonsymmetrical charge distribution around the absorbing atom. If the charge anisotropy is due to bonding alone it is termed as “natural” linear dichroism and when it has a magnetic origin it is called “magnetic” linear dichroism [16].

Experimentally, XMLD can be measured in two ways- (1) by using a fixed sample orientation relative to the linearly polarized X-rays and by rotating the magnetization of the sample between the easy and the hard directions by a sufficiently strong magnetic field (2) by magnetizing the sample along the easy axis and measuring the absorption with the easy axis either parallel or perpendicular to the X-ray electric field vector (E-vector) by rotating the E-vector relative to the sample or the sample relative to the E-vector [16]. The XMLD intensity depends on the expectation value of the square of the magnetic moment i.e., $\langle m^2 \rangle$ and hence can be very useful in the measurement of antiferromagnetic systems such as NiO and ferrimagnetic systems such as Fe_3O_4 .

2.4 X-ray photoemission spectroscopy

X-ray photoemission spectroscopy (XPS) is based on the photoelectric effect whereby monochromatic light such as X-rays cause emission of electrons upon interaction with a sample. XPS is a surface sensitive measurement technique due to the low inelastic mean free path of electrons in solids.

When X-rays interact with matter, an electron from the core or valence states is excited into the vacuum and ejected as a free electron. According to Koopmans’ theorem, it is assumed that the excitation of one electron does not change the energies of the remaining electrons. The kinetic energy of these ejected electrons can be measured using an electron analyzer and the binding energy can be written as,

$$E_{kin} = h\nu + E_{bind} - \Phi \quad (2.16)$$

where E_{kin} is the kinetic energy, $h\nu$ is the energy of the incident photons, E_{bind} is the binding energy of the electron and Φ is the work function.

The quantum mechanical description of the photoemission process is analogous to X-ray absorption process. Hence, the transition probability per unit time $W_{i \rightarrow f}$, from a state $|i\rangle$ to a state $|f\rangle$ is described by Fermi's Golden rule:

$$W_{i \rightarrow f} = \frac{2\pi}{\hbar} |\langle f | T_{i \rightarrow f} | i \rangle|^2 \rho(E_f) \quad (2.17)$$

where $T_{i \rightarrow f}$ denotes the interaction operator. In the first order the interaction operator $T_{i \rightarrow f}$ is equal to the interaction Hamiltonian \mathcal{H}_{int} .

By neglecting the two-photon process and also by assuming the radiation wavelength to be far higher than the atomic distances, the interaction Hamiltonian \mathcal{H}_{int} takes a simpler form given by,

$$\mathcal{H}_{int} = \frac{e}{m_e c} \mathbf{p} \cdot \mathbf{A} \quad (2.18)$$

A schematic of XPS process is shown in Fig. 2.2. X-rays with an energy $E = h\nu$ excite an electron from the core levels to the vacuum as a free electron as depicted in Fig. 2.2. The core hole state is the same as that described for X-ray absorption and hence the relaxation process of the core hole is also the same as that described in section 2.1.

Resonant photoemission In resonant photoemission, photons with an energy near the absorption threshold of a core level are used. The direct photoemission of valence band electrons then interfere with the Auger core-valence-valence (CVV) electrons that are emitted resulting in an intensity enhancement in the valence levels.

3 Experimental

The experiments described in this thesis were performed in an ultra high vacuum (UHV) chamber situated at MPI, Halle. In this chapter, brief descriptions of the different experimental techniques are given in section 3.1 followed by the details of materials used and their methods of preparation in section 3.2.

3.1 Experimental apparatus and techniques

UHV chamber The UHV apparatus is made of stainless steel and is maintained at MPI Halle. It provides a vacuum of the order of 2×10^{-10} mbar. A schematic side view of the apparatus is given in Fig. 3.1. It consists of basic vacuum components such as pressure gauges, turbo molecular pumps, ion pumps and titanium sublimation pumps. As shown in Fig. 3.1, the UHV apparatus comprises of two sets of chambers, an upper chamber for preparation and characterization of investigated materials and a lower chamber for magnetic measurements.

A manipulator is attached above the upper chamber which can be moved in all three directions X, Y and Z as well as rotated about polar and azimuthal angles for transfer, preparation and measurements of samples. The samples to be investigated are mounted onto tantalum sample holders using tantalum strips. The sample holder is placed in the manipulator which is provided with liquid N₂ and He cooling.

The upper chamber is equipped with a 4-fold metal e-beam evaporator for the epitaxial growth of thin films and a quartz crystal monitor for thickness calibration. It also has Auger electron spectroscopy, low-energy electron diffraction (LEED) and magneto-optic Kerr effect (MOKE) setups for the characterization of samples and preliminary magnetic measurements. The lower chamber is arranged in such a way that it can be attached to a synchrotron beamline in order to conduct X-ray absorption measurements. It is equipped with two magnetic coils which operate using current pulses for magnetic field generation in the horizontal as well as vertical directions, which enables magnetization parallel or perpendicular to the surface of the sample. A maximum field of 50 mT can be generated using these coils. The chamber is provided with a load-lock set-up to enable the vacuum transfer of sample to the preparation chamber. Samples prepared in other chambers can also be vacuum transferred to this chamber with the help of the load-lock system. Additional free ports allow for mounting pressurized oxygen and other gases in the chamber. The samples studied in this thesis were all prepared in this chamber unless otherwise indicated.

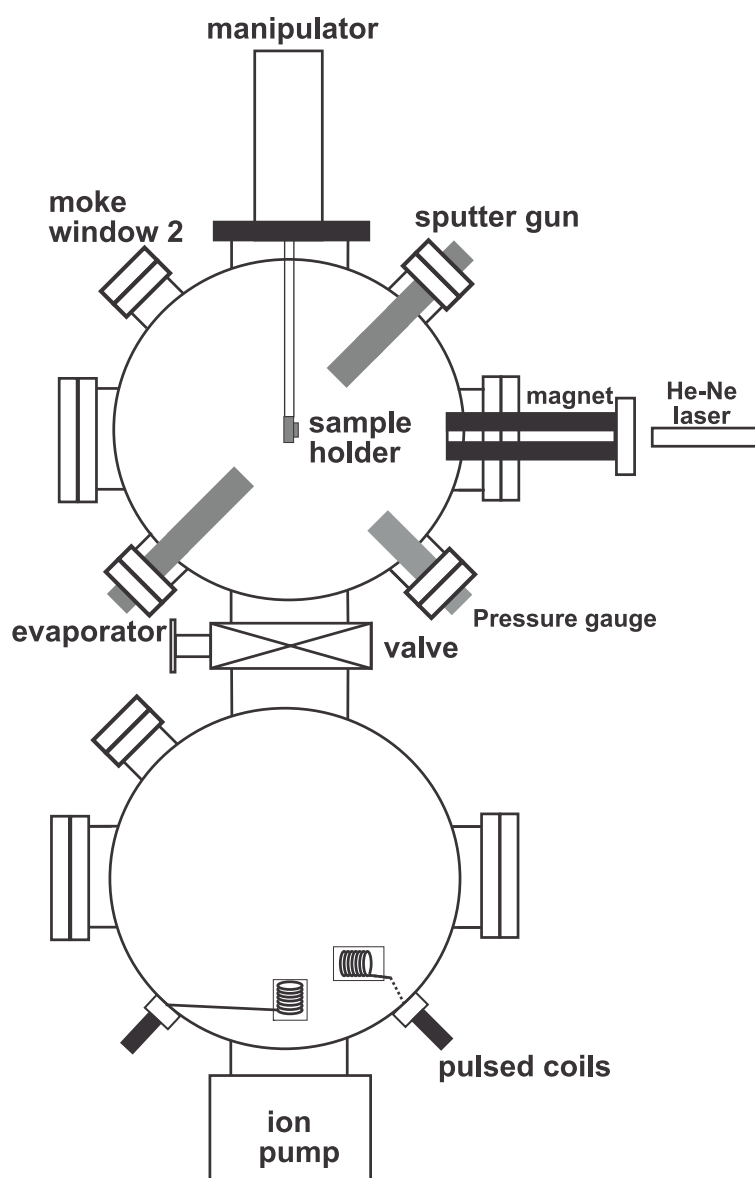


Figure 3.1: Schematic side view representation of the UHV chamber used to conduct the experiments mentioned in this thesis.

The different experimental techniques employed for sample preparation and measurements are sputtering, annealing, evaporation, Auger electron spectroscopy (AES), low-energy electron diffraction (LEED), magneto-optic Kerr effect (MOKE), X-ray photoelectron spectroscopy (XPS), scanning electron microscopy (SEM), energy dispersive X-ray (EDX) spectroscopy and X-ray absorption spectroscopy (XAS) which are described below.

Sputtering The chamber is equipped with a Physical Electronics sputter ion gun to clean the sample surfaces. Sputtering is the process of physical evaporation of atoms from a surface through the momentum transfer by bombarding energetic ions (for example, argon ions) accelerated in an electric field. The pressurized argon gas required

for sputtering was mounted to a flange at the sputter ion gun.

Annealing A filament is placed just below the sample holder in the manipulator and samples can be annealed to temperatures above 1100 K, with or without O₂ atmosphere through electron bombardment heating by increasing the filament current. The annealing temperature can be controlled by an N-type thermocouple attached to the sample holder.

Evaporation The thin films mentioned in this thesis have been prepared through metal e-beam evaporation. In this technique the atomic or molecular beams produced from Knudsen cells are used to prepare atomic thick films on suitable substrates. The rate of evaporation was determined using a quartz crystal monitor and stable growth rates were acquired by the control of the electron beam current and the outgoing ionized particle flux of the evaporator.

Auger electron spectroscopy (AES) The creation of Auger electron is already discussed in the previous chapter. AES is based on the principle of release of Auger electrons. In brief, when an atom gets bombarded with an electron beam, the core level of the atom gets ionized and a subsequent rearrangement occurs in order to reach a lower energy state which leaves the atom in a doubly ionized state and the energy difference between these two states is compensated by the ejection of an Auger electron [15].

Auger electron spectroscopy was employed to study the cleanliness of substrates as well as the chemical composition of substrates and thin films. The AES setup consists of an electron gun which generates a focussed electron beam. This electron beam hits the sample and ionizes it. In the present setup, the electron gun from Varian was usually operated at 3 keV. The emitted Auger electrons from the sample are deflected back to a cylindrical mirror analyzer and are detected. The electron multiplier multiplies the electrons and these electrons are analyzed using data processing electronics. These Auger electrons can then be plotted as a function of energy to generate an AES spectrum. Typically, Auger electron spectra are measured in the derivative mode by modulating a small AC voltage at the sweep supply. Measuring in the derivative mode helps to understand the usually low intensity Auger peaks better.

Low-energy electron diffraction (LEED) Being one of the versatile experimental techniques used for surface structure determination, LEED was employed in order to check the long range order of surfaces and thin films. In LEED, electrons possessing well defined kinetic energies (typically 10-1000 eV) incident normal to a sample surface. These electrons get backscattered and generate an electron diffraction pattern at a screen. Upon interaction with the sample surface, the electrons loose kinetic energies mainly through the inelastic scattering processes such as plasmon- and phonon excitations as well as electron-electron interactions. LEED image thus formed at the

screen can be qualitatively understood by considering the scattering of electrons by the atoms of a sample surface and hence provides information regarding the periodicity and structure of surfaces [20].

The chamber is equipped with an Omicron LEED system mounted on the top chamber. The LEED optics consists of an electron gun, a detector, electrostatic grids and a screen. The electron gun generates a monochromatic beam of electrons (typically 10-1000 eV) which gets incident normal on a sample surface and gets backscattered. The grids are used to remove inelastically scattered electrons. The present optics operates with a 4-grid system. The elastically scattered electrons are accelerated towards a phosphorescent screen and they appear on the screen as bright white spots. This LEED pattern corresponds to the image of the reciprocal space and the LEED spot intensity is proportional to the number of electrons in the corresponding beams.

Magneto-optic Kerr effect (MOKE) The MOKE setup in this chamber helps to measure hysteresis loops in both polar and longitudinal modes. The setup consists of a He-Ne laser which delivers a laser beam into the chamber. The laser beam passes through a polarizer filter and a photo-elastic modulator which provides a periodic modulation at 50 kHz of the light polarization. Then, it passes through the bore of a magnet (labelled as MOKE magnet in Fig. 3.1), the magnetic coil can be driven by a power supply and provides a maximum magnetic field of 60 mT. The laser beam then hits the sample. Measurements in the polar and longitudinal modes are taken by rotating the sample to different geometries. The laser beam gets reflected from the sample and exit through two different MOKE windows (each for the polar and longitudinal modes) which have detection system. The detection system consists of a polarizer filter and a photodiode to record the reflected light. A signal amplifier combined with a lock-in system is used to measure the detected Kerr signal. The Kerr ellipticity which is thus directly measured is proportional to the magnetization of the sample.

X-ray photoelectron spectroscopy (XPS) The XPS measurements were performed in the VSW XPS analyzer at the BACH beamline, Elettra. Typically, the XPS setup comprises of an X-ray source (in this case it is the synchrotron radiation) and an electron energy analyser, combined with a detection system (in this case, it is the hemispherical sector analyser (HSA)). A lens system in the HSA focus the photoelectrons leaving the sample surface to the focal point of the analyser. The HSA contains two plates or hemispheres carrying a constant voltage. The electrons on entering the analyser experience an electric field and consequently travel through a trajectory and get focussed at the exit slit. Only those electrons matching the pass energy (user defined analyser energy) will enter the hemispherical analyzer, focus at the exit slit and get detected by a channeltron electron multiplier detector. By ramping up the retarding field potential, detected photoelectrons are counted as a function of energy.

Scanning electron microscopy (SEM) and energy dispersive X-ray (EDX) spectroscopy The scanning electron microscopy (SEM) images of samples have been recorded ex-citu after removing from the UHV chamber. The SIGMA series scanning electron microscope from Zeiss, is situated at MPI, Halle. SEM uses a focused beam of electrons to produce an image of the sample. The main components of SEM include an electron gun which produces a collimated electron beam, electron lenses which focus the electron beam, deflection plates to deflect the electron beam in the x and y axes so that it scans in a raster fashion over the sample and electron detectors to detect the signal. Due to the interaction of the high energy electron beam with the sample surface, secondary electrons and backscattered electrons are created which contribute in the imaging of the morphology, topography and contrast of samples.

The X-ray radiation emitted from the sample due to the interaction with the high energy electron beam can be analysed with a detector to generate a spectrum. This method is known as energy dispersive X-ray spectroscopy (EDX). Since the emission of X-rays is specific to elements, the spectrum generated is highly element specific. Hence, this technique is employed for the detection of constituents of samples analysed in SEM. The EDX system at MPI, Halle uses the Quantax 400 (XFlash 5030) detector from Bruker.

X-ray absorption spectroscopy (XAS) Spectroscopic investigations such as XAS, XMCD and XMLD require synchrotron radiation sources owing to the high collimation, high intensity, high photon flux and energy tunability. Synchrotron radiation is the electromagnetic radiation produced by accelerated charged particles (electrons or positrons) when they hit the curved parts of a storage ring. Synchrotron radiation is emitted tangential to the curved portions of the storage ring.

By installing Insertion devices (ID), such as undulators in the storage ring, variable polarization of light can be obtained. Undulators are periodic structures composed of dipole magnets [21]. They produce electromagnetic radiation from the electron beam since electrons radiate energy while traversing through a magnetic field. By changing the gap distance between upper and lower magnetic arrays, the magnetic field strength of the undulator is changed which results in a change in photon energy. By moving the relative position between the two magnetic arrays (phase shift), the polarization of light can be varied to circular, elliptical and linear.

The soft X-ray synchrotron measurements described in this thesis have been performed at UE56/2-PGM beamlines (BESSY II, Helmholtz Zentrum, Berlin), BACH beamline (Elettra, Trieste) and I1011 (MAXlab, Lund). The measurements presented in chapter 5 have been done at Elettra, the magnetization loops in chapter 4 have been recorded at MAXlab and all other measurements have been from UE56/2-PGM beamlines. The absorption spectra measured from BESSY II have also been compared to the measurements from MAXlab and Trieste.

BESSY II has three beamlines of the UE56/2 PGM type. The first one is UE56/1-

PGM which is maintained by HZB staff and the other two beamlines of this type are UE56/2-PGM1 and UE56/2-PGM2 which are maintained by the Max-Planck-society. The investigations in this thesis were performed on UE56/2-PGM1 and UE56/2-PGM2 beamlines which are highly equivalent.

The UE56/2 PGM is an elliptical undulator beamline which provides soft X-rays in the energy range 50-1300 eV [21] with polarisation tunable to linear or circular which is appropriate for the XAS and XMCD examination of our samples (Fe $L_{2,3}$, Ti $L_{2,3}$, O K edge and Ba $M_{4,5}$). The beamline uses a Sasaki type elliptical undulator as insertion device. The beamline employs a collimated plane grating monochromator (PGM) and refocusing mirrors. A high degree of circular polarization ($P > 0.8$) is achieved for most of the energy range [21]. The radiation passes through a gold mesh in the last refocussing mirror in the beamline before falling onto the sample. This results in the emission of photoelectrons giving rise to a current. This current is proportional to the incident radiation and thus serves to normalize the measured absorption intensity to the number of incoming photons. The beam size at the sample is in the range of $1 \times 1 \text{ mm}^2$. High fluxes of the order of $4 \times 10^{15} \text{ photons/s}$ were obtained typically.

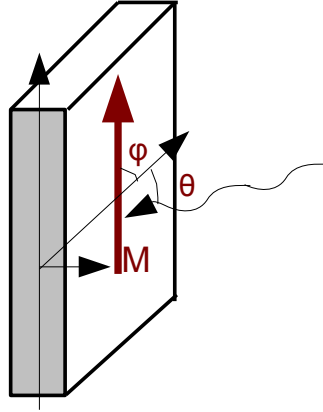


Figure 3.2: Experimental geometry of XMCD measurements

The absorption measurements have been conducted in the total electron yield (TEY) mode by measuring the drain current with a picoammeter. The measured spectra were normalized to the incoming photon flux by dividing the measured sample current with the photocurrent of the last refocussing mirror in the beamline. A linear background intensity at the pre-edge region is subtracted from these absorption spectra.

The measurement geometry for the XMCD measurements is specified in the schematic given in Fig. 3.2. The consistency of XMCD signal was checked by keeping the magnetization of the sample (labelled M) constant and by changing the light polarization and vice versa. Results obtained from both type of measurements have been found to be similar.

3.2 Materials and methods of preparation

The relevant materials investigated in this thesis are introduced in this section. The focus of this section is on the description of general properties as well as preparation methods.

3.2.1 BaTiO₃(001)

BaTiO₃ is a ferroelectric material which is widely used in the manufacture of electronic components and electro-optic devices due to its high dielectric constant. It has a perovskite-like structure which can be represented by the formula ABO₃ where the cations A and B have different sizes. The BaTiO₃ structure is formed by the oxygen octahedra with the octahedral hole occupancy of smaller cations and the dodecahedral hole occupancy of larger cations. The structure of a unit cell of BaTiO₃ is depicted in Fig. 3.3.

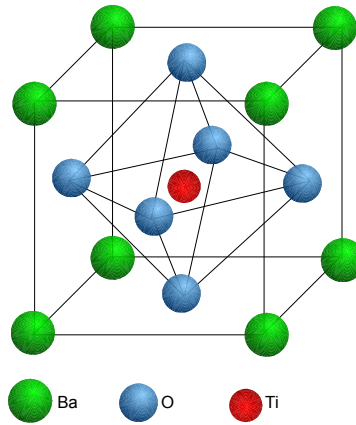


Figure 3.3: Structure model of BaTiO₃

BaTiO₃ was the first developed piezoelectric ceramic. At room temperature, the single crystalline BaTiO₃ has a band gap of 3.2 eV. The BaTiO₃ lattice changes its crystallographic dimensions upon changing the temperature due to the distortion of the TiO₆ octahedra. Between 278 and 393 K, BaTiO₃ has tetragonal crystalline structure. Above 393 K, BaTiO₃ exhibits cubic geometry. Below 278 K, BaTiO₃ changes to orthorhombic and another phase transition occurs at 183 K below which BaTiO₃ is rhombohedral [9].

Preparation of BaTiO₃(001) single crystals Commercially available (001) surfaces of single crystal substrates of BaTiO₃ (supplied by MaTeck: dimensions 5 mm×5 mm×1 mm) of good crystalline quality have been used for the measurements. The BaTiO₃ substrate used for measurements was prepared by Ar⁺ ion bombardment for 10-15 minutes at room temperature. The hot filament emission current was of the order of 30 mA and kinetic energies in the range 500 eV-1 keV have been used which resulted in sample currents typically in the range of 1 to 5 μA. After argon (Ar⁺) ion

sputtering, the crystal was subsequently annealed in an oxygen atmosphere ($p_{O_2} = 1 \times 10^{-6}$ mbar) at 1075 K for 10 minutes to remove carbon impurities and to restore surface order. With the high temperature annealing, carbon left over at the sample surface after annealing will be converted to CO_2 and pumped away.

The surface preparation plays an important role for $BaTiO_3$ since visibly the crystal turned bluish black from transparent upon annealing. Annealing creates oxygen vacancies which are necessary to make the $BaTiO_3$ electrically conducting to enable different surface sensitive measurements such as LEED, XPS and XAS. The cleanliness of the substrate has been examined by AES and XPS. Auger electron spectra showed no C lines indicating the cleanliness of the surface. The structural ordering has been studied through LEED. The long range order in the substrate is confirmed by the presence of sharp spots. (2×2) spots were also obtained at some energies probably as a result of oxygen vacancies. It is already reported for $SrTiO_3(100)$ surfaces that annealing in UHV creates oxygen vacancies and gives rise to a (2×2) superstructure [22, 23]. Details of $BaTiO_3$ characterisations will be discussed in the next chapter.

$BaTiO_3(001)$ layer samples $BaTiO_3(100)$ layer samples prepared by two different deposition techniques - pulsed laser deposition (PLD) and magnetron sputtering have been employed for the XAS measurements. The $BaTiO_3(001)$ layers were grown on $SrTiO_3(100)$ by PLD. The $BaTiO_3(001)$ layers were grown on $Pt(100)$ by magnetron sputtering. Fe films were later evaporated onto $BaTiO_3(001)/Pt(100)$. Details regarding the growth and characterizations of the $BaTiO_3(001)/Pt(100)$ can be found in [24].

3.2.2 Fe

One of the strongest and earliest known ferromagnetic material, Fe has a Curie temperature of 1043 K and a high room temperature saturation magnetization of 1714 emu/cm^3 . At room temperature, Fe has a body-centered cubic structure with a lattice parameter of 2.866 \AA . The magnetic easy axis is found to be along the $[100]$ direction for bcc Fe [25]. The magnetic moment in Fe originates from the difference in the number of occupied states between the majority and minority bands of valence band. Valence band splitting occurs due to the positive exchange interaction [26]. For thin films and surfaces, the d band and surface resonance states are narrowed due to the reduced coordination and broken symmetry, thereby resulting in changes in the magnetic properties [26].

Epitaxial growth of Fe thin films Ultrathin layers of Fe have been deposited on $BaTiO_3(001)$ by e-beam evaporation from a metal e-beam evaporator at a pressure 2×10^{-9} mbar at room temperature from Fe rods of high purity (99.9%) which were also thoroughly outgassed. Film thickness has been calibrated using a quartz crystal monitor. The evaporation rate for Fe was 0.7 MLE/min . Monolayer equivalent (MLE)

is referred to the amount of Fe in a homogeneous film having bulk structure and a thickness of 1.4 Å.

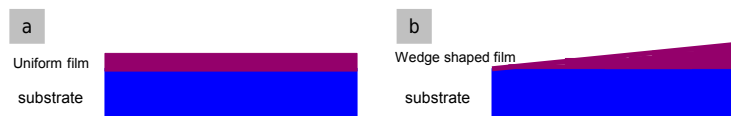


Figure 3.4: Schematic of the two types of samples investigated in this thesis (a) uniform thin film (b) wedge shaped film.

Uniform Fe film samples were prepared along with wedge shaped film samples. The two types of samples are schematically illustrated in Fig. 3.4, where (a) shows a uniform thin film on the substrate and (b) shows a wedge shaped film. For the evaporation of a wedge shaped Fe film, the sample was slowly moved down with manipulator. A shutter was used to cover the sample. By moving the sample down, the substrate got deposited with Fe from the evaporator as the sample slowly came out of the shutter cover. The motor program of the manipulator allows for a controlled motion of manipulator which can be set according to the desired sample thickness. Thus the longest evaporation time leads to the highest thickness of Fe film.

The as prepared films were later annealed to 373 K to release strains and to provide a better ordering. The films have been characterised by means of AES which recorded Fe peaks. The long range order in films has been investigated using LEED. The growth and electronic structure of the layers have been studied by XPS and XAS.

3.2.3 Fe₃O₄

Fe₃O₄ (magnetite) is a mixed valence oxide consisting of Fe ions in two ionic states Fe²⁺ and Fe³⁺ which crystallizes in the cubic inverse spinel structure. It is formed by the cubic close packed oxide (O²⁻) ions and the Fe ions occupy octahedral and tetrahedral sites. The Fe³⁺ ions occupy a quarter of the tetrahedral sites. Fe³⁺ and Fe²⁺ ions occupy half of the octahedral sites. Hence, the Fe ion in a tetrahedral site is surrounded by four O²⁻ ions and the Fe ions in octahedral sites are surrounded by six O²⁻ ions [14]. The Fe₃O₄ unit cell has dimensions $a=8.39\text{\AA}$.

The arrangement of Fe ions in these two sites result in complex exchange interactions between and within these sites. And, Fe₃O₄ is ferrimagnetic with a Curie temperature of 858 K. Interestingly, Fe₃O₄ undergoes a phase transition at 120 K, known as Verwey transition whereby the conductivity of Fe₃O₄ drops by two orders of magnitude in the low temperature phase [27]. This transition is accompanied by a change in the structure and magnetic properties with the structure changing from cubic phase above the transition to monoclinic phase below 120 K [28]. However, contradicting reports regarding a fluctuating mixed valence state question the validity of the charge ordering as Fe²⁺ and Fe³⁺ [29, 30]. This suggests that the assignment of integer ²⁺ and ³⁺ charges to the Fe ions might not be appropriate.

In the [100] direction of $\text{Fe}_3\text{O}_4(001)$, two types of surface terminations are possible, one with oxygen and octahedral iron (B layer) and the other with tetrahedral iron (A layer) [31, 32]. These two layers alternate in the [100] direction.

Epitaxial growth of Fe_3O_4 thin films Fe_3O_4 films investigated in this thesis have been prepared by reactive evaporation of Fe in an O_2 atmosphere. During evaporation, the substrate has been maintained at 573 K and the O_2 pressure in the chamber was kept at 2×10^{-6} mbar. The thickness of these Fe_3O_4 films has been calibrated by a quartz crystal monitor and by using X-ray absorption spectroscopy. The evaporation rate was $2 \text{ \AA}/\text{min}$. Similar to Fe, thin uniform film as well as wedge shaped film samples of Fe_3O_4 have been evaporated.

The as prepared films have been then post annealed to higher temperatures (673 K and 873 K). The stoichiometry of the films has been checked with XAS and XMCD measurements, details of which are presented in chapter 7.

4 Growth and magnetism of Fe films on BaTiO₃(001)

Thin films of magnetic materials display improved properties compared to bulk owing to the reduction in size and consequent dimensionality effects. Especially interesting are the changes in magnetic properties in thin film magnetic materials due to the interaction with a ferroelectric substrate which offer possibilities of future applications. In this chapter, the characterisation of ferroelectric BaTiO₃(001) substrates as well as the growth and the magnetic properties of ferromagnetic epitaxial Fe thin films deposited on clean BaTiO₃(001) are discussed.

A brief introduction to the state of the art research is presented in section 4.1 followed by a detailed description of the characterization of clean BaTiO₃(001) substrates with LEED, XAS and RPES in section 4.2. The growth of Fe ultrathin films on clean BaTiO₃(001) and the interface effects are investigated in section 4.3. The magnetic properties of the as prepared Fe films are discussed in section 4.4. The main conclusions drawn from this chapter are summarized in section 4.5.

4.1 Introduction

Materials possessing two or more ferroic properties in the same phase are known as multiferroics, a term coined by Hans Schmid [33]. The ferroic properties include ferromagnetism, ferroelectricity and ferroelasticity. The coexistence of two or more ferroic properties leads to multiferroic coupling which allows the control of ferromagnetism with the application of an electric field and vice versa [34]. On the other hand, magnetoelectric materials are those in which the magnetoelectric coupling exist which results from the interaction of any magnetic or electric order parameters, for example, paramagnetic ferroelectrics [35, 36]. Hence, some overlap with the multiferroicity is expected. The term magnetoelectric was coined by Debye [37] but it was as early as in 1894 that Curie suggested the possibility of a magnetoelectric behavior [38].

In conventional single phase multiferroic materials, the coupling is small. The fascinating arena of applications and technological relevance due to the coupling between different ferroic orders initiated the need for materials which combine magnetic as well as electric components. This made the fabrication and study of novel artificial dual phase systems extremely popular whereby the materials with desired functionalities can be combined to give rise to larger coupling across the interface. A prototype

of such a multiferroic interface is epitaxial Fe films on BaTiO₃ which offers a coupling of ferromagnetism and ferroelectricity.

Fe/BaTiO₃ interface has gained considerable attention as a potential candidate for multiferroic applications such as in data storage and spintronics. A magnetoelectric effect has been predicted for the Fe/BaTiO₃ interface and ferroelectric control of magnetism has been demonstrated later [8, 9]. Recently, it has been shown that magnetic domain patterns with alternating uniaxial and biaxial anisotropy can be imprinted on Fe films grown on BaTiO₃ consisting of a and c domains [39] which can be utilized for potential applications. These results have generated particular research interest and attention on this two phase multiferroic system.

First principles calculations predict a change in magnetic order for Fe films on TiO₂ terminated BaTiO₃ or PbTiO₃ surfaces from ferro- to ferrimagnetic and again to ferromagnetic as the thickness of the Fe monolayers increases [10]. First principles calculations on Fe/BaTiO₃ also show the presence of XMCD and magnetism of the first layers of Fe on BaTiO₃ [11]. The experimental realization of these predicted results would be interesting.

It is well known that the growth of thin films have a profound impact on the magnetic properties. Hence, the growth and the characterization of Fe thin films on different substrates have been of particular interest. The growth and the morphology of Fe thin films on SrTiO₃ have been investigated in detail [40, 41], where it has been found that Fe prefers a growth with the formation of islands. However, the morphology and the growth of Fe ultrathin films on BaTiO₃(001) single crystal substrates have not been investigated in detail so far.

Stability of the interface also plays a crucial role in the magnetic properties of thin films. Single crystal Fe thin films have been grown on a number of insulator substrates (such as MgO) and semiconductors (such as GaAs, InAs and Si) [42, 43, 44, 45]. A considerable intermixing between Fe and GaAs was found whereas the extent of intermixing was found to be comparatively low in the case of Fe on InAs [44]. The interface between Fe and oxidic substrates has been studied extensively. For example, for Fe on NiO, the presence of an oxidic layer upto 2 MLE has been found [46]. A weak chemical interaction at the interface has also been observed for Fe on MgO [42]. However, Fe was found to form an Fe²⁺ state in substrates such as Al₂O₃ [47]. The interface electronic structures of core-shell nanostructures of Fe, Fe₂O₃, α -Fe₂O₃ and Fe₃O₄ on BaTiO₃ have been investigated and it was found that the valence levels of Ti were essentially the same as that of BaTiO₃ [48]. Brivio and co-workers observed through XPS that the Fe at the interface is oxidized with a thickness of around 2 nm for Fe films grown on BaTiO₃ [49]. But, hard X-ray photoemission spectroscopy (HAXPES) studies by Zenkevich and co-workers on Fe/BaTiO₃ proved the absence of oxidation [50]. In this regard, further studies are required to resolve the origin of these controversial findings.

The magnetism of Fe films has been widely investigated. The magnetic properties

and the domain structures of Fe have been elucidated on substrates such as GaAs(001) and MgO(001) [42, 51]. In the study of magnetic thin films, one important topic is the magnetic anisotropy which determines the direction of magnetization. The interface and surface effects as well as strain play a major role in anisotropy. Shirahata and co-workers investigated the anisotropy of a 30 nm thick Fe film on BaTiO₃ and found a symmetry switching of the magnetic anisotropy associated with the interface lattice distortion occurring at the structural phase transition of BaTiO₃ [52]. This magnetic symmetry change was attributed to a change in magnetoelastic coupling at the interface [52]. FMR measurements on 30 nm Fe films on BaTiO₃/SrTiO₃(001) revealed dual resonance modes which was ascribed to the relaxed Fe in the film interior and the strained Fe at the interface [53]. However, the magnetic properties of the ultrathin films of Fe on BaTiO₃ remain to be explored in detail.

This chapter focuses on the growth of Fe ultrathin films on BaTiO₃(001) and the investigations of the interface stability and the magnetic properties.

4.2 Characterisation of BaTiO₃(001)

As described in chapter 3, BaTiO₃(001) is a widely used ferroelectric material with a variety of technological and industrial applications. The surface preparation of BaTiO₃(001) is also discussed in chapter 3. The surface treatment gives rise to a well ordered BaTiO₃ surface which has been noted from LEED investigations and the stoichiometry has been confirmed with XPS. Resonant photoemission studies have also been performed to characterize the surface.

4.2.1 Low-energy electron diffraction investigations

After the surface preparation, the long range order of the BaTiO₃(001) single crystal was checked with LEED. The results of the LEED investigations are shown in Fig. 4.1.

Figure 4.1 (a) shows a model for the structure of BaTiO₃(001) in top view along with the inverted gray scale LEED images at 90 eV and 70 eV kinetic electron energies in (b) and (c). The LEED images have been recorded from a clean BaTiO₃ prepared as mentioned in chapter 3. The alternating layers of BaO and TiO₂ of a BaTiO₃ crystal are represented in the structure model. The structure model in Fig. 4.1 (a) assumes a perfect TiO₂ termination without oxygen vacancies or reconstructions, because it is reported to be energetically more favorable [10]. The unit cell of BaTiO₃ is represented by the black square in the figure. As shown in Fig. 4.1, the surface treatment results in a LEED pattern with sharp spots indicating a long range order. In addition to the bright (1 0) and (1 1) spots, weak half order spots ($\frac{1}{2} \frac{1}{2}$) are obtained at some kinetic electron energies indicating a weak c(2×2) reconstruction. The integer order spots of BaTiO₃ are found to be sharp and the sharpness of the LEED spots point to good crystallinity of the substrate surface.

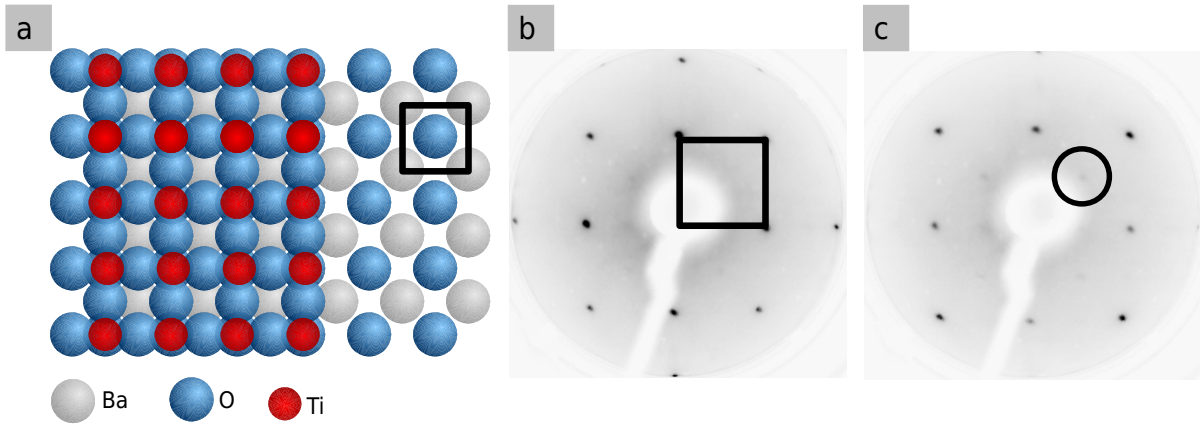


Figure 4.1: Structure model and LEED images of a clean BaTiO₃(001) single crystal surface prepared by annealing at 1075 K. (a) Top view of the structure model of a BaTiO₃(001) surface with alternating BaO and TiO₂ layers, (b) and (c) LEED images from a clean BaTiO₃ substrate at kinetic electron energies 90 eV and 70 eV respectively. The gray scale is inverted in the LEED images, i.e. black represents high electron density. The black square represents the unit cell. The position of the half order spot is indicated by the black circle.

The surface reconstruction indicates either relaxation, rearrangement or absence of oxygen atoms from the top layers. It might occur as a result of the surface preparation whereby the high temperature annealing in UHV produces oxygen vacancies, thus leaving the surface reduced, although some of them are compensated by annealing in an oxygen atmosphere. The $c(2 \times 2)$ reconstruction, hence points to a large number of oxygen vacancies. At the same time, the presence of the reconstruction at certain kinetic energies and the absence of it at some parts of the surface, imply the presence of reconstructed area as small patches on the surface. Hence, it can be assumed that some oxygen vacancies are present, at the same time, the absence of a large number of oxygen atoms from the surface can be ruled out.

After annealing, the colour of the crystal changes from transparent to bluish black indicating the reduction of the crystal by the creation of oxygen vacancies. Since oxygen is a weak scatterer, the $c(2 \times 2)$ reconstruction spots appear as faint. With the absence of oxygen atoms, the Ti atoms at the surface may also get relaxed at the surface. When an oxygen vacancy occurs, there must be charge compensation on Ba and Ti than their original 2+ and 4+ states. Ti will change to 3+ states to compensate for the loss of oxygen.

The reconstruction can also have a very limited influence on the positions of atoms to be deposited on top. Theoretical studies have assumed that with the evaporation of Fe atoms on BaTiO₃(001), the Fe atoms occupy the on-top positions on oxygen atoms [8, 10]. With the missing oxygen lattice points, the first layer of Fe might form voids at those positions which might get compensated with subsequent layers of Fe atoms.

BaTiO₃(001) surface preparations give rise to a number of different surface reconstructions as reported [54, 55, 56, 57]. Although a number of surface reconstructions are observed for BaTiO₃ like (1×1) , (2×1) , (2×2) , $c(2 \times 2)$, $(\sqrt{5} \times \sqrt{5})$, (3×1) , (3×2) ,

(6×1) [55, 57, 58, 59, 60] through various surface sensitive techniques, not many structures have been solved. First principles calculations predict more stability for the TiO-terminated interfaces of BaTiO₃(001) surfaces [61]. Out of the many surface reconstructions, a structure for the (2×1) reconstruction has been proposed for BaTiO₃(001) [56] with a TiO₂ terminated surface. But, at the same time, a similar perovskite SrTiO₃(001) has been widely investigated for the recurring surface reconstructions and various structures have been quantitatively resolved. It is reported that the annealing in oxygen rich vacuum produces a (2×2) reconstruction at the SrTiO₃ surface [62]. Most of the works proposed a TiO₂ rich overlayer for the surface. A combined STM and DFT study has proposed a double layer TiO₂ terminated structure for the (2×2) reconstruction for SrTiO₃ [63]. Quite remarkably, they propose that the structure is not oxygen reduced. Since BaTiO₃ is similar to SrTiO₃ in many structural aspects, similar arguments hold in the case of BaTiO₃ also. With reference to the reported structures solved for BaTiO₃ [55, 56], the $c(2\times 2)$ surface reconstruction can possibly be due to a TiO₂ termination.

Thus, from the LEED investigations, we can arrive at the conclusion that the surface preparations give rise to a well ordered and slightly reduced BaTiO₃ surface.

4.2.2 X-ray absorption spectroscopy studies

Electronic structure of the as prepared BaTiO₃ single crystal surface has been determined using XAS measurements combined with first principles calculations [64]. High resolution XAS measurements have been performed on a clean BaTiO₃(001) surface and the spectra were measured at Ti 2*p* (*L*_{2,3} edges), Ba 3*d* (*M*_{4,5} edges) and O 1*s* (*K* edge) in the TEY mode using linear polarized X-rays at room temperature in different directions by changing the polar as well as azimuthal angles. For comparison, all spectra are normalized to an edge jump from 0 to 1.

Figure 4.2 presents the XA spectra at Ti *L*_{2,3}, Ba *M*_{4,5} and O *K* edges measured in grazing incidence along two in-plane orientations - [100] and [110] directions of BaTiO₃. The spectra shown in Fig. 4.2 match well with the reported experimental and calculated XA spectra at the Ti *L*_{2,3}, Ba *M*_{4,5} and O *K* edges and hence the features in the spectra can be assigned according to the available literature [65, 66, 67, 68, 64, 69].

Figure 4.2(a) shows the Ti *L*_{2,3} edges absorption spectra. The Ti *L*_{2,3} edges spectrum originates from the Ti 2*p* (core level) to 3*d* (unoccupied state) electronic transitions. At the Ti *L* edge, the absorption spectrum consists of two small pre-edge features observed at photon energies 455.8 and 456.4 eV respectively. The *L* edge is split into *L*₂ and *L*₃ due to spin-orbit interaction and peaks are observed at the *L*₂ and *L*₃ edges at energies 457.25, 459.3, 462.7 and 464.6 eV. Treating BaTiO₃ as a cluster made of Ti and six oxygen atoms, the 3*d* states of Ti are assumed to be split into two states assigned as *t*_{2*g*} and *e*_g. The energy separation between the two subbands in Fig. 4.2 is found to be approximately 2 eV which matches with the splitting between the two states [64, 70].

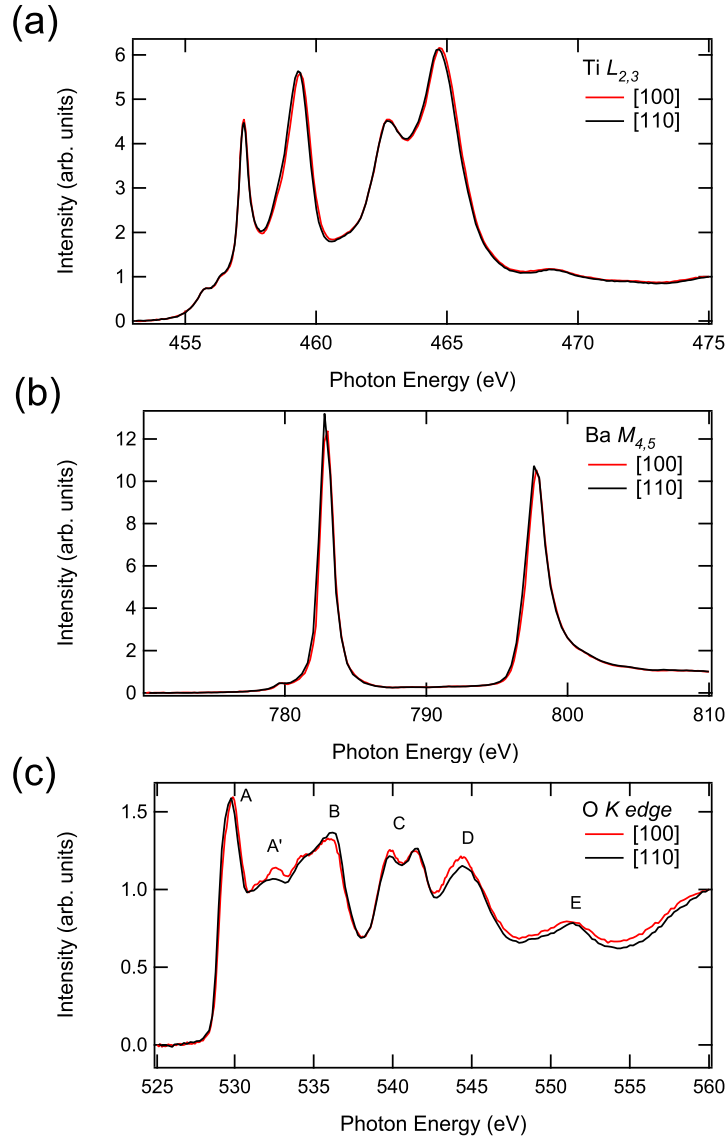


Figure 4.2: High resolution X-ray absorption spectra at (a) Ti $L_{2,3}$, (b) Ba $M_{4,5}$ and (c) O K edges from a BaTiO₃(001) single crystal surface. The spectra have been measured using the linear polarization of light in the TEY mode in grazing incidence with the sample at room temperature. The measurements were performed along the directions as indicated in the figure legend. The spectra are normalized to an edge jump of unity.

The Ba $M_{4,5}$ edges absorption spectrum is presented in Fig. 4.2(b). The spectrum comprises of a pre-edge feature at 779.2 eV and peaks at 782.8 and 797.6 eV respectively. According to theory, the spectral features correspond to the dipole-allowed Ba $3d^{10}4f^0 \rightarrow 3d^94f^1$ transitions [64]. The M_5 and M_4 features are attributed to the $3d_{5/2}$ (at 782.8 eV) and $3d_{3/2}$ (at 797.6 eV) core hole states.

The O K edge spectrum is the result of the transitions from O $1s \rightarrow p$ which is shown in Fig. 4.2(c). The features at the O K edge in Fig. 4.2 are labelled as reported in [64] to help an easy comparison. The associated energies of features labelled A, A', B, C, D and E are 529.9, 532.6, 535.9, 539.8 and 541.6, 544.4 and 551.4 eV respectively. The features A and A' arise as a result of transitions from O $1s$ core level to final states with

O $2p$ levels hybridized with Ti $3d$ levels. The energy separation between A and A' is found to be 2.1 eV which corresponds to the crystal field splitting at the Ti $L_{2,3}$ edges. The feature B results from transitions to O $2p$ -Ba $5d$ hybridized states. The features B and C are separated by a minimum. The features after the minimum result from the transitions to final states consisting of O $2p$, Ti $4s$ and $4p$ and Ba p levels.

A change of X-ray incidence angle from grazing to normal results in a decrease in the absorption intensity. At the O K edge, minor differences in peak intensity ratio and features are observed specially in the energy region 530 ± 10 eV, for spectra measured in the [100] and [110] directions.

With the high energy resolution, it is possible to map out very discrete energy shifts and from Fig. 4.2, a small shift of 0.1 eV photon energy is observed between spectra measured in the [100] and the [110] directions at Ti, Ba and O edges. The physical significance of the energy shift lies in the fact that a tetragonal distortion of the TiO_6 octahedra is manifested as an energy shift as reported for SrTiO_3 by changing the angle of incidence [69]. Within the BaTiO_3 surface, such a distortion can occur due to the compression or expansion of the Ti-O bond lengths along certain directions due to the presence of oxygen vacancies, formed as a result of surface sputtering and annealing treatments. The presence of domains also have an influence on the BaTiO_3 lattice and it is known that the a domains provide a maximum anisotropic lattice strain of 1.1% in the [100] direction in tetragonal BaTiO_3 at room temperature [39] which could result in an energy shift in XA spectra. However, the shift is found to be consistent at all the edges measured which might be a small problem in the data acquisition at the beamline and hence should probably be neglected.

The experimental investigations combined with theoretical calculations at the O K of BaTiO_3 also help in the confirmation of spectral features, the need for such a confirmation coming from the earlier attribution of a very similar spectrum as SrTiO_3 O K edge by Soriano and co-workers [71]. The XA spectra of $\text{BaTiO}_3(001)$ measured after the surface preparation is similar to the spectra from bulk and hence it can be understood that the electronic structure of the $\text{BaTiO}_3(001)$ surface is not altered much compared to that of bulk.

4.2.3 Resonant photoemission spectroscopy measurements

In order to study the valence states in BaTiO_3 , we made use of resonant photoemission spectroscopy (RPES) and combined it with XAS to study the occupied levels. Resonant photoemission is a good tool to investigate the Ti $3d$ - O $2p$ hybridisation in BaTiO_3 responsible for the covalent character of the bond.

In the present study, photoemission data were acquired with photon energies ranging from 455-465 eV, i.e., below and above the Ti $2p$ core level threshold. With the photon energy above the Ti $2p$ core threshold, the excitation of Ti $2p$ electrons to the conduction band can be probed. The use of deeper core levels such as $2p$ is beneficial

compared to $3p$, in a way that they induce a stronger resonant $p \rightarrow d$ transition and hence clearer variations in the valence band emission are obtained as the $2p$ threshold is passed [72].

Figure 4.3 shows the RPES spectra of the valence band region and the shallow core levels of a clean BaTiO₃ obtained with photon energies near the Ti $2p$ core level energies, at room temperature. The different features in the spectra can be identified and assigned according to available literature for BaTiO₃ [73, 54] and valence band of SrTiO₃ [74]. In BaTiO₃, the Ti $3d^0/3d^1$ levels are closer to the Fermi level, as described by the bulk band structure [10]. The feature A observed at around 1 eV binding energy is contributed by the Ti $3d^0/3d^1$ levels. This is the defect peak arising from reduced Ti³⁺ [75]. In the defect free state of BaTiO₃, Ba carries a 2+ charge, Ti is 4+ and O is 2-. Ti³⁺ is created as a result of the charge compensation for O²⁻ vacancies. Hence, the RPES spectra confirm that the half order spots obtained in the LEED images can be ascribed to oxygen vacancies due to the surface preparation treatment. A similar defect state is also discussed in the case of SrTiO₃ studied with RPES [74].

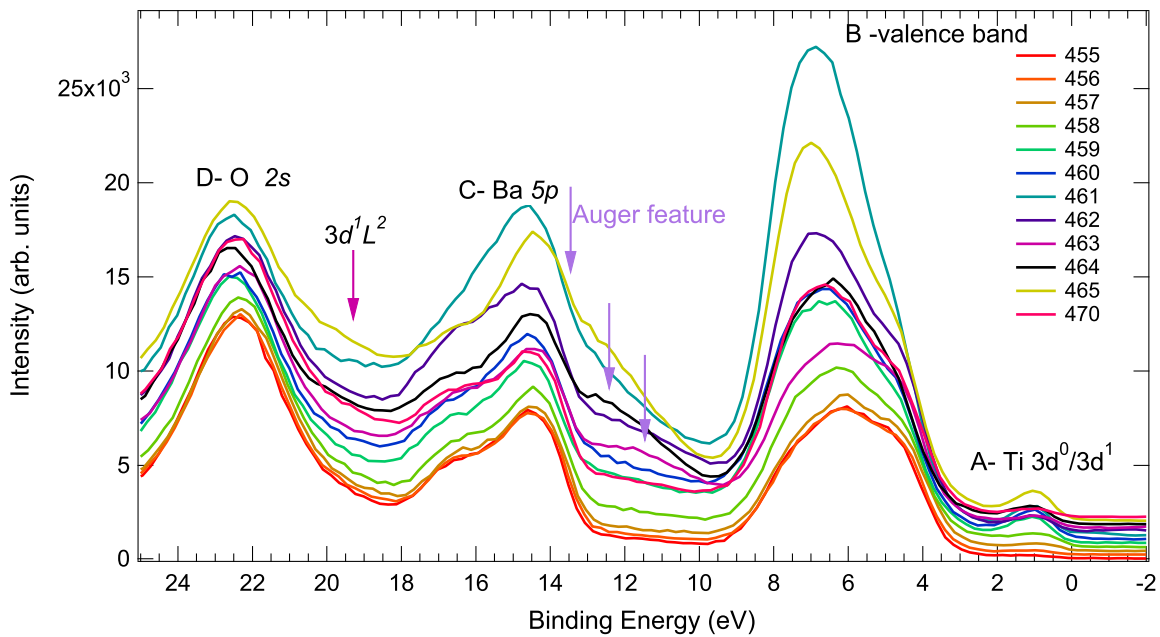


Figure 4.3: Resonant Photoemission spectra at the near valence band region of BaTiO₃ single crystal surface obtained with Ti $2p$ core level energies. The spectra are offset in the intensity axis for clarity and the photon energies are listed in figure legend. The different features are marked and are explained in the text.

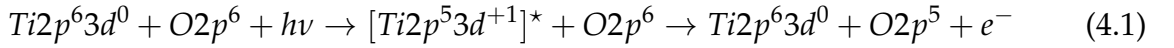
The valence band feature which extends from 3-9 eV below the Fermi Energy (E_F), labelled as B, is attributed to the O $2p$ - O $2p$ non-bonding states closest to the VBM and the O $2p$ -Ti $3d$ bonding levels at higher binding energies. The broad feature C at a slightly higher binding energy is the contribution from the spin-orbit split doublets of Ba $5p$ states and extends from 13- 18 eV. For BaTiO₃(001), the reported binding energy values corresponding to Ba $5p_{3/2}$ are 14.2 and 14.3 eV, for Ba $5p_{1/2}$ are 16.1 and 16.2 eV [54, 73]. The contribution from O $2s$ is observed at around 22 eV binding energy and is

denoted D. The reported binding energies for O 2s in BaTiO₃(001) are 22.2 and 22.1 eV [54, 73] which is consistent with our observations.

The spectrum in Fig. 4.3 shows clear intensity enhancements at features A, B and C at some photon energies. The resonance at feature B is the outcome of two concurrent processes - excitation of Ti 2*p* electrons to the 3*d* states and de-excitation of the valence band electron from O 2*p*.

The direct photoemission process involves the ejection of an electron from the initial state $2p^6 3d^n$ to form the $2p^6 3d^{n-1}$ final state. In the resonant photoemission process, an electron from the $2p^6$ core level gets excited to the 3*d* level leading to the $2p^5 3d^{n+1}$ excited state, which subsequently decays via an Auger process giving rise to the $3d^{n-1}$ final state. This results in the emission of electrons possessing a kinetic energy equivalent to the direct photoemission peak of the 3*d*. In a defect free BaTiO₃, the Ti 3*d* is unoccupied and therefore, the resonance occurs via an interatomic process due to the hybridisation of O 2*p* and Ti 3*d* levels similar to that observed in the case of TiO₂ [76]. Hence the excitation process remains the same as described involving Ti $2p^6$, but the decay process occurs via O 2*p* orbitals.

The resonant photoemission process in BaTiO₃ can be represented as,



where the asterisk denotes the excited state.

Therefore the intensity enhancement at feature B asserts the contribution of Ti 3*d* in the valence band and the hybridisation between Ti 3*d* and O 2*p* orbitals, although this hybridisation is well established.

The defect sites are created due to the oxygen vacancies and consequent charge balance in Ti as Ti³⁺. From Fig. 4.3, resonance intensity enhancement is also found at the defect states (A), which is strong at similar photon energies to that of feature B.

Particularly important is the significant intensity increase in the energy region between 12 and 18 eV represented as C. But, if the intensity enhancement is in the Ba 5*p* region, it would indicate that the Ba levels hybridize with Ti energy levels. Hudson and co-workers have observed an intensity enhancement in RPES at the Ba 5*p* level in BaTiO₃ using 38 eV photon energy, but attributed it to the absorptions due to higher order light [73]. In the present case, since Ti 2*p* photon energies are employed, the problems with higher order light do not persist. The Ba levels were mostly discussed as non overlapping since the Ba 5*p* is almost 17 eV away from the valence band. Also, the spatial separation of Ti and Ba due to the structural arrangement prevents any overlap of states.

In order to clearly understand the results and the observed resonance enhancement in the binding energy region of 10-18 eV, we compared the results from the TiO₂(100) RPES with Ti 2*p* photon energies [77]. The results are comparable to TiO₂(100) since

BaTiO₃ comprises of similar TiO₂ octahedrons. With Ti 2*p* photon energies, Prince and co-workers observed intensity enhancement at two features with binding energies between 13-18 eV and they ascribed one of the features to an Auger peak [77]. The other peak is assigned to final states $3d^1L^2$, with two ligand holes.

From Fig. 4.3, a feature at 11 eV binding energy measured with a photon energy of 463 eV can be isolated, which is found to remain at constant kinetic energy as the photon energy is varied. The peak corresponds to a kinetic energy of 451.5 eV. Hence, this can be ascribed to L_3VV Auger peaks of titanium which appears at a kinetic energy of 451.5 eV. In addition, we can also identify another peak at higher binding energies (19 eV) corresponding to the aforementioned $3d^1L^2$ final states which is marked in Fig. 4.3. Hence, it is affirmed that the intensity changes are not related to Ba 5*p* related resonances, but to Auger electron emission lines. More theoretical investigations will be helpful to comment on the exact nature of the peak and resonating states. Comparing the intensity changes in the present work to previously reported works, suggests that the reconstruction does not change the Ti-O hybridisation.

At the O 2*s* region (feature D), no significant resonance intensity change is noted which might be due to the energy gap from the valence band thereby making it difficult to participate in the hybridisation. Also, the O 2*s* region has much smaller overlap with Ti 3*d* levels.

For all features, resonance enhancement is the strongest for the photon energies close to the peaks of the Ti $L_{2,3}$ absorption edges. Therefore the resonance PES in Fig. 4.3 can be compared to the Ti $L_{2,3}$ edge XAS given in Fig. 4.4. The Ti $L_{2,3}$ edge XAS measures the excitation from Ti 2*p* to 3*d* levels and thus probes the unoccupied valence states with Ti 3*d* character.

The XAS at the Ti $L_{2,3}$ edges are given in Fig. 4.4 along with the intensity enhancement spectra constructed from the resonance intensity increases at a fixed binding energy as indicated in the figure legend. The XAS data were recorded in total electron yield mode by measuring the drain current from the sample. The constructed spectra at 7 eV and 14.5 eV extend from 455 eV to 465 eV with 1 eV steps. At both the binding energies a resonance is observed at 461 eV and also at the Ti $L_{2,3}$ edge maxima indicating 3*d* character in both the features. The 3*d* resonance enhancement is found to be maximum at the energies corresponding to the $2p_{1/2}$ and $2p_{3/2}$ excitations of the XAS spectra. The enhancement is found to be absent in the in-between region of these two excitations. The spectrum constructed from feature C at 14.5 eV is almost similar to the one obtained from the intensities of feature B. This supports the argument that feature C can be assigned as a Ti L_3VV Auger electron emission line.

From Fig. 4.4, it can be seen that the resonant intensity enhancement corresponding to the first XAS peak is displayed only by feature A. This indicates that the transitions involve Ti 3*d* states. The distortion of symmetry around the Ti³⁺ ions due to the creation of oxygen vacancies might result in lifting the degeneracy of the t_{2g} states. This gives rise to the observed intensity enhancement at the corresponding energies of the

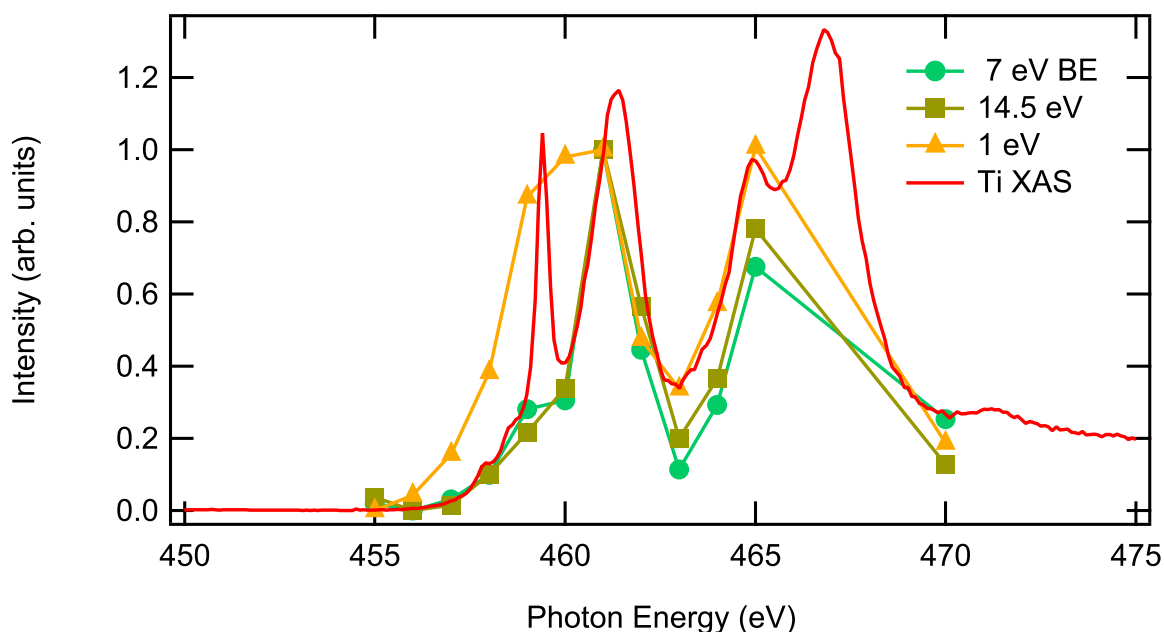


Figure 4.4: X-ray absorption spectrum at Ti $L_{2,3}$ edges measured from a single crystal BaTiO₃(001) along with the resonance intensity enhancement spectrum constructed by noting the intensity increase at a fixed binding energy as indicated in the figure legend. For comparison, the spectra are normalized to unity at 460 eV photon energy.

first L_3 edge narrow peak. Detailed theoretical calculations are necessary to understand the states further.

To conclude, the RPES measurements show resonance intensity enhancements observed at features A, B and C. The contribution of Ti states to all these features is established through comparison with the Ti L edge XA spectrum. The RPES measurements at photon energies near the Ti $2p$ threshold help to identify the Ti L_3VV Auger electron emission line.

4.3 Growth of ultrathin Fe films on BaTiO₃(001)

The deposition of Fe layers onto BaTiO₃(001) single crystal substrates is already described in chapter 3. In this section, the structural long range order and the interface stability of Fe layers on BaTiO₃(001) will be elucidated.

4.3.1 Results of LEED investigations

The structure and long range order of the Fe films have been investigated through LEED. As mentioned earlier, the BaTiO₃ single crystal substrates showed sharp LEED patterns before evaporation of Fe. On evaporation of the first few monolayers of Fe, the background intensity increased and the substrate spots became less sharp and with subsequent deposition, the spots faded away slowly indicating the absence of long range ordering of Fe atoms. Also, no distinct new features were observed in LEED.

From 6 MLE onwards, faint and broad (1 0) spots of Fe(001) are observed with the absence of substrate spots. At 8 MLE thickness, the spots became brighter suggesting better ordering. With further increase in Fe thickness, the Fe spots became sharper.

The inverted gray scale LEED images obtained from 8 MLE and 26 MLE Fe films on BaTiO₃ at 90 eV kinetic electron energy are presented in Fig. 4.5(a) and (b) along with a model for the structure of Fe on BaTiO₃ in Fig. 4.5(c). The unit cell of Fe is represented by the magenta square. As discussed above, the spots of 27 MLE Fe LEED image are sharper and brighter compared to that from 8 MLE with a less intense background. The model assumes the position of Fe atoms on top of each oxygen atom according to the theoretical calculations [8, 10].

Fe has a lattice parameter 2.866 Å and that of BaTiO₃ is 3.991 Å. Comparing the substrate LEED spots, it can be seen that Fe grows 45° rotated on BaTiO₃ in order to reduce the lattice mismatch. With the rotation of Fe unit cell by 45°, a small lattice mismatch of 1.5% is obtained. Hence the epitaxial relation is Fe [110]/ BaTiO₃ [100] which was also assumed in theoretical calculations [8].

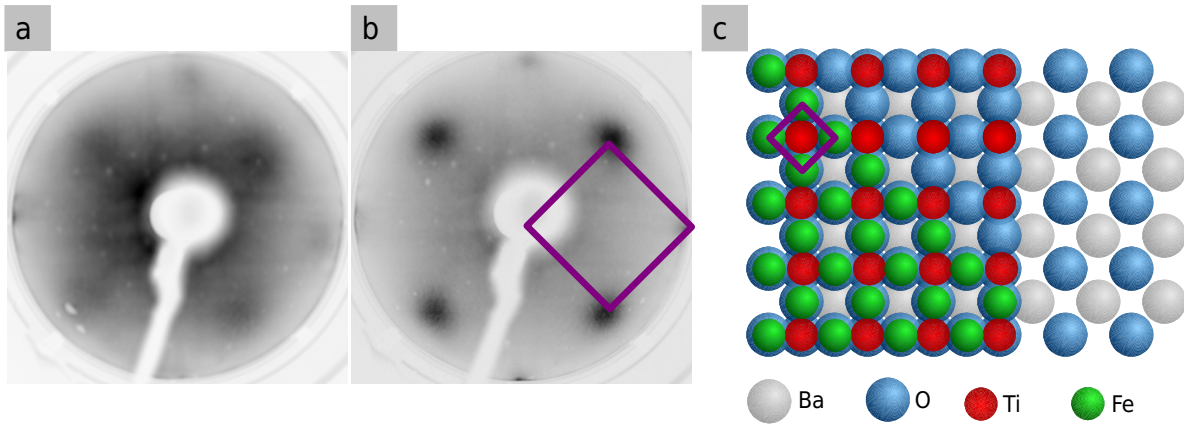


Figure 4.5: The inverted gray scale LEED images of (a) 8 MLE and (b) 26 MLE Fe thin films on BaTiO₃(001) surface recorded with an electron kinetic energy 90 eV. The magenta square represents the unit cell of Fe. (c) The structure model for Fe layers on BaTiO₃(001) assuming an Fe occupation on top of O atoms of BaTiO₃.

The spots in the LEED pattern from Fig. 4.5(a) and (b) are broad. The broadening of diffraction spots can be explained by assuming the periodic structure to be composed of islands and the island size (d_{isl}) can be approximately determined from the equation:

$$\frac{h_w}{a^*} = \frac{a}{d_{isl}} \quad (4.2)$$

where h_w is the half width of the diffraction spot, a^* the distance between two spots and a is the lattice constant corresponding to a^* [20].

In order to find out the half width of the LEED spot, a line profile can be made across the spots of the LEED image. Assuming that the broadening of the LEED spot is caused by one dimensional disorders such as islands and also by assuming uniform island size over the entire area, an island size of 18 ± 2 Å is calculated from the LEED pattern in

Fig. 4.5(b) from the (1 0) spot. Due to the presence of the very high background, it is difficult to accurately estimate the island size from the LEED pattern.

The assumption of uniform island size is valid for the metal overlayers on insulating substrates where the inhomogeneous distribution of island sizes is observed mostly [78] in the smaller thickness regime. The strain from BaTiO₃ might lead to a roughness in Fe which in turn result in the formation of islands. Moreover, the interaction between Fe and BaTiO₃ is expected to be small which will result in the large surface energy of a stretched out, flat film. Kamaratos et al. have studied the growth of Fe on SrTiO₃(001) and found the same epitaxial relationship as that for Fe on BaTiO₃(001) [40]. The observed pattern was directly correlated to a body centred cubic lattice from a (100) surface. Therefore, it can be concluded that Fe grows as a body centred cubic lattice which is the favoured crystal structure for growth under 1185 K.

4.3.2 Interface stability

The interface plays a crucial role in the applications of multiferroic materials. In this regard, the chemical stability of the interface becomes a prominent point to discuss. As mentioned in the introduction section, the first few layers of Fe on oxidic substrates such as MgO and NiO were found to be oxidised due to the interaction with the oxygen from the substrate [42, 46]. Since Fe/BaTiO₃ interface is a metal on oxide interface, it can be expected that the interface Fe is oxidized. The sharpness of the interface as well as thickness dependent changes to the electronic properties of the Fe layers deposited have been studied using XAS and XPS.

Figure 4.6 (a), (b), (c) and (d) show the Ti $L_{2,3}$, Ba $M_{4,5}$, O K and Fe $L_{2,3}$ edges XA spectra measured using linear polarized light from Fe layers of different thickness on BaTiO₃. The corresponding spectra from BaTiO₃ before evaporation of Fe films is shown along with.

The spectra after Fe evaporation shown in Fig. 4.6 (a), (b), and (c) resemble the corresponding spectra from BaTiO₃(001) before evaporation shown in section 4.2.2. The O K edge XA spectrum shows a sharp intensity decrease as a function of increasing Fe thickness and hence, the spectra are shown until an Fe thickness of 4.4 MLE. All absorption peaks including the pre-edge features are reproduced after Fe evaporation also. Apart from the decrease in intensity, no major changes like splitting of peaks or shift in energy are seen in the spectra after Fe evaporation.

The absorption spectrum of Fe shown in Fig. 4.6 (d) consists of mainly two features. The peak at 706.6 eV (L_3 edge) results from the transition of electrons from the $2p_{3/2}$ to unoccupied states. The peak at 719 eV (L_2 edge) is the result of the excitation of $2p_{1/2}$ electrons to unoccupied states. It is seen that the intensity of the peaks increases as the thickness of Fe layers is increased.

An analysis of the Fe XAS line shape yields information on the chemical state of the system. It is observed in Fig. 4.6 that all the XA spectra show typical features of

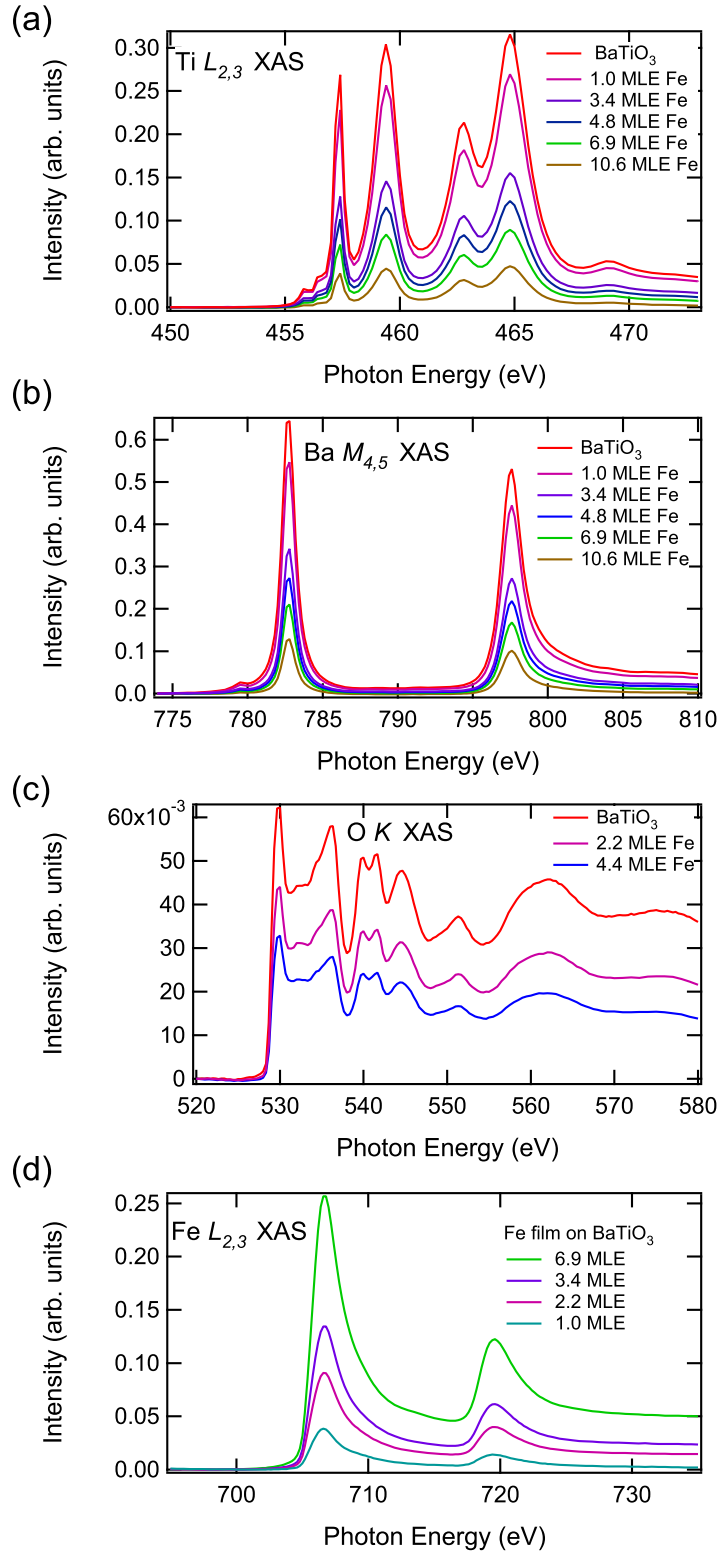


Figure 4.6: (a) Ti $L_{2,3}$, (b) Ba $M_{4,5}$, (c) O K and (d) Fe $L_{2,3}$ edges X-ray absorption spectra measured from Fe/BaTiO₃(001) with linear polarized light in grazing incidence. The corresponding Fe film thickness is mentioned in the figure legend.

metallic Fe [5]. The full width half maxima (FWHM) of all spectra at the Fe L_3 edge remained constant at 3 ± 0.1 eV, which is similar to the value obtained for Fe films

on Si(001) [79]. Hence it is inferred that there is not much changes to the electronic structure with the subsequent evaporation steps. We could not observe any splitting or shifting of absorption peaks within the experimental photon energy resolution of 0.2 eV, thereby confirming the absence of oxidation of the layers as a result of annealing. These observations indicate that the interface is a sharp and abrupt one.

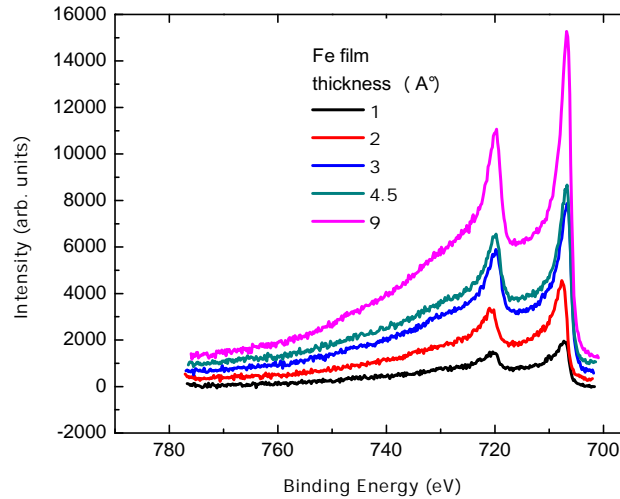


Figure 4.7: Fe 2*p* X-ray photoemission spectra of different thickness of Fe thin films deposited on BaTiO₃(001) and measured in normal emission using 930 eV photon energy. The spectra are offset in the intensity axis for clarity.

Figure 4.7 shows the Fe 2*p* photoemission spectra measured with 930 eV photon energy in normal emission. The spectrum consists of two features- 2*p*_{3/2} feature at 707 eV and 2*p*_{1/2} feature at 716 eV- with an energy separation of 9 eV. Both these peaks show a clear thickness dependence, the main features observed essentially being the same without changes to the FWHM. The spectra are shown in figure after subtracting a Tougaard background which is the most appropriate form of background subtraction for transition metals [80]. The 2*p* line shows no pronounced satellite features. After the background subtraction, the spectra do not show any new features in accordance with the assumption of the absence of oxidation at the interface.

The interface sharpness in this case depends on the affinity of Fe for O compared to Ba and Ti and on the surface free energies (or adhesion energies) of metal and oxide. The late transition metal Fe has a lower affinity due to the small negative heats of formation compared to Ba and Ti. The heat of formation (ΔH_f) of FeO is -272 kJ/mol whereas that for TiO₂ is -944.7 kJ/mol and hence the high ΔH_f of Fe compared to Ti results in a very small interaction between Fe and the substrate when Fe is grown on TiO₂ surfaces. Intermixing is usually favored in systems where the heat of formation of the alloy or the compound is lower than the substrate.

Kamaratos et al. have studied the interface between Fe films grown on SrTiO₃ [40]. According to them, the Fe/SrTiO₃(001) interface is a sharp and abrupt one and is stable

for annealing upto 800 K. Silly and Castell reported an island growth for Fe on SrTiO₃ [41]. In this context, an understanding of the wetting process in Fe/BaTiO₃ can be reached based on the criteria of electron affinity. Previous XPS studies on Fe/BaTiO₃ interface have indicated the presence of a partially oxidised Fe layer which is almost 2 nm thick [49]. But our results are in agreement with the hard X-ray photoemission spectroscopy (HAXPES) studies by Zenkevich and co-workers on Fe/BaTiO₃ where they proved the absence of oxidation [50]. In this regard, our measurements serve as a confirmation for the sharp interface between Fe and BaTiO₃.

The absence of variations at the interface might also be contributed by the reduction of BaTiO₃ substrate. The number of free oxygen at the interface might be too small to cause either the oxidation of Fe or further noticeable reduction of the BaTiO₃ surface.

To conclude, the importance of BaTiO₃ as a substrate is outlined by the absence of intermixing with the Fe layers as seen from the XAS and XPS investigations. Hence this observation and confirmation of a sharp interface opens the possibility of the growth of non-oxidic metal films (for example: that of other late transition metal elements) or 3D islands on BaTiO₃, which makes this system even more interesting for technological applications. The interface is crucial in determining the magnetic properties of the Fe layers which will be discussed in the next section.

4.4 Investigations of Magnetic properties

This section focuses on the magnetism of Fe ultrathin films on BaTiO₃(001) probed with XMCD in core level X-ray absorption. The Fe films investigated have been prepared by e-beam evaporation at room temperature and later annealed to 373 K for 10 minutes. The XA spectra have been recorded at the $L_{2,3}$ edges of Fe with two different helicities of light, ie, elliptical positive and elliptical negative. All measurements have been made with the sample at room temperature. The absorption spectra of thick Fe layers have been corrected for saturation effects [81].

4.4.1 Thickness dependence

The thickness dependence of the magnetic properties of Fe ultrathin films on BaTiO₃ have been studied by evaporating a wedge shaped Fe film. The evaporation of a wedge shaped Fe film proved beneficial since we could investigate the magnetic properties of the sample for a whole range of thickness starting from 1 Å to 20 Å. The thickness of Fe in the wedge was also accurately calculated by means of an edge jump analysis of the XA spectra [82]. The Fe layers were magnetized to saturation in the in-plane easy axis direction with a pulsed magnet which provided a 0.5 T magnetic field. From MOKE and XMCD magnetization loop measurements, the magnetic fields required for saturating the ultrathin Fe films were found to be smaller than 12 Oe. Results of MOKE experiments will be discussed in the next chapter and the magnetization loops

are presented in subsection 4.4.3.

The Fe films did not show any out-of-plane magnetism in remanence at any thickness investigated. A 0.5 T magnet was used for magnetizing in remanence and the absence of an out-of-plane magnetism could be due to the inability of the sample to reach saturation magnetization in the out-of-plane direction in remanence. To obtain a saturation magnetization along the hard axis direction a very high magnetic field of a few Tesla is usually required.

The in-plane ferromagnetism in Fe films was found to start from a thickness of 6 MLE onwards since the XMCD spectra did not show any characteristic features until an Fe thickness of 6 MLE. In Fig. 4.8, the in-plane Fe $L_{2,3}$ XAS and XMCD spectra of a 5.3 MLE Fe film on BaTiO₃ are shown. The XA spectra show typical features of metallic Fe. The resultant XMCD spectrum does not show any features at the L_2 or L_3 edges indicating the absence of ferromagnetism at this thickness.

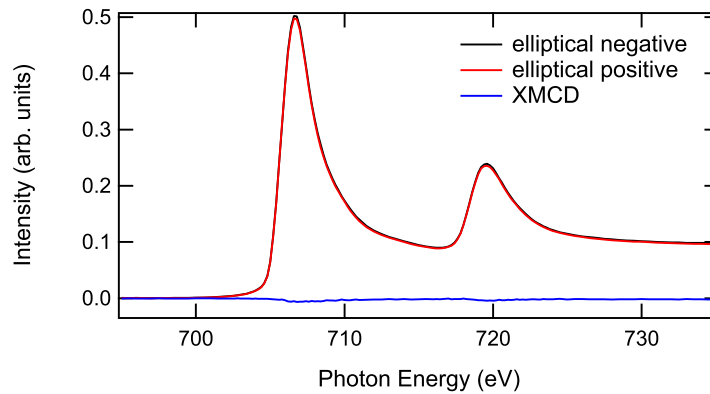


Figure 4.8: Normalized Fe $L_{2,3}$ XAS and XMCD spectra measured in the [100] direction of Fe from a 5.3 MLE thick Fe film on BaTiO₃.

Several factors can be responsible for the absence of ferromagnetism in the thin Fe films. Generally, the presence of a non-magnetic compound of Fe such as FeO might hinder the ferromagnetism in these layers. But the XPS as well as XAS analysis as discussed in the previous section rule out the possibility of the presence of FeO at the interface. In the case of Fe layers on MgO, Torelli and co-workers also discuss the absence of magnetism at the thinner layers and ascribe it to the superparamagnetic phase of iron due to the formation of Fe islands [42]. For Fe layers on NiO, the Fe layers did not show ferromagnetism at 6 MLE and below due to the effect of growth morphology, where the STM analysis has shown the presence of islands below 6 MLE and as the thickness increased, the islands became more interconnected [46]. Since our LEED investigations point to the possible formation of islands, the presence of superparamagnetic iron islands must be a viable reason for the absence of ferromagnetism below 6 MLE thickness.

Another possible explanation would be the presence of dead layers of iron at the interface which could be verified through the analysis of the evolution of ferromagnetism of the films. We also analysed on the possibility of the Curie temperature of the

thin layers being lower than the room temperature as another reason for the absence of ferromagnetism at the thin layers, which will be discussed in a following subsection.

The XMCD spectra show typical features of metallic Fe starting from a thickness of 6 MLE. The normalized in-plane XAS spectra as well as the XMCD of a thick Fe film (10.6 MLE) measured in the [100] direction of Fe are presented in Fig. 4.9. The absorption spectra show typical metallic features of Fe without any peak splittings. The Fe XMCD spectrum comprises of two features, a single negative peak at the L_3 edge and a positive peak at the L_2 edge similar to those reported for metallic Fe [16, 5]. In addition, a very small positive feature is observed at 710.2 eV for thicker Fe layers.

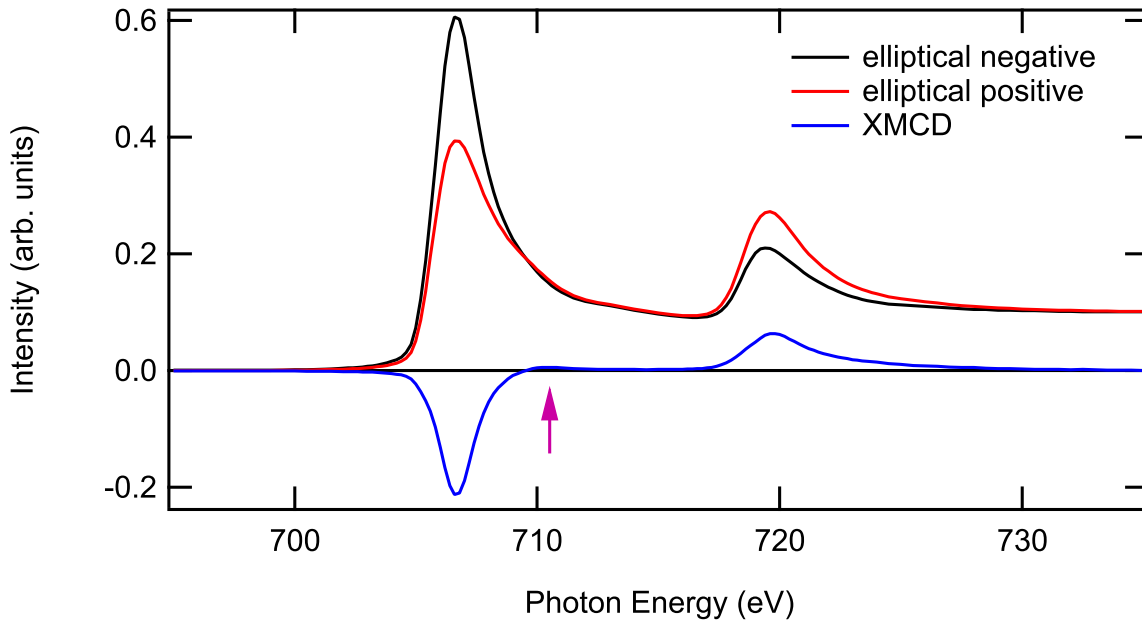


Figure 4.9: Fe $L_{2,3}$ edge XAS and XMCD spectra of a 10.6 MLE thick film on BaTiO₃ measured in the [100] direction of Fe. The XAS as well as XMCD spectra are normalized. The purple arrow shows the small XMCD signal at 710.2 eV which is discussed in the text.

In order to elucidate the thickness dependence clearly, the normalized Fe $L_{2,3}$ edge XMCD spectra for different Fe film thickness measured in the magnetic easy axis direction, i.e., [100] direction of Fe, are presented in Fig. 4.10. It is seen that the XMCD signal at both L_2 and L_3 edges increases with increasing Fe thickness starting from 6 MLE. It can be understood that as soon as the island size is larger than the exchange length, the layers become ferromagnetic [83, 42], which occurs around 8 Å for the layers investigated.

Figure 4.10 displays the smooth transition from non ferromagnetic region to fully saturated region. In addition to the L_2 and L_3 edge peaks, the small peak at 710.2 eV shows an enhancement as the thickness increases. The normalized XMCD asymmetry, shown in Fig. 4.10, which is a measure of the spin imbalance in the valence states, is calculated as $[\sigma^+ - \sigma^-] / [\sigma^+ + \sigma^-]$, where σ is the absorption cross section.

Since the measurements were taken on a wedge sample, we could measure in small thickness steps and therefore outline the complete transition. Three distinct magnetic

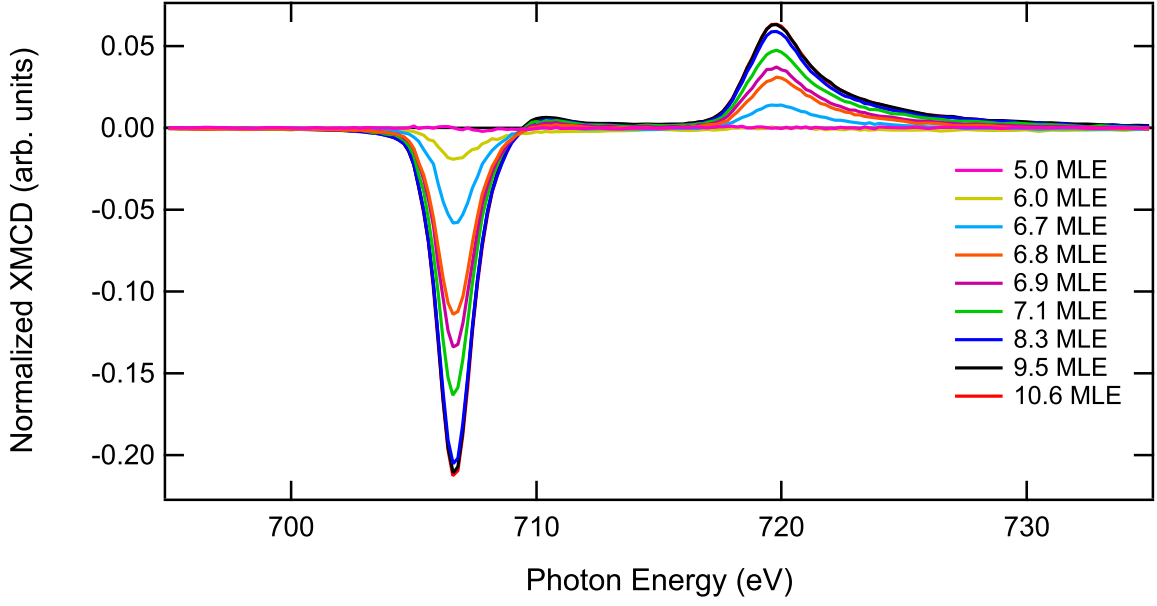


Figure 4.10: Normalized Fe $L_{2,3}$ edge XMCD spectra measured along the in-plane [100] direction of Fe for different film thicknesses. The film thickness is indicated in the figure legend.

regimes can be distinguished from Fig. 4.10. They can be termed as the onset region, intermediate ferromagnetic region and the ferromagnetic saturation region. After the onset is observed, the XMCD signal increases gradually until 8 MLE where the asymmetry values reach 21 %. This is termed as the ferromagnetic saturation region. The transition from non-ferromagnetic to saturation ferromagnetic region happens within 2 MLE which is a small thickness regime. This rapid transition can be correlated to the absence of dead layers of Fe.

A full analysis of the XMCD spectra according to the sum rules helps to calculate the absolute spin and orbital magnetic moments (m_s and m_l) accurately as a function of Fe thickness. The resultant XMCD spectra were corrected for angle of incidence and degree of light polarization and the orbital and spin magnetic moments per atom were determined based on the sum rules. Table 4.1 summarizes the variation of m_s , m_l , m_{Tot} and m_l/m_s as a function of Fe film thickness.

The magnetic moment calculations were carried out, using a value of 3.39 for the number of 3d holes ($10 - n_{3d}$) for Fe according to the previously published reports [5]. This is a reasonable assumption although the possibility of a modified band structure compared to bulk Fe which would consequently change the n_{3d} cannot be neglected. The spin moment thus calculated (m_{Seff}) contains the spin magnetic dipole term Tz ($m_{Seff} = m_s + 7/2\langle Tz \rangle$) which can be neglected for systems with cubic symmetry but is important for surfaces and interfaces [19]. The calculated spin moments in this thesis (m_s) are the effective spin moments m_{Seff} , and contains contribution from the $\langle Tz \rangle$ term.

In the original sum rule analysis, the q value which is the integral of L_2 and L_3 edges, was calculated at 760 eV. The spectra we measured had a photon energy range upto

735 eV. It is seen that the q value at 735 eV is slightly larger than that at 760 eV. We found that the correction factor for an energy range upto 735 eV should be 0.94. Since the orbital moment suffers much from the change in integration range, they are multiplied by the correction factor. The calculated and corrected values of m_l are displayed in Tab. 4.1. Since the changes in spin moment are negligible, it is not applied.

Table 4.1: Calculated effective spin and orbital moments of Fe films on BaTiO₃(001) along the [100] direction of Fe. The thickness of Fe is given in MLE and the asymmetry at the L₃ edge is given in % . The asymmetry values are given without applying correction for angle of incidence and incomplete polarization. m_S , m_l and m_{Tot} are in units of Bohr magneton per atom ($\mu B/atom$). The maximum error for thickness is ± 0.2 MLE and m_S , m_l and m_{Tot} values are 5%, 10% and 5% respectively.

Thickness	asymmetry	m_S	calculated m_l	corrected m_l	m_l/m_S	m_{Tot}
10.6	21.3	1.96	0.192	0.180	0.092	2.14
9.5	21.1	1.96	0.183	0.172	0.088	2.13
8.3	20.5	1.87	0.194	0.182	0.097	2.05
7.1	16.3	1.50	0.159	0.149	0.099	1.65
6.9	13.4	1.17	0.151	0.142	0.121	1.31
6.8	11.4	0.97	0.148	0.139	0.143	1.11
6.7	5.8	0.47	0.085	0.080	0.170	0.55
6.0	1.9					
bulk Fe [5]		1.98		0.086	0.043	2.07

The error bars in XMCD asymmetry and calculated magnetic moments signify experimental errors, the possible systematic errors related to the preparations and measurements of samples as well as those from the analysis of spectra. The estimated error in the magnetic moments reflects data noise and other uncertainties such as background subtraction from the XA spectra. The error is estimated from the variation in the magnetic moment values of subsequent measurements. The difference in calculated moments is also assessed from the measurements where the polarization is changed by keeping the magnetization constant and vice versa. The effect of different analysis procedure on the magnetic moments are also taken into account. However, the presence of error bars do not hinder further quantitative discussions. These error bars apply to all magnetic moment values calculated in this thesis.

The general trend of the calculated m_S , m_l and m_{Tot} is similar to that of the XMCD asymmetry as expected. The m_S of thick films ($1.96 \mu B/atom$) are in agreement with the reported bulk Fe values ($1.98 \mu B/atom$) [5]. The m_S values decrease gradually as the film thickness is lowered. In the thickness region between 6 and 8 MLE, the values are substantially smaller than the reported bulk values. This is related to the coalescence of small islands to grow a continuous film.

The calculated orbital moments (m_l) also show a strong thickness dependence. It is higher than the bulk Fe values [5]. A similar increase of m_l is also observed in Fe on

GaAs(001) and is attributed to the reduction in symmetry [84]. As the dimensionality decreases, an increase in the orbital moment is expected. In bulk bcc Fe the high symmetry of the cubic structure quenches the orbital moment. Hence a reduction in symmetry is accompanied by an anisotropy of orbital moments as well as enhanced values of m_l . Symmetry breaking arises from low coordination numbers and the strain due to the lattice mismatch between the layer and the substrate which is therefore predominant in the case of monolayers [84]. The highest m_l values shown in Tab. 4.1 are almost twice the reported bulk Fe values.

The total magnetic moments (m_{Tot}) follow a similar trend as the m_s values. Total moments are also low for the lower thicknesses and soon reach bulklike values for a thickness of 8.3 MLE and above. Total magnetic moment (m_{Tot}) of $2.2 \mu B$ is reported for Fe bulk-like films grown on parylene by Chen and co-workers [5]. The m_{Tot} of the thick (10.6 MLE) Fe films on BaTiO₃ films are similar to the reported values of bulk Fe.

Significantly higher m_{Tot} values are reported for Fe(001) surfaces [85, 26]. However, for Fe/MgO, where the growth mode is via the formation of islands, the enhancement of spin moments has not been observed [42]. Moreover, the bulk like moments were attained at a thickness of 5.2 MLE with bulklike orbital to spin moment ratios [42].

The ratio of m_l to m_s is independent of the number of holes and hence is a reliable quantity to compare with other published results. From Tab. 4.1, it is seen that the thinnest films exhibit largest orbital to spin moment ratios, ratios as high as 0.170 is obtained for thinner films (6.7 MLE) compared to the bulk Fe ratio of 0.043 [5]. This enhancement in ratio is contributed by the orbital moment enhancement explained for low Fe thickness.

With the increase in thickness, the ratio decreases and reaches 0.092 for a 10.6 MLE film. Considerably higher ratios were reported for Fe nano-clusters and thin films. Ratios as high as 0.075 were reported for an Fe wedge on Cu(100) as well as Fe films [82], 0.083 for Fe films [86] and 0.1 for Fe nanoclusters [87]. Small Fe nanoclusters on Ni/Cu(100) show even higher ratios than 0.1 [88]. Ohresser and co-workers distinguished different regions of Fe growth such as 1D, 2D and the corresponding ratios show a huge variation from 0.06 to 0.1 [89]. The high ratios are in accord to the formulation of island structures which is structurally different from the continuous flat film with bulk-like ratios. Since high ratios are expected for low coordinated systems, Fe on BaTiO₃ ratios reflect the transition from isolated clusters to percolated islands.

Hence, the thickness dependence of Fe XMCD along the [100] direction of Fe reveal the onset of ferromagnetism at 6 MLE for Fe films on BaTiO₃. An analysis of the XMCD spectra helps to distinguish three magnetic regions, namely, the non-ferromagnetic region, the intermediate ferromagnetic region and the ferromagnetic saturation region.

Comparison to Theory First principles calculations within the framework of Density Functional Theory have been used to investigate the magnetism of 1-3 MLE thick Fe films on BaTiO₃ [11]. The characteristic XMCD features have been found to be depen-

dent on the interface structure [11]. Our measurements at room temperature did not yield any XMCD signal until 5 MLE contrary to the theoretical predictions [11, 10]. However, the calculated critical temperature of the ultrathin Fe layer is between 170 to 230 K [11]. Our experiments were performed at room temperature and this could serve as a reason for the absence of XMCD at the very thin layers. The XMCD spectral features obtained for the thick layers resembles the calculated XMCD signal of bulk Fe [11].

First principles calculations on Fe/BaTiO₃ predict enhanced magnetic moments for Fe monolayers [10]. However, due to the experimental problems involved, for example, formation of Fe islands, possibly low Curie temperature for the very thin layers, it is difficult to realize the ferromagnetism and consequently magnetic moments until 6 MLE. Even for the transition layers, the magnetic moment observed here is less than that of bulk.

4.4.2 Direction dependence

The direction dependence of magnetism in the Fe films has been investigated with the help of XMCD measurements in different directions by changing the azimuthal angle. The film thickness has been calculated independently for each measurement. The angle dependent XAS has also been measured for individual uniform samples and compared to the wedge data.

The measurements have been taken in three azimuthal directions with respect to Fe. The [100] direction of Fe was chosen because the magnetic easy axis in bulk Fe is reported to be along [100] [25]. Measurements along two other directions, the [110] and the [1 $\bar{1}$ 0], have been taken by rotating the azimuthal angle of the crystal by 45° in either directions with respect to the Fe[100] direction.

The normalized XMCD asymmetries at the L_3 edge for all three directions investigated are plotted in Fig. 4.11 as a function of Fe layer thickness. In Fig. 4.11, notable differences are observed in the ferromagnetic onset, transition and saturation regions along the different directions. The ferromagnetic onset thickness for the [100] direction is 6 MLE, which reduces to 5.6 MLE and 5.0 MLE along the [110] and [1 $\bar{1}$ 0] directions. Most importantly, the asymmetry values below 6.7 MLE are the highest in the [110] direction and that above 6.7 MLE, are the highest along the [100] direction. For thick layers, the maximum asymmetry along the [110] direction is 16.0% whereas that in the [1 $\bar{1}$ 0] is 17.3%. However, in the [100] direction the maximum asymmetry is 21.3%. The asymmetry values obtained along the [100] direction is almost 20-25% higher than that of the other two directions. The transition region characteristics are also different in the different directions. In the transition region, asymmetries in the [110] and [1 $\bar{1}$ 0] directions were larger for the thin films of Fe. Thus, indeed at this thickness the easy axis is not along the [100] direction.

This indicates a change in easy axis as a function of Fe film thickness. The thin films

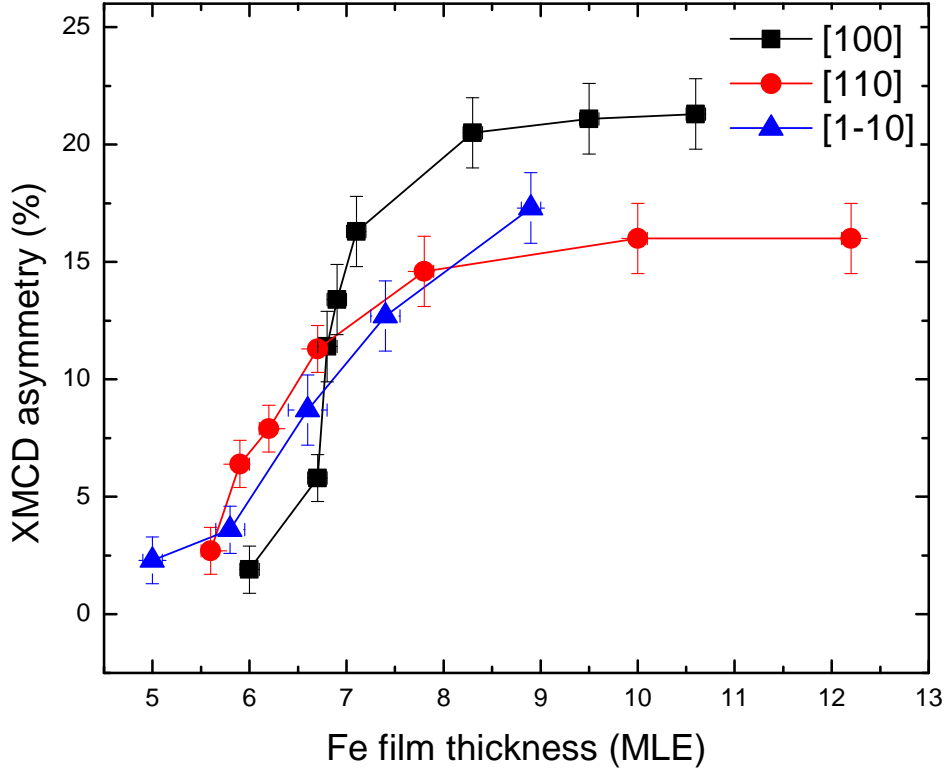


Figure 4.11: XMCD asymmetry measured at the Fe L_3 edge along three different azimuthal directions with respect to the Fe film, plotted as a function of Fe film thickness. The different directions [100], [110] and $[1\bar{1}0]$ with respect to Fe, are indicated in the figure legend.

have an easy axis along the [110] direction and the thick films (above 6.7 MLE) have an easy axis along the [100] direction of Fe. A preference in magnetisation direction, in other words, a magnetic anisotropy is observed above and below 6.7 MLE. At the transition thickness, the anisotropy vanishes and all directions show equivalent asymmetries.

The change of magnetic easy axis (in-plane) may also be termed as the in-plane spin reorientation transition (SRT). In order to check spectral changes in the XMCD along other directions, the XMCD spectra of the different Fe layer thickness measured along the [110] and $[1\bar{1}0]$ directions of Fe are presented in Fig. 4.12. From Fig. 4.12, a smooth variation of XMCD signal in the $[1\bar{1}0]$ and [110] directions of Fe is observed as a function of Fe thickness. Moreover, the spectra do not show any pronounced differences of features compared to the [100] direction. Apart from the slightly different ferromagnetic onset thickness, the XMCD spectral features gradually increase as the film thickness increases. The small positive feature at 710.2 eV also follows the same change as that of L_3 edge asymmetry.

The magnetic moments calculated from a few representatively selected thickness are

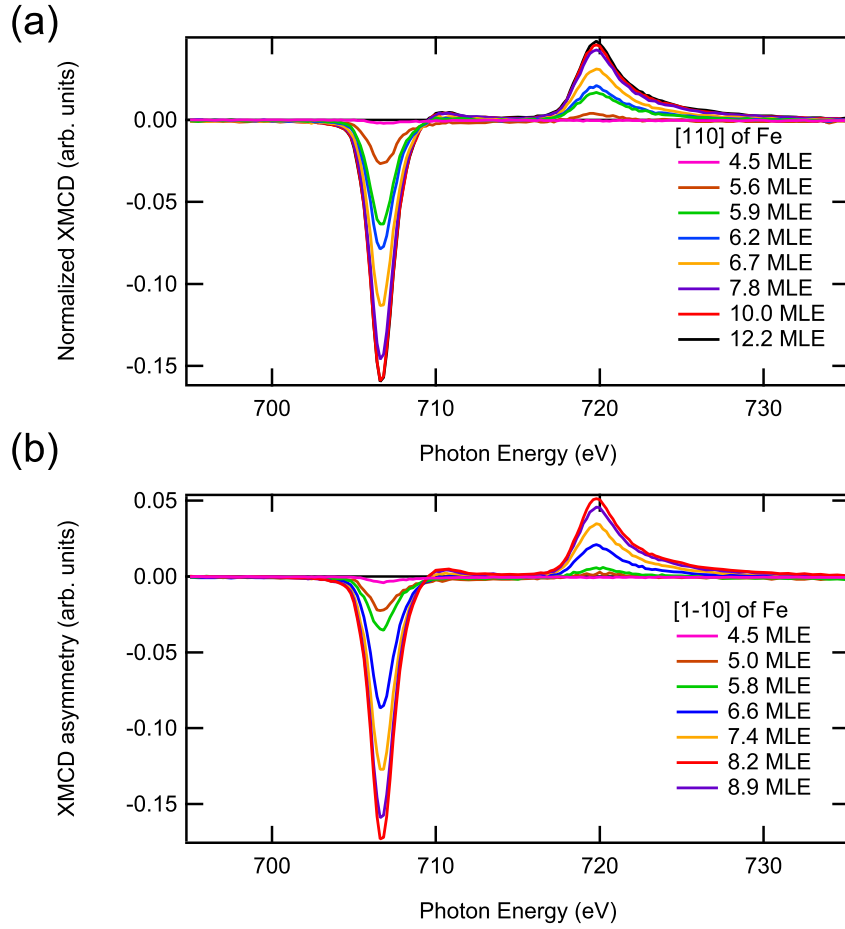


Figure 4.12: Variation of XMCD as a function of film thickness measured at the Fe $L_{2,3}$ edges in the (a) [110] and (b) $[1\bar{1}0]$ directions of Fe. The XMCD spectra are normalized.

summarized in Tab. 4.2 and Tab. 4.3 for the directions [110] and $[1\bar{1}0]$ of Fe and can be compared to the ones listed in Tab. 4.1 for the [100] direction. In general, the calculated magnetic moments display a trend in agreement to that observed for asymmetry.

For thick Fe films, the m_S and m_{Tot} values along the [110] and $[1\bar{1}0]$ directions are less than that of [100] direction. The maximum value of m_{Tot} calculated in the [110] direction is $1.58 \mu_B$ and that in the $[1\bar{1}0]$ is $1.70 \mu_B$, whereas the m_{Tot} along the [100] direction is $2.14 \mu_B$ which is similar to the bulk Fe value indicating that the magnetic easy axis is parallel to the [100] direction. But, for the thin layers, the m_S and m_{Tot} values are higher than that along the [100] direction. For thin layers, the magnetic moment values are slightly larger in the [110] direction compared to the $[1\bar{1}0]$ direction.

The orbital moments (m_l) also show a similar trend to that of m_{Tot} . In metal films, the maximum m_l values have been reported for the easy axis due to the correspondence between magneto-crystalline anisotropy and the anisotropy in m_{orb} [6, 90]. This also proves the point that the easy axis for the thin films described in the present work lies parallel to [110] which changes to [100] for thick films.

Along the [110] and $[1\bar{1}0]$ directions, the m_l/m_S ratio is high for the thin films and decreases on increasing the film thickness. For all thicknesses investigated, the m_l/m_S

Table 4.2: Calculated effective spin and orbital moments of Fe/BaTiO₃ layers along the [110] direction of Fe. The thickness is given in MLE and the asymmetry is given in % for the L_3 edge. The m_S , m_l and m_{Tot} are in units of $\mu_B/atom$.

Thickness	asymmetry	m_S	calculated m_l	corrected m_l	m_l/m_S	m_{Tot}
12.2	16.0	1.45	0.142	0.133	0.092	1.58
10	16.0	1.42	0.160	0.150	0.106	1.57
7.8	14.6	1.30	0.135	0.127	0.098	1.43
6.7	11.3	0.98	0.125	0.118	0.120	1.10
6.2	7.9	0.65	0.110	0.103	0.158	0.75
5.9	6.4	0.54	0.080	0.075	0.139	0.62
5.6	2.7					

Table 4.3: Calculated effective spin and orbital moments of Fe films on BaTiO₃ along the $[1\bar{1}0]$ direction of Fe. The film thickness is given in MLE and the asymmetry is given in % for the L_3 edge. The m_S , m_l and m_{Tot} are in units of $\mu_B/atom$.

Thickness	asymmetry	m_S	calculated m_l	corrected m_l	m_l/m_S	m_{Tot}
8.2	17.3	1.55	0.164	0.154	0.099	1.70
7.4	12.7	1.08	0.146	0.137	0.127	1.22
6.6	8.7	0.70	0.117	0.110	0.157	0.81
5.8	3.6					
5.0	2.3					

ratio is higher compared to the reported bulk Fe values. Any change in the ratio indicates modifications in the electronic structure [42, 91]. Tab. 4.1, shows that the m_l/m_S ratio for the thin layers in the [100] direction is enhanced compared to that of thick layers. In comparison to bulk Fe, the enhancement in the ratio can be calculated as, $(ratio_{film} - ratio_{bulk})/ratio_{bulk}$, where the $ratio_{bulk}=0.045$ [92, 5]. From this, an enhancement of 278% is calculated for the 6.7 MLE Fe along the [100] direction in comparison to bulk.

The basic reason behind the anisotropy in the magnetic moments is spin-orbit coupling [26]. The presence of anisotropy in the magnetic moments of Fe indicates that the Fe 3d levels contribute to the magnetic anisotropy. The enhancement in $(ratio_{film} - ratio_{bulk})/ratio_{bulk}$ also shows enhanced spin-orbit interaction [91]. The enhanced spin-orbit interaction lifts the degeneracy of the d-orbitals and thereby increases the orbital moments. So, we arrive at the conclusion that the thin Fe films are dominated by spin-orbit interaction which results in the increase of orbital moments and the orbital to spin moment ratio. In a simple approach, it can be assumed that the interface magnetic moment anisotropy originates as a result of the interface bonding of Fe-Ti orbitals. Although the O 2p-Ti 3d is supposedly the strong bond in

Fe/BaTiO₃ films, the Fe-Ti bonding might be sufficiently strong to redirect the orbital magnetic moment owing to spin-orbit interaction. When the Fe thickness increases, the spin-orbit coupling is quenched and the Fe *d*- orbitals become more degenerate. This might occur by changing the electron occupation consequently giving rise to a change in magnetic easy axis. In addition, the small deviations observed in the ferromagnetic onset thickness along the different directions hint at the presence of anisotropic interface bonding. The interaction of Fe-Ti is in agreement with the theoretical calculations described in [8].

In Fig. 4.10 and 4.12, a small positive XMCD feature at 710.2 eV is visible above 6.7 MLE. This feature has been observed for Ga_xFe_{1-x} and attributed to the transitions from the 2*p* core level to the unoccupied majority spin band [93]. This argument is also supported by earlier theoretical studies [94, 95]. The main negative Fe XMCD peak at the *L*₃ edge is due to the transitions to unoccupied minority spin band [93, 94, 95]. From Fig. 4.10 and 4.12, a gradual transition from negative intensity to positive intensity is visible at the 710.2 eV feature indicating the absence of holes in the majority spin band below 6.7 MLE. Arenholz and co-workers correlated the magnetoelastic energy to the electronic states located near the Fermi level [93] and it is known that the magnetoelastic energy is directly proportional to the spin-orbit splitting [96]. However, it has been reported for Fe layers on GaAs that the magnetoelastic interactions do not play the key role in SRT [97].

An in-plane spin reorientation transition has been reported for many Fe thin film systems [98, 99]. Another possible reason behind the SRT in thin films is governed by strain from the substrate. In the present case, the lattice mismatch is small, thereby only a small amount of strain from BaTiO₃ to Fe is expected. However, the sign change of the small XMCD feature reveals the absence of holes in the majority spin band which indicates that the Fe layers exhibit opposite sign in magnetoelastic strains with respect to bulk strain. SRT is reported for Fe layers on MgO at around a similar Fe thickness [99], which helps to neglect strain as the primary reason for the transition since the lattice mismatch for Fe on MgO is higher (3.9%) compared to BaTiO₃ (1.5%) which did not result in any change in the SRT transition thickness. Hence the assumption of negligible strain effects seems inevitable.

An in-plane rotation of the magnetic easy axes with increasing film thickness is observed for La_{0.67}Sr_{0.33}MnO₃ thin film on NdGaO₃(112) by Nishikawa and co-workers and is ascribed to the gradual relaxation of the planar asymmetric distortion of the surface unit cell of NdGaO₃(112) with increasing film thickness, changing the crystal symmetry from monoclinic to orthorhombic [100]. They also observed a change in the in-plane magnetic anisotropy from uniaxial to biaxial as the film becomes thicker [100]. Similar to their conclusions [100], we can expect a relaxation of the BaTiO₃ surface leading to less strain in thicker Fe layers and subsequent changes to the magnetic easy axis. The reported observations of uniaxial anisotropy of Fe layers on BaTiO₃ for small thickness which changes to biaxial anisotropy [39] serves as a support for this.

Hence, another interesting point which requires detailed investigations in this regard is the interactions within the Fe layers on BaTiO₃.

Figure 4.11 and the magnetic moment calculations reveal that the local magnetization exhibits a strong azimuthal dependence. For a system magnetized along the in-plane magnetic easy axis, the magnetization in the direction of the field is $M_s \cos \phi$ [101], where ϕ is the angle between the applied field and the easy axis. The magnetization at another angle ϕ_h is given by the component of magnetization in the direction of the field i.e, $m_h = \cos(\phi - \phi_h)$. By this relation, 70% of the magnetization value is expected at an angle 45° away from the easy axis. This matches well with our experimental observations and explains the quantitative differences in asymmetry and magnetic moment along the different directions.

Thickness dependent in-plane SRT in the ultrathin Fe films on BaTiO₃(001) has also been observed through other experimental techniques such as MOKE. MOKE measurements on this system reveal an SRT at the same Fe film thickness as that observed via XMCD [102].

The consistency of results was checked in several repeated experiments with different samples. The results obtained on the wedge samples were also compared to the layer by layer grown uniform film samples. The evolution of magnetism in the uniform film sample along the [100] direction is similar to that observed for the Fe wedge shaped film sample. However, the interesting point is the difference in magnetic properties noted along the [110] direction of Fe. The intermediate region is of particular interest and this has been studied in detail. Interestingly, at higher thickness (around 29 MLE) the magnetism along the [110] direction is similar to that observed for the [100] direction. In order to see the trend more clearly, the calculated magnetic moments of a few selected films in the [110] direction of Fe are listed in Tab. 4.4.

Table 4.4: Calculated effective spin and orbital moments of Fe/BaTiO₃ films along the [110] direction of Fe measured from uniform thin film samples. The thickness of Fe film is given in MLE. m_S , m_l and m_{Tot} are in units of $\mu B/atom$.

Thickness	m_S	m_l	m_l/m_S	m_{Tot}
28.6	1.94	0.109	0.056	2.05
14.3	1.62	0.099	0.060	1.72
8.6	1.30	0.104	0.080	1.40
5.7	0.84	0.107	0.096	0.95

The onset of ferromagnetism for the uniform film sample (5.7 MLE) is similar to that of the wedge sample (5.6 MLE). The width of the transition regime is also consistent to that of the wedge sample. The m_S , m_l and m_{Tot} values calculated from the 5.7 MLE uniform film are higher than the values obtained from the wedge film sample. For all Fe thicknesses investigated, the m_l/m_S ratios from the thin uniform film sample

are significantly lower to that from the wedge sample. The orbital moment (m_l) values except that for 5.7 MLE are small in the uniform film. m_S and m_{Tot} values of the 8.6 MLE uniform film is similar to that of the wedge sample. However, at higher thickness, the m_S and m_{Tot} values are higher in the uniform film samples.

The results from the investigations of uniform film sample clearly illustrates the effect of growth on the magnetic properties of the film. The magnetic moments presented in Tab. 4.4 point to the quality of the film and it can be understood that layer after layer evaporation and intermittent annealing has helped to improve the film structure, the effect of which is reflected as a smaller m_l/m_S ratio compared to the wedge shaped film. The different regimes of magnetic behavior are the consequence of the different growth regimes. Evidently the magnetic properties can be correlated to the growth which in turn to structure. The bulklike total magnetic moment observed for the thick layers in the [110] direction points to the possible complete percolation of small islands into a uniform film and the presence of ferromagnetism as a result of long range order at the higher thickness.

In short, the direction dependence of XMCD investigated on the Fe ultrathin films reveal an in-plane SRT at a thickness of 6.7 MLE. The observed SRT is explained by taking spin-orbit interactions into consideration.

4.4.3 Magnetization loops

In-plane magnetization loops were acquired for two different Fe thicknesses in the [100] direction of Fe.

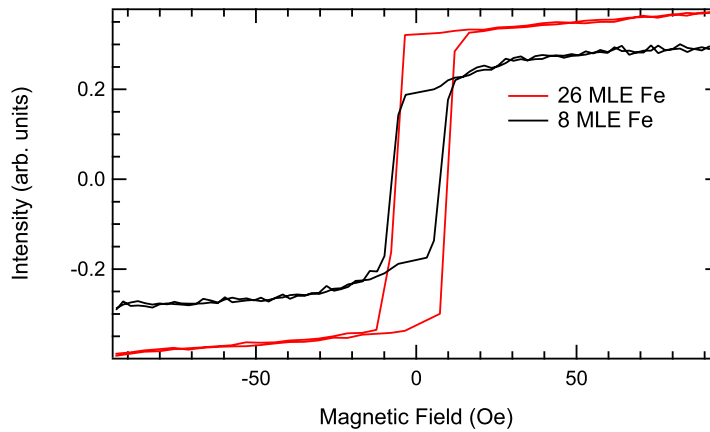


Figure 4.13: Magnetization loops obtained from XMCD at the L_3 edge energy maxima for two different Fe thicknesses along the [100] direction of Fe.

Figure 4.13 illustrates the magnetization curves along the [100] direction of Fe thin layers on BaTiO₃ for two thickness of Fe investigated: 8 MLE and 26 MLE. The two different thicknesses were chosen according to the previous LEED investigations- 8 MLE in the thin film regime and 26 MLE in the thick film regime. As the film thickness increases, the loops become vertically longer corresponding to the increase in mag-

netization. The shape of the loop of 26 MLE film is rectangular and the coercivity is found to be low. The coercivity of both the films were found to be similar and it did not change with the increase in thickness.

The shape of the magnetization loop for the 8 MLE Fe in Fig. 4.13 is slightly s-like. This indicates the possible presence of a uniaxial anisotropy near the SRT thickness which gets dominated by bulk magnetocrystalline anisotropy for thick films. This is also supported by the observation of a uniaxial anisotropy in Fe films on BaTiO₃ which changes to biaxial with thickness [39], while the loop for the 26 MLE is predominantly contributed by the magnetocrystalline anisotropy as exhibited by the rectangular shape. The presence of uniaxial anisotropy has been reported for thin Fe layers on GaAs [97, 51], where the influence of interfaces on the magnetic anisotropies is established. This strengthens the assumption about the role of Fe/BaTiO₃ interface in the SRT and the explanation of spin-orbit coupling induced anisotropic interface bonding seems to be a plausible cause for SRT.

4.4.4 Temperature Dependence

It is well known that temperature has a profound impact on the magnetic properties of ultrathin films. Of special mention is the Curie temperature of thin films which is found to be different from bulk [103]. In order to understand the effect of temperature on the magnetism of Fe films on BaTiO₃, the XMCD spectra were compared as a function of thickness at two different temperatures. Figure 4.14 gives the dependence of the XMCD L_3 asymmetry as a function of thickness in the [110] direction of Fe.

From Fig. 4.14, it can be seen that for 150 K, the onset of ferromagnetism is observed at 5 MLE Fe whereas it is 5.7 MLE at room temperature. The slightly earlier onset of ferromagnetism could be due to the Curie temperature at this thickness being lower than the room temperature. A decrease of Curie temperature is reported for decreasing thickness of Fe films on MgO(100) [104]. Similar to 300 K, the transition to the ferromagnetic XMCD is rapid for 150 K and takes place within two monolayers. The asymmetry at these two regimes, namely the onset and the transition region, is quite equal at both temperatures. The two plots diverge at higher thickness showing a prominent difference in asymmetry between 150 and 300 K. The bulk Fe layer asymmetry at 150 K is almost 24% which is higher than that for the same thickness layer at 300 K. This increase in asymmetry is a measure of the enhancement of magnetism at lower temperatures for higher thickness of Fe.

The spin and orbital moments are calculated for the Fe layers XMCD measured at 150 K according to the sum rules and are displayed in Tab. 4.5. The variation of m_S , m_l , m_{Tot} and m_l/m_S resembles that of asymmetry. The thick layers (26 MLE) show bulklike m_S and m_{Tot} values. However, m_l as well as m_l/m_S values show enhancement. The m_l/m_S is higher than bulk Fe for all thicknesses investigated due to the m_l increment which happens as a result of symmetry reduction at the surface as expected for thin

films [84].

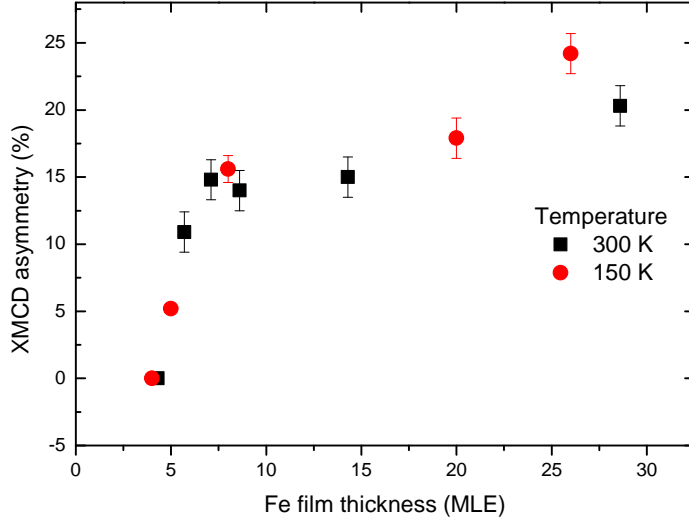


Figure 4.14: XMCD asymmetries of Fe films on BaTiO₃ at 300 K and 150 K measured in the [110] direction of Fe and plotted as a function of thickness. The corresponding temperatures are indicated in the figure legend.

Table 4.5: Magnetic moments calculated from Fe/BaTiO₃ XMCD measured at 150 K for different thicknesses in the [110] direction of Fe. The thickness is given in MLE and the asymmetry is given in % for the L_3 edge. m_S , m_I and m_{Tot} are in units of $\mu_B/atom$.

Thickness	asymmetry	m_S	m_I	m_I/m_S	m_{Tot}
26	24.2	2.08	0.117	0.056	2.2
8	15.2	1.48	0.104	0.07	1.584
5	5.2	0.35	0.053	0.147	0.403

In general, the magnetism at lower temperature is found to be higher than that at room temperature. Sahoo and co-workers [9], investigated the magnetic properties of a 10 nm Fe film on BaTiO₃ and observed a difference between the heating and cooling branches in magnetization which they attributed to the pinning of BaTiO₃. Similar effects could be observed in the present study but the difference is small since the thickness of Fe used here is also small. Magnetic moments calculated for Fe clusters show a decrease with increasing temperature [105]. The increase in magnetization might also be contributed by the substrate phase transition with temperature. At 150 K, BaTiO₃ is in the rhombohedral phase. The transition from room temperature tetragonal to 150 K rhombohedral alters the magnetoelastic coupling and strain which in turn affects the magnetization values. The magnetic properties of Fe film at 150 K could be modified due to the lattice distortions of the underlying substrate through the magnetoelastic coupling at the interface.

Temperature dependence of spontaneous magnetization at low temperature is higher according to Bloch's law [106],

$$M(T) = M(0)[1 - (T/T_C)^{3/2}] \quad (4.3)$$

where $M(0)$ is the spontaneous magnetization at absolute zero and T_C is the Curie temperature. Therefore, at higher temperatures, a decrease in spontaneous magnetization is expected.

According to Equation 4.3, if the measurement temperature is closer to the Curie temperature, a higher difference in the magnetization values between the two temperatures is expected. For thin layers, it is well known that the Curie temperature is smaller than the bulk value. Hence, for thin films, a larger difference between the 300 and 150 K magnetization can be expected. On the contrary, in the present case, larger differences in the magnetization values are obtained for the thick layers. This indicates that the temperature dependency is weak for the Fe layers and the observed differences can indeed be caused by the BaTiO₃ phase change induced strain on Fe. In this regard, more measurements in the vicinity of the phase transition temperature would prove to be helpful.

4.4.5 Induced magnetic moments at Ti atoms

XAS and XMCD spectroscopy were employed in this work to study if the Fe atoms induce magnetic moments on the interface Ti and O atoms.

The XA spectra measured at the Ti $L_{2,3}$ edges and the resultant XMCD spectra from BaTiO₃ and Fe films on BaTiO₃ are shown in Fig. 4.15 (a) and (b). The absorption spectra are measured in the [100] direction of BaTiO₃ after depositing 8.2 MLE Fe. From Fig. 4.15 (b), it is clear that the features of the XMCD spectra obtained from the 8.2 MLE Fe on BaTiO₃ sample is similar to those measured from clean BaTiO₃(001) single crystals before evaporation of the Fe film. The spectra consist of a prominent positive feature at 457.1 eV followed by three negative features at higher energies. However, the corresponding absorption spectra indicated a very small energy shift between the two light helicities. The shift might be arising from some data acquisition problems at the beamline and hence does not have much physical significance. It is seen that if one of the XA spectrum is shifted by 0.005 eV, most of the features in the resultant XMCD spectrum vanishes. Although the XMCD spectrum in Fig. 4.15 (b) resembles some of the Ti $L_{2,3}$ XMCD spectra published [107], the presence of an XMCD spectrum before the evaporation of Fe helps in the analysis. Hence, from the similar XMCD features observed with and without Fe, it can be understood that the XMCD spectrum after Fe evaporation is the result of a small shift and a slight offset of one of the absorption spectrum. Hence, the conclusion is that the Ti L edge do not show the presence of induced magnetic moments.

First principles calculations on the Fe/BaTiO₃ multilayers predict the presence of an

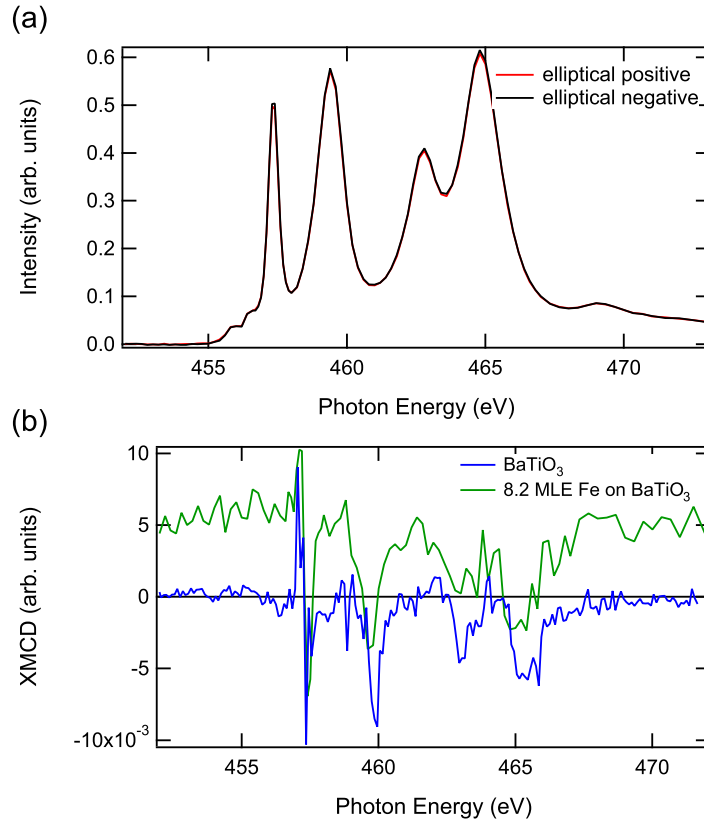


Figure 4.15: Ti $L_{2,3}$ edge (a) XAS and (b) XMCD spectra measured from clean BaTiO₃ and Fe/BaTiO₃ in the [100] direction of BaTiO₃ with samples at room temperature. The XMCD spectra in (b) are offset in the Y-axis for clarity.

induced magnetic moment on Ti and O [8, 10, 108]. The absence of an XMCD signal in the present case is possibly because the induced spin polarization on Ti 3d was too weak at room temperature to give rise to a magnetic moment at Ti. X-ray resonant magnetic scattering (XRMS) measurements have revealed the presence of a magnetic signal at Ti atoms on Fe/BaTiO₃ interface owing to the spin polarization of Ti atoms [109]. They have discussed that the detection of XMCD signal from Ti is challenging since the signal originates from the very first atomic layer of BaTiO₃ [109]. This could be another reason for the absence of a Ti XMCD signal. The investigation of spin polarization at Ti by more sensitive techniques such as XRMS would be helpful to resolve this issue completely.

4.5 Conclusions

The long range order and the electronic structure of the BaTiO₃(001) single crystal surface after the surface preparation have been investigated with LEED, XAS and RPES measurements. The presence of sharp first order LEED spots indicate good crystallinity and long range order. The presence of half order spots at some kinetic electron energies indicate a $c(2 \times 2)$ reconstruction preferably due to oxygen vacancies. The

available literature suggests a correlation of the $c(2\times 2)$ reconstructed surface to a TiO_2 surface termination. The XAS measurements compared to theoretical investigations help to unravel the electronic structure of the BaTiO_3 surface. The resonant PES measurements on the clean BaTiO_3 surface using photon energies in the range of $\text{Ti } 2p$, led to the observation of a $\text{Ti } L_3VV$ Auger peak near the valence band region.

Epitaxial Fe ultrathin films have been grown on BaTiO_3 by electron beam evaporation. The growth of Fe layers and the interface stability in $\text{Fe}/\text{BaTiO}_3(001)$ have been studied in detail with the help of LEED, XPS and XAS. The Fe films did not show a LEED pattern until a thickness of 6 MLE owing to the lack of long range order possibly caused by the growth of Fe as islands which is indicated by the broad LEED spots obtained from Fe thickness higher than 6 MLE. The FWHM at the Fe L_3 edge XAS (3.0 ± 0.1 eV) indicated the absence of changes to the Fe electronic structure. XAS measurements at the Ti $L_{2,3}$, Ba $M_{4,5}$ and O K edges revealed the absence of spectral shift and splitting. This is ascribed to the lower tendency of oxide formation of Fe compared to Ti as well as the presence of a reduced interface. Hence, it is inferred that the interface from BaTiO_3 to Fe is abrupt.

The magnetic properties of the as-prepared films have been investigated with XAS and XMCD. XMCD measurements reveal the onset of ferromagnetism from 6 MLE onwards along the $[100]$ direction of Fe and the asymmetry values reaches bulk-like within a thickness range of 2 MLE. The ferromagnetic onset thickness corresponds to the appearance of a LEED pattern, thereby indicating the correlation between magnetism and structural order in ultrathin films. The nonferromagnetic region (upto 6 MLE) is attributed to the possible growth mode of Fe as islands. The effective spin moments, orbital moments and the total magnetic moments per atom for different Fe thicknesses have also been calculated. The m_S and m_{Tot} of thick films ($1.96, 2.13 \mu\text{B}/\text{atom}$) are in agreement with the reported bulk Fe values ($1.98, 2.2 \mu\text{B}/\text{atom}$). However, the m_l values and consequently m_l/m_S values show an enhancement which might be due to a symmetry reduction at the surface. The m_S and m_{Tot} of thin films were less in comparison to Fe bulk, due to the film thickness being in the intermediate ferromagnetic region.

Most importantly, the investigations of the azimuthal angle dependence of XMCD have clearly shown the change of the magnetic easy axis from the $[110]$ direction of Fe in thin films to the $[100]$ direction with increasing thickness. The change of easy axis is observed at an Fe film thickness of 6.7 MLE and is attributed to the interface bonding of Fe-Ti orbitals and spin-orbit interactions. Other possible reasons behind the SRT are also discussed. The magnetic moments in the different directions follow a trend similar to the $[100]$ direction of Fe, however, the magnitude of magnetic moments as well as the ratio is found to be only around 70% of that in the $[100]$ direction. The effect of temperature on the XMCD reveal that the temperature dependency is weak for the Fe layers and the very small changes in magnetization are attributed to the magnetoelastic interactions due to the BaTiO_3 . The XMCD investigations for the induced moments at

the Ti *L* edges did not yield any signal possibly because the induced spin polarization on Ti 3*d* was too weak at room temperature.

In short, we observe that the magnetism of Fe ultrathin films on BaTiO₃(001) is correlated to the growth and structural order which in turn is correlated to the surface structure of BaTiO₃(001).

5 Fabrication and magnetism of ordered Fe islands on BaTiO₃(001)

The magnetic properties of thin films are highly sensitive to the microstructure and the morphology. Hence any change to the morphology or grain size will affect the magnetic properties. In order to understand the structural and magnetic property changes accompanying the annealing process, Auger electron spectroscopy, LEED, MOKE, XAS and XMCD measurements have been performed in-situ along with ex-situ SEM imaging and EDX spectroscopy investigations. Starting with a brief introduction in Section 5.1, the morphological transformations of the Fe thin films on annealing will be demonstrated in Section 5.2. The XAS measurements to investigate the interface stability will be described in Section 5.3. The MOKE and XMCD measurements will be discussed in the following Section 5.4. Finally the main conclusions drawn from this chapter are presented in Section 5.5.

5.1 Introduction

Nanostructures of Fe find applications in catalysis and magnetic recording which has triggered research on the modification of magnetic properties through morphological changes [110, 111]. In this context, the knowledge of the shape, size distribution and wetting properties of the metal overlayers are very important.

Metal on oxide systems also find applications in electronics where the stability of the interface, oxidation/reduction reactions and the effect of heat treatment are important. The investigations of deposition, morphology and effect of heat treatment on metal-metal oxide systems have been reported. For example, Ni on TiO₂ forms crystallite islands upon annealing [112]. In this case, although the interface orientation has been checked and found to be (110)Ni||(110)TiO₂, $[\bar{1}10]$ Ni||[001]TiO₂ which is the same before and after annealing [112], the stability of the interface has not been investigated. As already discussed in chapter 4, the stability of Fe/BaTiO₃ interface has been controversial as suggested by different reports [49, 50] and the XAS measurements shown in chapter 4 confirm that the interface is indeed sharp. In this regard, the interface stability of Fe thin films upon annealing turns out to be an interesting point of investigation.

Another important aspect for technological applications of metal-oxide systems is the ability to predict the size, topology and distribution of different features. For example, Fe nanoislands are employed in the fabrication of carbon nanotubes [110]. Hence

the knowledge of the shape and distribution of nanoislands is necessary to facilitate their use in these particular applications. In Fe nanowire arrays on W(110), the self assembly and magnetic domain microstructure have been studied [113] and the observations highlighted that by controlling the dewetting of the Fe film different magnetic anisotropy energies are influenced. This brings into light the importance of the interface as well as kinetic and thermodynamic processes involved in the self-assembly due to annealing. In order to achieve precise control over the desired features of the nanostructures, an understanding of the fundamental processes which govern their formation is necessary. In light of these reports, the studies of Fe island formation on BaTiO₃ and the exploration of their magnetic properties remain attractive.

Ordered arrays of metals on oxide substrates can be fabricated through a number of methods, for example, the self assembly through annealing was used to obtain arrays of Fe and the magnetic properties were also analysed for possible device applications [114]. Silly and Castell made use of self assembly to fabricate ordered islands of bcc Fe on SrTiO₃(001) (STO) [41]. However, the magnetic properties of such islands have not been investigated in detail so far. Ordered islands were obtained for the deposition of Fe on Mo(110) [115] and MgO(001) [116] substrates also. In all these cases, an understanding of the fundamental process is essential in effectively employing them for applications.

In this chapter, the formation of highly ordered directional nanoislands of Fe on BaTiO₃(001) through self organization due to annealing of the Fe film will be demonstrated along with the studies on the magnetic properties accompanying the transformation of morphology from thin film to nanoislands. The results will be discussed keeping in view the fundamental processes involved in morphology transformations.

5.2 Effect of annealing the Fe film: Morphological changes

Ultrathin films of Fe have been evaporated onto BaTiO₃(001) single crystal substrates from a metal e-beam evaporator at room temperature as discussed in chapter 3. Two thicknesses of Fe films (thin film-8 MLE, thick film-26 MLE) on BaTiO₃ have been investigated in order to understand the transformations in morphology with annealing. The films have been annealed in UHV to a series of temperatures above room temperature and morphological as well as magnetic properties were measured after cooling down to room temperature. The maximum annealing temperature (973 K) was kept below the Curie temperature of Fe (1043 K).

5.2.1 Auger electron spectroscopy

The effect of annealing on the surface composition and morphology has been investigated with Auger electron spectroscopy. The Auger electron spectra of an 8 MLE

Fe film recorded with 3 keV beam energy after annealing to different temperatures is shown in Fig. 5.1.

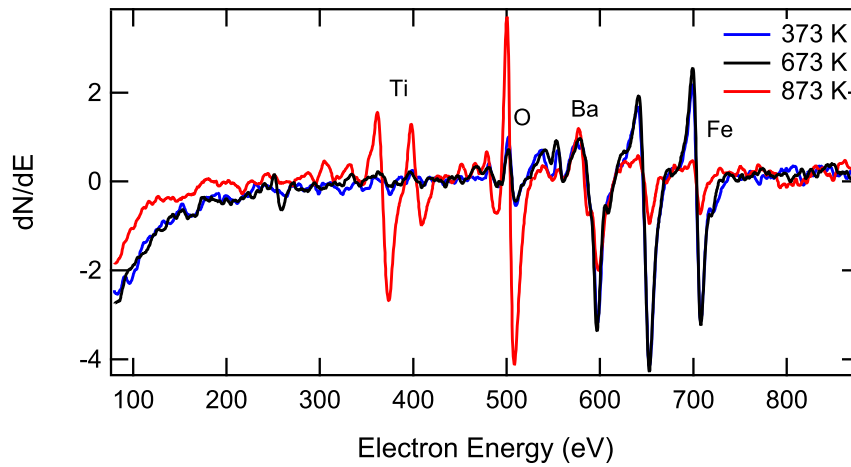


Figure 5.1: Auger electron spectra of an 8 MLE Fe film on BaTiO_3 annealed to different temperatures as mentioned in the figure legend. The spectra are recorded with 3 keV beam energy. The different features are labelled.

The different features of the spectra are labelled in Fig. 5.1 according to their kinetic energies with reference to the Handbook of Auger Electron Spectroscopy [117]. The peak at 375 eV corresponds to the principal Auger peak of Ti i.e. *LMM* Auger emission line of Ti, similarly the feature at 508 eV is the O *KLL* Auger emission line, the peak at 587 eV is Ba *MNN* Auger emission line and the three peaks at 597, 653 and 708 eV are Fe *LMM* Auger emission line features. The spectra obtained after 373 and 673 K annealing look almost similar with Fe features clearly visible. The absence of Ti, and Ba peaks indicate that the thickness of Fe exceeds the electron penetration depth for Ti, and Ba and hence with 8 MLE Fe, annealed to 373 K, Auger electron spectra hardly detects the substrate. The agreement in peak height measured at different points on the surface indicate uniform covering of the surface by the Fe layer. However, the spectra clearly show a reduction in Fe peak intensity after annealing to 873 K. The Ti, Ba and O peaks are more pronounced after the annealing, resulting in a change in the Fe-Ba and Fe-Ti peak ratios compared to the 673 K annealed film. This reduction in Fe indicates some morphological rearrangements within the film. After annealing, the peak ratio of O to Ti yields a value 2.7:1, which is less than the expected ratio of 3:1 from the chemical formula indicating the presence of a reduced BaTiO_3 surface. The 2.7:1 peak ratio is obtained taking into account the sensitivity factors from [117].

Similar to these measurements, the Auger electron spectroscopic measurements of a 4 MLE Fe film on MgO annealed to 673 K has also shown a reduction in the Fe peak intensity which was attributed to the formation of Fe islands [42]. Thus, it can be assumed that the decrease in peak ratio in Auger spectra results from the formation of Fe islands.

With the Auger spectroscopic investigations, a conclusion can be reached that the

change in the peak intensities due to annealing is caused by changes in the morphology. Any change in the surface morphology can be detected by microscopy methods which will be discussed in the coming sections.

5.2.2 Faceting: LEED investigations

During the growth of Fe layers on BaTiO₃, a LEED pattern is visible only from 6 MLE onwards. The as grown films revealed a LEED pattern with broad spots which is a sign of the presence of small islands of Fe which coalesce to a continuous film with subsequent evaporation.

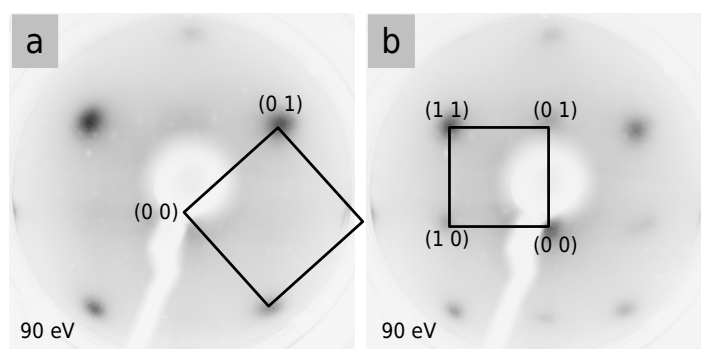


Figure 5.2: LEED images obtained from a 26 MLE Fe film on BaTiO₃ after (a) 573 K and (b) 673 K annealing. In the image, the gray scale is inverted, which means that black represents high electron intensity. The black square represents the unit cell of (a) Fe and (b) BaTiO₃ and the respective (0 0) and (1 0) spots are marked. The electron energies are given in figure.

The LEED images of the 8 MLE and 26 MLE Fe films annealed to 373 K are shown in chapter 4. The LEED spots are found to be broad indicating a limited long range periodic arrangement of scattering lattice points. After annealing to 473 K, the spots became sharper and the background intensity decreased, indicating enhanced long range order of the film. Figure 5.2 (a) shows the inverted grey scale LEED image of a thick Fe layer (26 MLE) annealed to 573 K, recorded at 90 eV kinetic electron energy. With 573 K annealing, the Fe spots became sharper. Figure 5.2 (b) displays the LEED pattern at a kinetic electron energy of 90 eV after annealing to 673 K. Here, the pattern resembles that of BaTiO₃ although the spots are broader than clean BaTiO₃. The broadening of the spots points to the disorder in the periodicity of BaTiO₃ lattice points. A comparison of the intensity of the (1 0) spots of BaTiO₃ and Fe film annealed to 673 K at 90 eV kinetic electron energy can be made. It is seen that for the BaTiO₃ substrate, the intensity of the (1 0) spot was high compared to (1 1). Whereas in Fig. 5.2 (b), the intensity of the (1 1) spot is found to be high. Hence we arrive at the observation that the (1 0) spot intensity of Fig. 5.2 (b) is reversed in comparison to that from the clean BaTiO₃. This is an indication that the (1 0) spot intensity from the Fe film has not completely disappeared, but is superimposed to the (1 1) spot of BaTiO₃.

After 873 K annealing, the LEED pattern completely changes to that of BaTiO₃ indicating a complete breakdown of the uniform Fe film which is indicated in the Auger

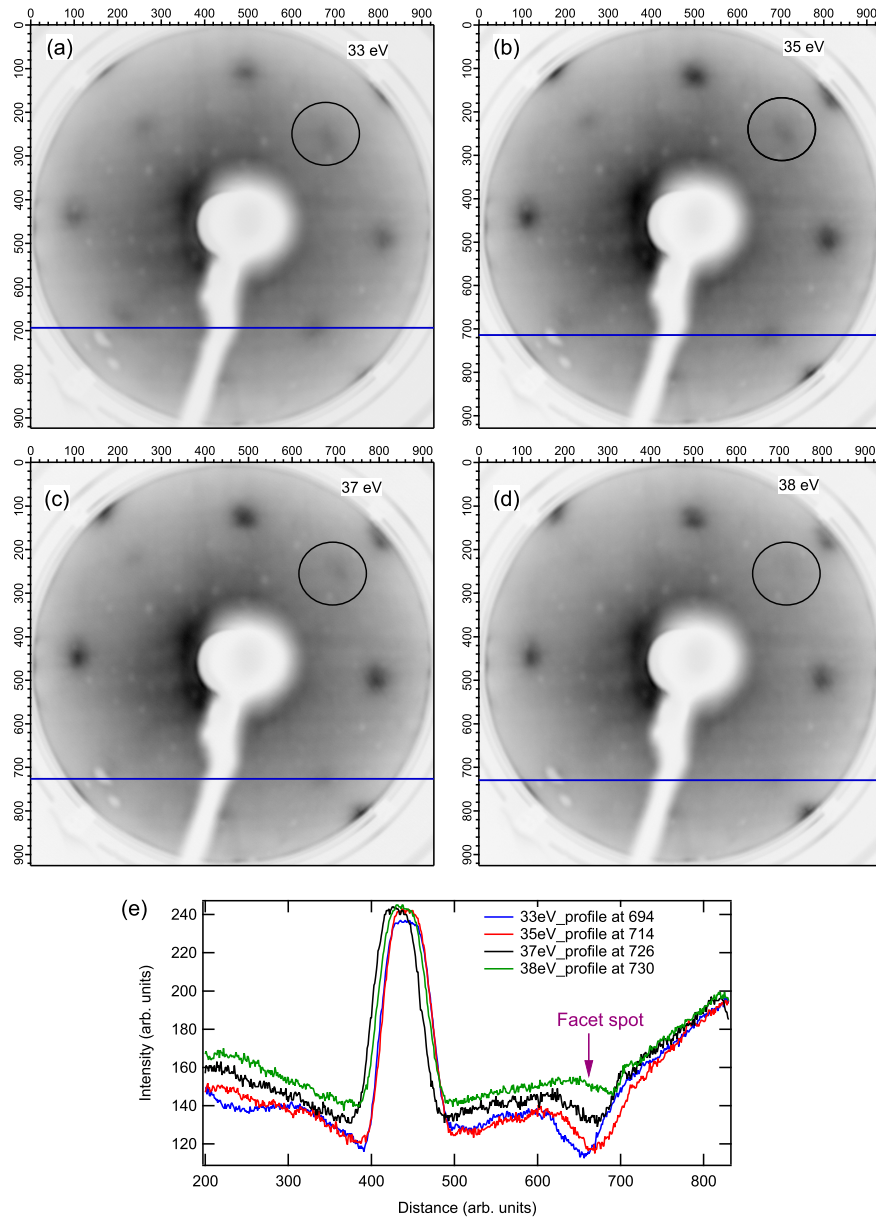


Figure 5.3: (a), (b), (c) and (d) LEED images obtained from an 8 MLE Fe film after 873 K annealing (e) Line profile made at facet spots from (a), (b), (c) and (d). The electron kinetic energies are indicated in figure.

electron spectra as a decrease in the intensity of Fe peaks. All LEED spots were found to have similar intensities and hence any distinction of Fe and BaTiO₃ contributions are impossible.

Figure 5.3 (a)-(d) shows the LEED images of an 8 MLE Fe film on BaTiO₃ recorded at 33, 35, 37 and 38 eV kinetic energies after annealing to 873 K. They show (1 0) spots of BaTiO₃ and (1 0) as well as (1 1) spots at higher energies. Some additional spots (marked in circles) which were different from the Fe(001) or BaTiO₃(001) spots are also seen. One additional spot in each quadrant, a total of four new spots are observed. The additional spots move away from the central (0 0) spot on increasing the kinetic energy while all other spots move towards the (0 0) spot of the original surface. Hence,

it can be understood that these new spots are the result of new surface orientations or facets in addition to the original (001). The new surfaces are formed due to some morphological rearrangements.

The term faceting denotes the formation of new crystal planes with lower energies which have different crystallographic orientations than the original ones due to the tendency of a crystal to lower the surface free energy [20]. LEED is profoundly useful in detecting the formation of facets with planes inclined to the nominal surface orientation. For a nominal surface orientation, using normal incidence of the primary beam of LEED, the (0 0) spot of the LEED pattern will be located at the centre of the diffraction screen. All other spots in the pattern move towards the (0 0) spot with an increase in kinetic electron energy. While with a faceted surface, the (0 0) beam from that facet will be located elsewhere on the screen or may be even out of the screen. Thus, the LEED spots from faceted surfaces move towards their (0 0) spot which is different from the nominal surface (0 0) spot. Hence, LEED is a very commonly referred technique in order to deduce faceting and resulting surface inclinations.

In order to clarify the presence and movement of the facet spot, a line profile is made across the LEED images. Figure 5.3 (e) shows the line profiles across one of the facet spot at 33, 35, 37 and 38 eV kinetic electron energies. The location of the profile of the facet spot is shown with the blue line in the LEED images and is also indicated in the figure legend. The presence of the facet spot is felt as a dip in the line profile. The intensity increase at 450 in the X-axis observed in Fig. 5.3 (e) is due to the bright area from the wehnelt assembly. The profiles clearly show the movement of facet spot away from the central (0 0) spot of the original film. The presence of four facet spots confirms the formation of four new surface inclinations compared to the original film. For a structurally similar system, Fe on SrTiO₃(001), the scanning tunnelling microscopic investigations provide evidence for the formation of four sided pyramidal bcc Fe nanoislands [41]. The pyramids have been shown to have a (001) top facet and four (011) side facets. Taking this into consideration, it can be assumed in the present case that upon annealing, the Fe thin film transforms to pyramidal structures with a (001) top surface and four (011) side facets. Hence, the four new LEED facet spots can be attributed to four new (011) surfaces.

Thus, the morphology change as seen from Auger electron spectroscopy is evidenced to be due to the faceting of the film through LEED investigations.

5.2.3 SEM and EDX spectroscopy investigations

Scanning electron microscopy (SEM) and electron dispersive X-ray spectroscopy (EDX) are well suited techniques to monitor the morphological changes in the Fe film. SEM images and EDX spectra have been recorded ex-situ after removing the sample from the UHV chamber.

The SEM images of the Fe films annealed to 373 K are shown in Fig. 5.4 (a). The

image shows a uniform contrast all over the film. It can be inferred that the film is continuous and any island-like structure is absent within the resolution of the image. The calculation of island size after deposition of a thick Fe layer is already discussed in chapter 4. But since the size calculated was close to 2.5 nm, it is impossible to resolve and image such structures with the help of the present resolution in SEM. Hence, we do not observe any small islands after 373 K annealing and the film surface appears to be flat. Since the area imaged is uniform, the image is recorded at a crack to distinguish the sample. The sample is broken and the edges of the sample are seen at the right hand bottom side of the image near the black coloured area. The black colour represents area outside the sample. It is clear from the image that the film is essentially uniform, continuous and structureless after 373 K annealing.

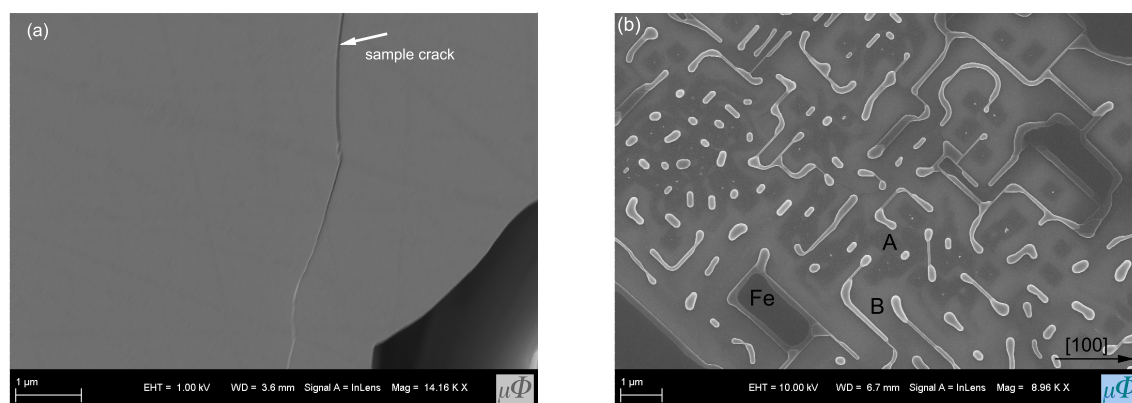


Figure 5.4: SEM images obtained from a 26 MLE Fe film on BaTiO₃ after annealing to temperatures (a) 373 K and (b) 773 K. The [100] direction is marked in (b) with respect to Fe.

Figure 5.4 (b) shows the SEM image of a 773 K annealed Fe film. The disruption of the film morphology due to annealing is clearly observed here. The prominent features in this image are elongated and interconnected islands. Some very small bright spots are also observed. Two different surroundings can be distinguished around the islands based on their grey levels, which are labelled as A and B in the image. Broad black coloured areas are also found.

To identify the different features in the image, the elemental composition of the constituents in the image has been determined using EDX. The results from the EDX analysis are shown in Fig. 5.5 and Fig. 5.6.

As seen in Fig. 5.6 (left), the elongated and interconnected islands are constituted by Fe. From this, the islands can be completely attributed to Fe with the BaTiO₃ signals coming from the substrate below. However, as shown in Fig. 5.6 (right), the uniform contrast area only contains Ba, Ti and O, with a stoichiometry expected for BaTiO₃, without any traces of Fe. Within experimental detection limits no difference between the compositions of the two grey levels A and B of Fig. 5.4 (b) could be found. However, taking into account the limited surface sensitivity of SEM, the possibility of one of the feature being BaTiO₃ and the other one being BaTiO₃ covered with a thin Fe wetting

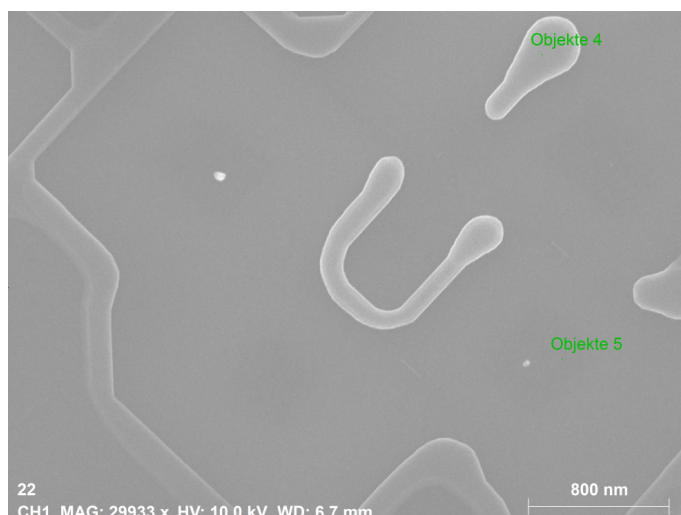


Figure 5.5: A SEM image of the 773 K annealed Fe film. The EDX spectra were recorded from a point in the island structure and from a point at the uniform contrast area.

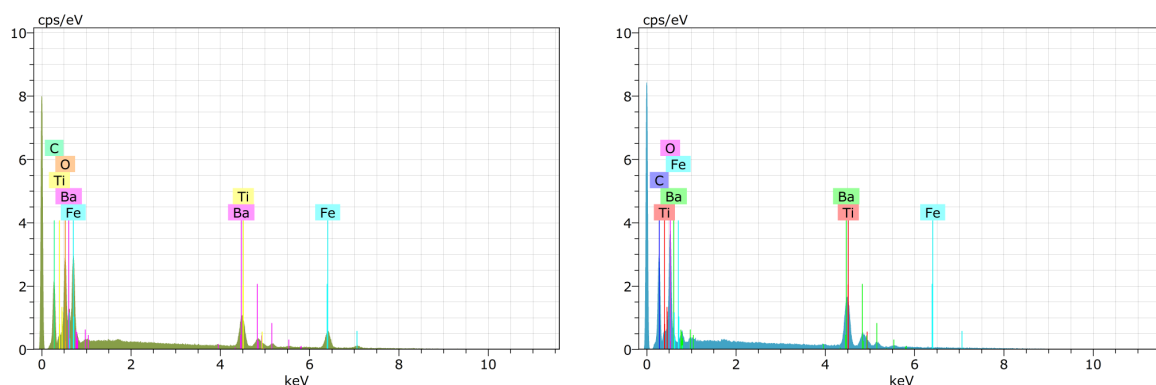


Figure 5.6: EDX spectra obtained from a 26 MLE Fe film on BaTiO₃ after annealing to 773 K. (left) spectrum from an island structure and (right) spectrum from the uniform area.

layer cannot be excluded. In this case, the image contrast could simply be due to the corresponding difference in work function. The broad black area was found to be constituted of Fe and hence is labelled Fe in Fig. 5.4 (b). A line profile across the image shows that the interconnected areas have a height difference to that of the islands with islands being higher.

Figure 5.7 (a) and (b) show the lower and higher resolution SEM images obtained after annealing the Fe film to 973 K. Compared to Fig. 5.4, the images clearly demonstrate the presence of highly ordered directional Fe islands. It is evident from the SEM images that after annealing to temperatures around 973 K, the film breaks up macroscopically and self assembles to form islands. The Fe islands are found to be of almost similar shape with preferential orientation, mostly along the [100] and the [110] directions of Fe. Although the islands are more uniform compared to the 773 K annealing, differences in shape and size still exist. The islands are found to possess an average diameter around 150 nm. This demonstrates that annealing at successively higher temperatures results in the formation of isolated islands at the cost of interconnected islands. Very

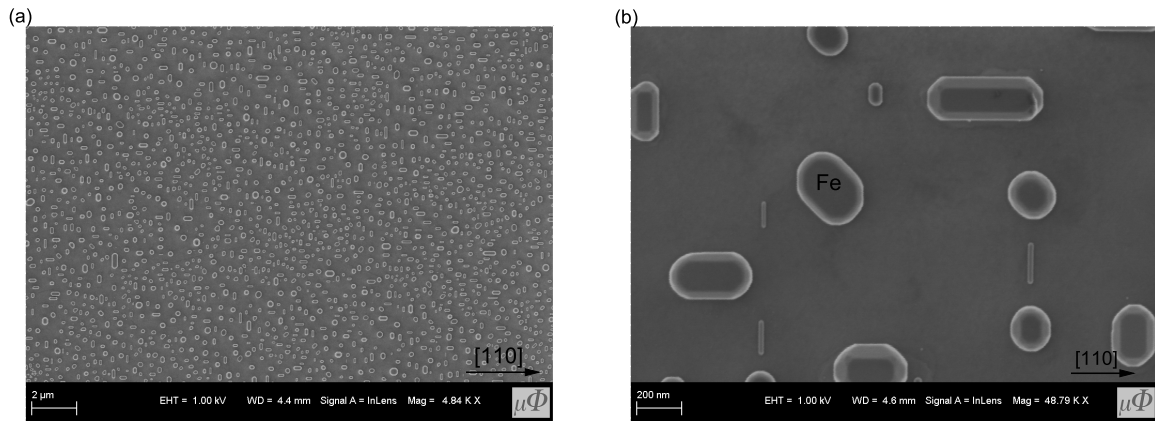


Figure 5.7: (a) low magnification and (b) high magnification SEM images obtained from a 26 MLE Fe film on BaTiO₃ after annealing to 973 K. The directions are specified in the images with respect to Fe.

small islands with sizes less than 30 nm are also found to be present. They appear as bright spots in the image. The large black areas composed of Fe are completely absent after annealing to 973 K. The contrast difference which existed in the island surroundings after 773 K annealing is also missing.

The EDX measurements done on these images reveal that the islands are constituted of Fe and the surrounding area is of BaTiO₃ alone. Hence, the 973 K annealing has resulted in the formation of uniform islands with uniform surroundings. Even in this case, the presence of a thin wetting Fe layer on top of the substrate cannot be excluded.

Thus, from the LEED and SEM investigations, it is clear that the film undergoes a major morphology change when heated above 673 K. This indicates that the film is metastable.

The growth of metal films on oxide substrates critically depends on the affinity of the metal to react with oxygen. Thermodynamic factors such as heat of formation (ΔH_f) have a strong influence on the stability of the metal-metal oxide interfaces. Metals having a high ΔH_f for oxide formation react strongly with the oxide substrate. One of the growth modes of thin metal films on oxides is the Frank-van der Merwe growth whereby a 2D layer-by-layer growth is obtained on top of a flat wetting layer produced upon deposition of the first layers due to the high affinity of a metal to oxide formation. The layer-by-layer growth is followed until a critical thickness beyond which the accumulated elastic strain in the film relaxes via the formation of dislocations. In the Stranski-Krastanow (S-K) growth mode, discrete 3D islands are formed at lower film thickness resulting from the lowering of strain. In the third growth mode, known as the Volmer-Weber growth mode, the formation of a wetting layer is suppressed due to the weak metal-substrate interactions resulting in the agglomeration of the metal into 3D islands [118, 119].

A change in the morphology of the Fe thin film upon annealing indicates that the rate limiting step in this morphology change has a high activation energy. The rate limiting

step could be the one involving the “climbing up/down” of Fe across a step edge from one terrace to another one and this barrier is known as the Ehrlich-Schwoebel barrier [26]. Because of the fewer nearest neighbors the atom possesses in the transition state while crossing the step edge, this barrier is generally higher than the barrier for the surface diffusion on a terrace. Thermodynamically, Fe has a lower heat of formation of oxide compared to Ti and hence only less interaction is expected for Fe with the BaTiO₃ surface. This typically results in low barriers for surface diffusion. If the annealing temperature is sufficiently high to overcome the Ehrlich-Schwoebel barrier, the atoms can diffuse to different terraces. In this case, the islands are formed with a preference to low-index surfaces since they have low surface energies. Since the Fe lattice matches with the BaTiO₃ lattice, (mismatch is only 1.5%), the Fe islands can be expected to have a (001) plane at the interface which is in agreement with the LEED patterns observed.

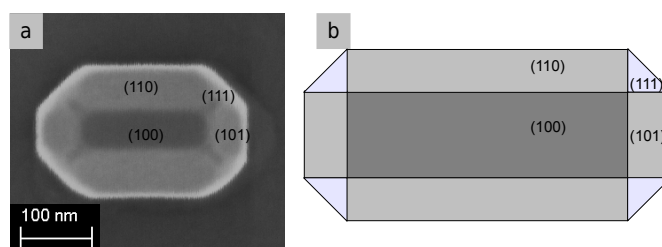


Figure 5.8: (a) SEM image of a representative Fe nanoisland formed after 973 K annealing. (b) A schematic for the possible island structure for the SEM image shown in (a).

The formation of ordered islands is the result of self assembly leading to faceting, favoured by thermodynamics and controlled by kinetic factors like nucleation and diffusion. The process of self assembly is driven by diffusion leading to a reduction in the surface energy of the system by the formation of low index surfaces. In order to minimize the total surface energy of the system, the planes with lower surface energies will be favored. The presence of (100) surface as expected from the LEED investigations is justified since even the formation of high energy planes would yield a lower energy compared to the flat film due to the reduction of surface area. Therefore, the island shape is not cubical with (100) surfaces, but pyramidal with (110) surfaces. For a bcc crystal, the surface energy (γ) of the (100) surface is larger than $\gamma(110)$ [120] and therefore the (110) orientation can be expected at the island edges.

The SEM image from a representative Fe island is shown in Fig. 5.8 (a). It is clear from the figure that the island has a square top surface and resembles an eight sided pyramid. An analysis of the image indicates that the islands cover only 7-8 % of the total area. In general, the islands can be imagined to be made of (100) planes at the top as pointed out by the LEED investigations. The surfaces at the edges have (110) orientation and (111) orientation at the corners. Based on this idea, the different surfaces of the nanoislands can be identified and assigned as shown in the schematic of Fig. 5.8(b).

Thus, the SEM investigations help to confirm the formation of island structures upon annealing the uniform Fe thin film. The EDX investigations help to identify the con-

stituent of the island structures as Fe.

5.3 Interface effects

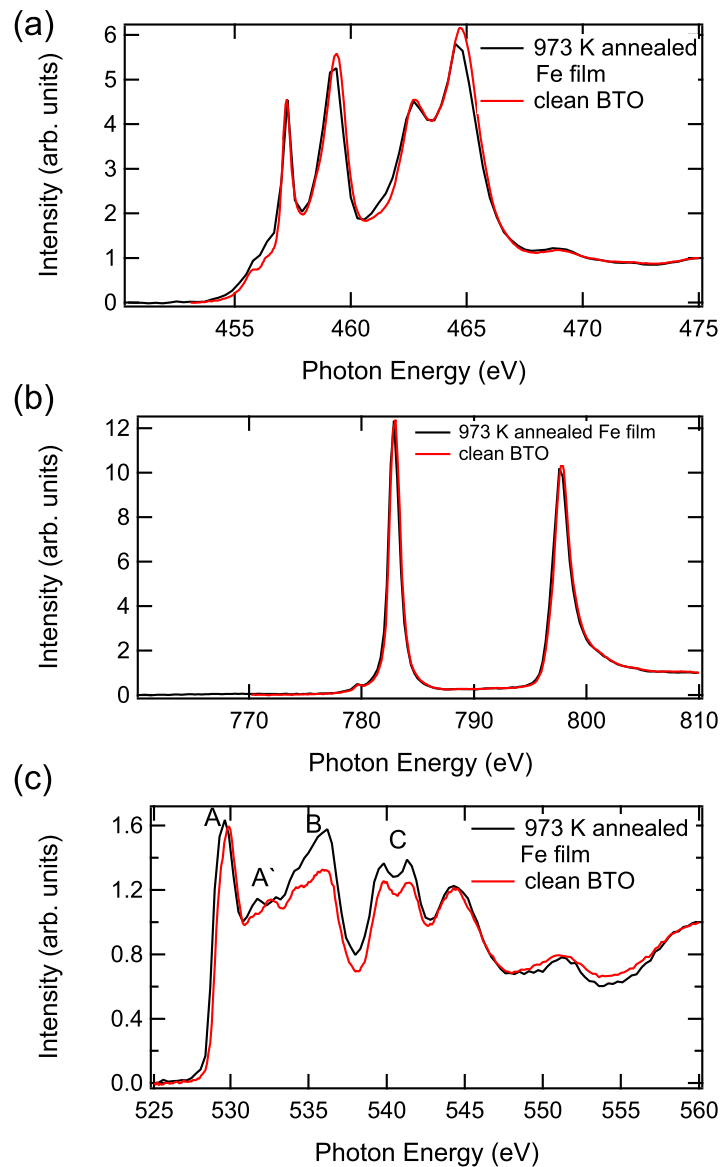


Figure 5.9: XA spectra measured at the (a) Ti $L_{2,3}$, (b) Ba $M_{4,5}$ and (c) O K edges from a 26 MLE Fe on BaTiO₃ annealed to 973 K using linear polarized light in grazing incidence with the sample at room temperature. For comparison, the corresponding spectra from clean BaTiO₃ are shown along with. All spectra are normalized to unity at the post edge region.

The changes to the interface of Fe and BaTiO₃ due to annealing have been examined with the help of XAS. The Fe $L_{2,3}$, Ti $L_{2,3}$, Ba $M_{4,5}$ and O K edges have been measured in total electron yield using linear polarized light in grazing incidence. All spectra are normalized at the post edge to unity.

Figure 5.9 (a) shows the Ti $L_{2,3}$ edges XA spectrum measured from the Fe film annealed to 973 K. For comparison, the Ti $L_{2,3}$ edges spectrum from a clean BaTiO₃ sub-

strate is shown along with. The line shapes of both spectra are equivalent. All spectral features of Ti $L_{2,3}$ from clean BaTiO₃ substrate are present in the spectrum from the annealed film. No additional features or splitting of peaks is noted in the Fe film spectrum. However, differences are observed in the intensity of pre-edge features and at a photon energy of 461 eV. A small shift (0.1 eV) towards lower energies is also present in the Fe film XA spectrum.

The XA spectrum at the Ba $M_{4,5}$ edges is shown in Fig. 5.9 (b) which also has similar features with a small energy shift (0.1 eV) compared to that of bulk BaTiO₃. The FWHM of the Ba $M_{4,5}$ edge peaks and the energy separation after annealing are found to be equivalent to that of BaTiO₃. Even with a high resolution, no differences in the XAS line shapes which could occur due to oxidation are observed.

The XA spectrum at the O K edge measured after annealing is shown in Fig. 5.9 (c). The spectrum shows similar features at similar energies to that of bulk BaTiO₃. However, differences in intensity ratios are noted in features A', B and C. In addition, similar to the Ti $L_{2,3}$ and Ba $M_{4,5}$ edges, a small energy shift (0.15 eV) towards lower energies is also present, which can be attributed as an experimental artefact caused by the data recording problems or a trouble from the beamline.

Hence, apart from the negligible changes observed as energy shift and intensity ratios, the absorption spectra from the annealed film more or less resemble the corresponding spectra from the clean BaTiO₃. Hence, it can be concluded that changes to the electronic structure of BaTiO₃ due to annealing is extremely small.

The absence of electronic changes at the interface can be explained energetically as discussed in chapter 4. In the first row transition metals, the reactivity decreases from left to right. Among Fe and Ti, the heat of formation of oxide is found to be higher for titanium compared to Fe. Due to this, the growth of Fe on TiO₂ will result in a very small interaction between Fe and the substrate. First row transition metals such as Cr and Cu reportedly have low interaction with Ti-oxide surfaces such as TiO₂ [121].

The absence of chemical changes at the interface of BaTiO₃ might also be contributed by the reduction of the BaTiO₃ substrate. The number of free oxygen at the interface might be too small to cause further noticeable reduction of the BaTiO₃ surface and oxidation of Fe.

5.4 Magnetic properties of Fe islands

The effect of annealing on the magnetic properties of the Fe layer and self assembled islands has been studied by means of MOKE and XMCD.

5.4.1 Magneto-Optic Kerr Effect

The magnetic properties have been probed by means of MOKE measurements in the longitudinal geometry. As shown in chapter 4, the XMCD measurements revealed the

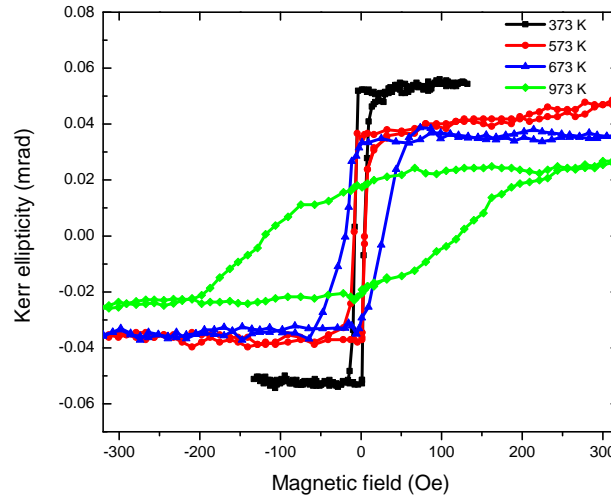


Figure 5.10: MOKE loops of a 26 MLE Fe film on BaTiO₃ measured in the longitudinal mode after annealing to different temperatures as indicated in the figure legend along the [100] direction of Fe. All MOKE loops were measured with the sample at room temperature.

in-plane (100) axis of Fe as the magnetic easy axis at 26 MLE thickness. The results of MOKE investigations after annealing to different temperatures are summarized in Fig. 5.10 which shows the in-plane longitudinal MOKE loops along the Fe (100) axis obtained after annealing to different temperatures as indicated. In order to show the changes more vividly, a selection of loops are shown in Fig. 5.10, based on the changes observed in coercivity and shape.

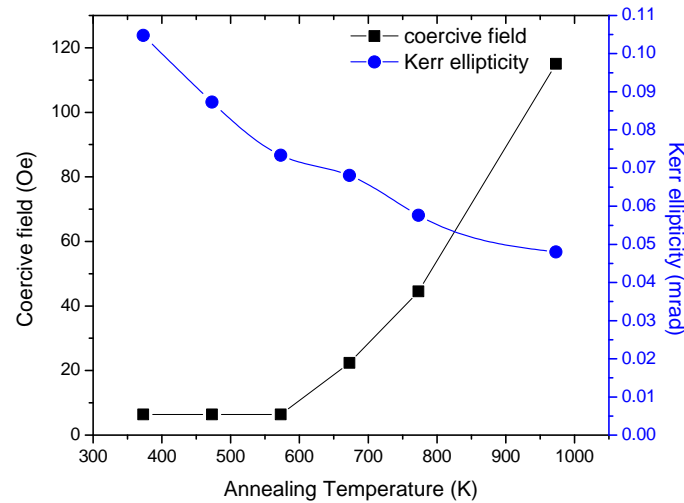


Figure 5.11: Variation of the coercive field and Kerr ellipticity as a function of annealing temperature for a 26 MLE Fe film on BaTiO₃ constructed from the MOKE loops. Spline curves are used to connect the points which serves as a guide to the eye.

For all MOKE loops, the remanent magnetization (M_r) is found to be close to the

saturation magnetization (M_s) implying that the magnetic easy axis direction is still parallel to the film plane and the different annealing steps did not change the easy axis of the film. For 373-573 K annealing, rectangular hysteresis loops with low coercivities (H_c) are obtained. The hysteresis loop obtained after 373 K annealing is a narrow loop with a width of 6.4 Oe. The rectangular shaped MOKE loops exhibiting small coercivity is an indication for a multidomain continuous film. The presence of defects and other structures would have an influence on the shape and hysteresis properties of the MOKE loops. The loops might become tilted due to the presence of defects which is not seen here. The coercivity (H_c) remains the same after annealing to 473 and 573 K.

Strong differences are observed when the annealing temperature is increased further. To be more precise, when the annealing temperature increases to 673 K, H_c is enhanced to 22 Oe. With further increment in annealing temperature, the loops become wider, and with 973 K annealing, the coercivity value reaches 115 Oe. Apart from the change in coercivity, there are evident changes in the shape of the loop and magnetization. The rectangular shaped hysteresis loops became more rounded at the corners after annealing to 673 K and above. But the loops were found to be saturated. With the increase in annealing temperature, the Kerr ellipticity, which is proportional to the magnetization, gradually decreases. Figure 5.11 summarizes the evolution of the coercive field as well as the magnetization as a function of annealing temperature. The Kerr ellipticity values shown in Fig. 5.11 are obtained by adding the magnitude of the maxima and minima values of Kerr ellipticity from individual measurements. This corresponds to the width of the MOKE loop. A decrease in the MOKE loop width is equivalent to a drop in the magnetization. Hence, the increase of coercivity and the decrease in magnetization are clearly demonstrated and the magnetization is reduced to nearly 50% of the value at 373 K after annealing to 973 K.

The change in the shape of the loop as well as coercivity and magnetization suggests changes in the film continuity or structure, as already seen from the SEM images. The changes in the magnetic properties exactly correspond to the temperatures which disrupt the film morphology. In the next section, the correlation of these changes to the magnetic moments of the film will be examined and the changes obtained from MOKE as well as XMCD measurements will be discussed.

5.4.2 X-ray Magnetic Circular Dichroism

In order to further understand the reduction in magnetization, the element specific magnetic properties have been investigated with XMCD since it offers the possibility to determine the spin and orbital magnetic moments. The absorption data have been obtained by measuring in total electron yield in grazing incidence at the [100] azimuthal direction of Fe. The experiments were performed at the BACH beamline, Elettra with the sample at room temperature.

The XAS and resultant XMCD spectra at the Fe $L_{2,3}$ edges taken after different tem-

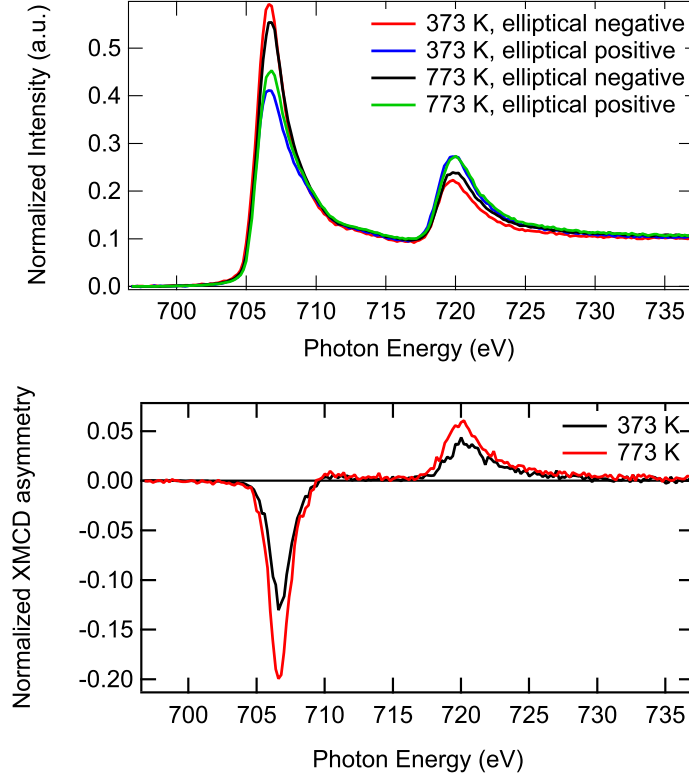


Figure 5.12: XAS and XMCD spectra at the Fe $L_{2,3}$ edges measured from a 26 MLE Fe film on BaTiO_3 after annealing to different temperatures as mentioned in the figure legend. The XAS spectra are normalized to the sum of the maximum at L_2 peak.

perature annealing steps are presented in Fig. 5.12. The line shape of normalized XAS and XMCD spectra correspond to metallic Fe without any additional features from chemical changes like oxidation. The Fe $L_{2,3}$ XAS line shape remains the same after 373 and 773 K annealing. The FWHM at the Fe L_3 edges in both cases is found to be 3 eV confirming that the annealing does not have pronounced effects on the Fe unoccupied levels.

The difference in normalized XMCD asymmetry with 773 K annealing compared to 373 K annealing is remarkable. The asymmetry after 773 K is only 60% of that of 373 K annealing. The magnetic moments were calculated from the XMCD spectra and are summarized in Tab. 5.1.

Table 5.1: Magnetic moments of Fe/ BaTiO_3 film for different temperatures measured in the [100] direction of Fe. The temperature is given in K and the asymmetry is given in % for the L_3 edge. m_S , m_I and m_{tot} are in units of μ_B/atom .

Temperature	asymmetry	m_S	m_I	m_I/m_S	m_{tot}
373	20	2.00	0.11	0.055	2.11
773	13	1.20	0.07	0.058	1.27
bulk Fe [5]		1.98	0.086	0.043	2.07

The m_S and m_{tot} values of the 26 MLE film are similar to those reported for bulk Fe [5]. However, the m_l as well as m_l/m_S values show a small increment. This might be due to the reduction in symmetry at the surface similar to that reported for Fe on GaAs [84]. Overall, the magnetic moments indicate that the 26 MLE film is comparable to bulk Fe in electronic and magnetic structure.

After annealing to 773 K, the m_S , m_l and m_{tot} values show a reduction of almost 40%. However, the m_l/m_S ratio remains constant indicating that the electronic structure changes are negligible before and after annealing.

Partial oxidation of the Fe film could result in a reduction of magnetic moments. And, a fully oxidized BaTiO₃ substrate can partially oxidize the thin Fe film at the interface. In the present case, neither the XAS nor AES spectral Fe signals show any signs of oxidation. This could be due to an already reduced substrate after surface preparations. Hence, it can be assumed that the surface preparation and the number of oxygen vacancies play a crucial role in the stability of the interface. This proves that a slightly reduced BaTiO₃ reacts less with Fe layers which would make it an excellent ferroelectric substrate to be used in combination with metallic ferromagnetic layers for multiferroic applications.

Another possible reason for the decrement in magnetization could be the structural transitions of the Fe film upon annealing. Annealing studies performed on 3 MLE thick Fe films on Cu(100) [122] reported a strong reduction in magnetisation which was attributed to a fct to fcc structural transition in Fe. However, this is less likely in the present case because the small lattice mismatch between Fe and BaTiO₃ implies the presence of bcc Fe, rather than fcc or fct Fe.

The evolution of magnetization, coercivity, magnetic moment and Auger electron peak intensity is the consequence of faceting and island formation of the Fe film as evident from LEED and SEM investigations. The change in coercivity indicates that the film begins to break up after 673 K annealing, the LEED images complement this assumption with the observation of a small change in pattern. The SEM images prove this, by showing large areas of BaTiO₃ along with interconnected long Fe islands as assessed with EDX.

From the SEM images the average particle size of the present Fe nanostructures has been determined as around 150 nm. This is more than the reported Fe particle superparamagnetic critical diameter of 20-30 nm for Fe [123]. Hence, the presence of superparamagnetic islands can be excluded as a reason for the decrease in magnetic moment. Also, the superparamagnetic particles require larger magnetic fields to reach saturation since the field has to overcome the thermal energy, kT . The MOKE measurements have shown fully saturated loops which negate the presence of superparamagnetic islands. The coercivity increase could be due to domain wall pinning after the creation of islands offering morphological barriers to domain wall motion.

Even though small, the lattice mismatch between Fe and BaTiO₃ is found to give rise to strain in the film [9, 52]. However, this strain is insufficient to induce such large

variations in magnetic properties since the nanoislands must have less strain compared to the film.

A comparison of the two thicknesses of Fe layers described (8 MLE and 26 MLE) yields the information that the initial film thickness is an important factor in determining the surface morphology as reported in [124]. In the present case, the thin Fe film indicates the formation of facets after annealing to a comparatively lower temperature (873 K) compared to the thick film which requires a higher annealing temperature (973 K) for the formation of islands.

For thin film systems, such as NiZn ferrites, a decrease of anisotropy resulted in a reduction of coercivity and an increase in magnetic moment [125]. Self assembly and formation of nanoislands is reported for Fe on Mo(110) grown through pulsed laser deposition at high temperatures around 723 K [115]. The studies of magnetic properties indicated that the island shape controls the anisotropy of the film and they observed zero remanence for islands with a width larger than 350 nm due to the non-uniform magnetic configuration in the island with either domains or vortices [115]. The configurational magnetic anisotropy which dominates over magnetocrystalline anisotropy for Fe nanoislands is reported to result in the rounding of hysteresis loops as observed for Fe on MgO [116]. Hence it is possible to ascribe the rounding of MOKE loops observed for high temperature annealing to a state where the magnetocrystalline anisotropy is dominated by the magnetic anisotropy due to the islands, or in other words, to the shape anisotropy of the nanoislands. Therefore, the decrease in magnetic moment could be caused by the competition between the different magnetic anisotropy contributions in the islands due to the [110] and the [100] orientations of islands. In this case we measure only the averaged projection of the magnetization of the islands, thereby causing a reduction in observed magnetic moment.

However, the strong reduction in magnetic moment and magnetization requires consideration of other factors such as the presence of magnetic structures like vortices, the size of which falls in the average particle size we observe [126]. A magnetic vortex is a spiral structure of magnetic moments. Such structures have already been reported on systems like Fe on W [126]. Hence, these magnetic structures can be imagined to be contributing to the decrease in magnetization as well as to the increase in coercivity.

A random orientation along with the distribution in size results in the distribution of switching fields which influences the shape of the loop as discussed for Fe on W [126]. The rounded loops in the present measurements can hence be correlated to a distribution in the size of particles even though they are highly oriented.

Thus, the MOKE measurements reveal a strong reduction in magnetization and enhancement in coercivity upon annealing to 973 K associated with the formation of ordered Fe nanoislands. The XMCD investigations also show a reduction in magnetic moments upon annealing to 773 K. These changes are discussed based on the assumption of the presence of special magnetic structures such as vortices.

5.5 Conclusions

In this chapter, the formation of the nanoislands of Fe on BaTiO₃ due to annealing and their magnetic properties are described. The thermal treatment induces directional nanoislands along the [100] and the [110] directions of Fe. The Auger electron spectra show a reduction in Fe peak intensity indicating the formation of islands which is confirmed by the LEED investigations where LEED spots from facets are obtained in addition to the original ones. Ex-situ SEM investigations reveal the morphology change from thin film to ordered islands as the annealing temperature increases. SEM images reveal the formation of ordered islands having a diameter 150 nm and the composition of the islands was determined as Fe with the help of EDX spectra. XAS investigations revealed that the formation of the BaTiO₃/Fe interface did not give rise to changes in the oxidation state of either Fe or BaTiO₃.

The magnetization process of the Fe thin film is found to be largely affected by the variation of annealing temperature. The magnetic properties measured as a function of annealing temperature reveal changes to coercivity, magnetization and magnetic moments. The MOKE measurements reveal an increase in coercivity of the film from 6.4 Oe to 115 Oe upon annealing to 973 K. The magnetic moment of the film is found to be similar to that of bulk after 373 K annealing and a reduction of nearly 40% is obtained upon annealing to 773 K. Upon annealing to 973 K, the magnetization exhibited a reduction to around 50% of the value after 373 K annealing. The reduction in the magnetic moment and the magnetization are attributed to the presence of magnetic structures such as vortices. In addition to the changes in magnitude, the shape of the MOKE loop became rounded which is correlated to a distribution in particle size.

The importance of initial film thickness and annealing temperature on the faceting of metal films on oxide substrates is demonstrated. This self assembly is explained on the basis of thermodynamic and kinetic considerations. Control over the desired morphology and properties can be achieved in the self assembly process by controlling the annealing temperature, duration of annealing and the initial film thickness. Therefore, such an approach can be made use of in designing novel ordered structures with metals on oxidic substrates. We strongly believe that the present work will motivate research on the morphology controlled growth of this multiferroic system.

6 Growth and magnetic properties of Fe ultrathin films on BaTiO₃ layers

Magnetoelectric coupling across multiferroic interfaces is appealing because of the well known ferroelectric control of magnetism [34]. Most of the studies on the magnetoelectric coupling in heterostructures have been reported for ferromagnetic layers on ferroelectric crystals. The need of high voltages for switching the polarization of the ferroelectric substrates is an obstacle in the commercial application of these materials. In this context, thin layers of ferroelectric materials such as BaTiO₃ will be beneficial since the voltages required for the reversal of polarization in these layers will be smaller than their thick counterparts.

Regarding the applications of ferroelectric thin films, Zhang and co-workers reported the control of magnetism of NiFe film on BaTiO₃ film with the application of a small voltage, around tens of volts [127]. It is also reported that the magnetization in Ni/BaTiO₃ hybrid structures can be irreversibly switched using the electric field dependence of the magnetic coercivity [12]. These experiments bring in the promise of future spintronic applications involving BaTiO₃ layers.

The magnetism of Fe on BaTiO₃ single crystal substrates is already discussed in chapter 4. This chapter begins with a brief introduction in section 6.1 followed by a detailed characterisation of BaTiO₃(100) layers on Pt(100) and SrTiO₃(100) substrates using XAS discussed in section 6.2. The changes at the interface due to the evaporation of Fe investigated using XAS will be described in section 6.3. The magnetic properties of Fe thin films grown on BaTiO₃(100)/Pt(100) will be elucidated in section 6.4 followed by the main conclusions of this chapter in section 6.5.

6.1 Introduction

Thin films of BaTiO₃(100) have certain advantages over single crystals when it comes to applications, especially in spintronics. Apart from comparatively lower voltages required for switching the polarization, the layer samples do not suffer from structural breakdown after passing through phase transitions a number of times.

Growth of thin films of ferroelectric materials has been picking up momentum lately. Considerable efforts have been made to fabricate and study the properties of BaTiO₃ thin films by means of various techniques. Different deposition techniques such as radio frequency sputtering, pulsed laser deposition, chemical vapor deposition, and

ultrasonic spraying technique have been employed in the preparation of BaTiO₃ layers as discussed in [128, 129, 24, 130]. Nano-crystalline BaTiO₃ films have been evaporated on Pt/Ti/SiO₂/Si substrates by RF magnetron sputtering at 773 K [131]. However, the change in the film stoichiometry compared to the source material and the creation of surface defects cannot be ruled out [132, 133]. Hence, the study of the films by means of any surface sensitive technique such as XAS is necessitated.

Pt and SrTiO₃ are found to be good substrates to grow BaTiO₃ films because of the lattice match. Förster and co-workers have prepared the BaTiO₃(100) layers on Pt(100) by means of sputter deposition [24]. Recently, Lee and co-workers have investigated the interfacial coupling in tricomponent superlattices like Fe/BaTiO₃(PbTiO₃)/Pt system using first principles [13]. They describe a polarization-induced change in the magnetization at the interface, which gives rise to a magnetoelectric coupling and makes the electric control of magnetism possible. This makes the Fe/BaTiO₃/Pt an attractive system for magnetic investigations. Brivio and co-workers reported the formation of BaTiO₃ layers via pulsed laser deposition (PLD) and also studied the growth and magnetism of Fe layers in the 1-3 nm thickness range using MOKE hysteresis loops [49]. Although they did not detect any sizable interdiffusion of cations and Fe, oxidation of interface Fe atoms is reported. However, as discussed in chapter 4, since the oxidation of Fe is ruled out in an Fe/BaTiO₃ single crystal interface, similar investigations on the BaTiO₃ layer substrates are important.

6.2 Characterization of BaTiO₃(100) layers

XAS is well suited to study the unoccupied electronic structure in oxide thin films due to the element specificity. Variations in the electronic structure of the BaTiO₃ layers which might occur due to the different preparation methods are studied by means of XAS.

The high resolution XA spectra measured at the Ti $L_{2,3}$, Ba $M_{4,5}$ and O K absorption edges of two different BaTiO₃(100) layer samples prepared by two different deposition techniques - pulsed laser deposition and magnetron sputtering are shown in Fig. 6.1. To enable an easy comparison, the spectra from bulk BaTiO₃ measured in the same geometry and discussed in chapter 4, are also shown along with. The spectra are recorded using linear polarized light in grazing incidence at room temperature in total electron yield mode and are normalized to the incident X-ray flux using the drain current from the last refocussing mirror in the beamline. Since the X-axis (photon energy) range was different for the different measurements, the Ti $L_{2,3}$ spectra in Fig. 6.1 (a) are normalized to unity at 470 eV, the Ba $M_{4,5}$ spectra in Fig. 6.1 (b) at 807 eV and O K spectra in Fig. 6.1 (c) at 550 eV. The spectra offer an energy resolution of 0.1 eV at the Ti $L_{2,3}$ edges and 0.2 eV at the O K edges, which helps to study the small features in more detail.

For brevity, the different features and the associated energies are summarized and compared to corresponding bulk BaTiO₃ values in Tab. 6.1, Tab. 6.2 and Tab. 6.3. The

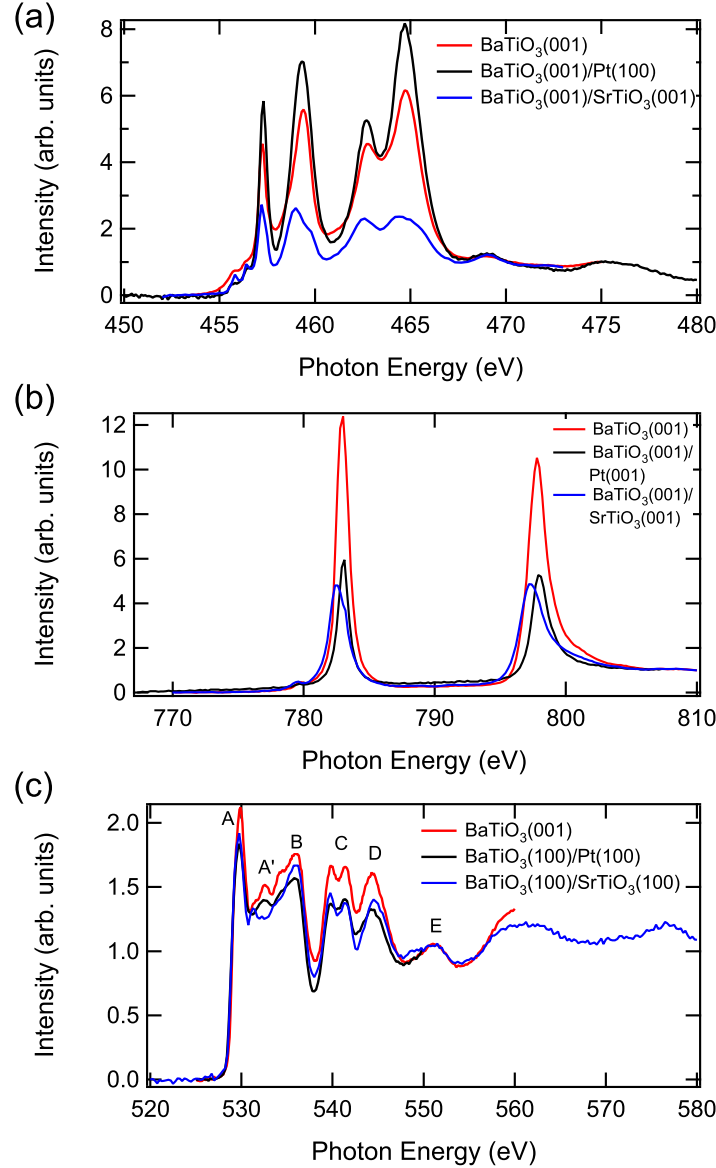


Figure 6.1: XA spectra of the (a) Ti $L_{2,3}$, (b) Ba $M_{4,5}$ and (c) O K edges of BaTiO₃ thin films on Pt(100) and SrTiO₃(100) compared to those from the BaTiO₃ single crystal substrates. The spectra are measured with linear polarized light in grazing incidence in the [001] direction of BaTiO₃ at room temperature in the TEY mode.

electronic transitions at the Ti $L_{2,3}$, Ba $M_{4,5}$ and O K edges are described in detail in chapter 4 for a BaTiO₃(001) single crystal.

Table 6.1: The different features and the associated energies at the Ti $L_{2,3}$ edges measured from BaTiO₃ layers using X-ray absorption in TEY mode compared to the corresponding energies of features obtained from a BaTiO₃(001) single crystal. The spectra are shown in Fig. 6.1.

Sample	Ti pre-edge	Ti L_3	Ti L_2
BaTiO ₃ (100)/Pt(100)	455.8, 456.4	457.30, 459.3	462.7, 464.7
BaTiO ₃ (100)/SrTiO ₃ (100)	455.8, 456.4	457.20, 459, 459.8	462.6, 464.6
BaTiO ₃ (001)	455.8, 456.4	457.25, 459.4	462.7, 464.7

Table 6.2: The features and the associated energies at the Ba $M_{4,5}$ edges from the XA spectra of BaTiO₃ layers shown in Fig. 6.1 compared to a BaTiO₃(001) single crystal absorption features.

Sample	Ba pre-edge	Ba M_5	Ba M_4
BaTiO ₃ (100)/Pt(100)	779.6	783.0	797.8
BaTiO ₃ (100)/SrTiO ₃ (100)	779.6	782.6	797.2
BaTiO ₃ (001)	779.8	783.0	797.8

Table 6.3: The features and the corresponding energies at the O K edge from the XA spectra of BaTiO₃ layers shown in Fig. 6.1 compared to a BaTiO₃(001) single crystal XAS.

Sample	O K edge (A)	O K edge (B)	O K edge (C)
BaTiO ₃ (100)/Pt(100)	529.8	535.8	539.8
BaTiO ₃ (100)/SrTiO ₃ (100)	529.75	535.75	539.75
BaTiO ₃ (001)	529.9	535.9	539.8

The pre-edge features at the Ti $L_{2,3}$ edges from both BaTiO₃ layers shown in Fig. 6.1 (a) and tabulated energies in Tab. 6.1 are consistent with the observations from the bulk BaTiO₃ sample. At the Ti L_3 edge, the BaTiO₃/Pt sample shows two peaks whereas a splitting of the lower energy peak is observed for the BaTiO₃(100)/SrTiO₃(100) sample. The Ti L_2 edge comprises of two features for both samples and the energies and the energy separation of the BaTiO₃(100)/Pt(100) sample match well with that of the BaTiO₃(100) sample. The BaTiO₃(100)/SrTiO₃(100) sample shows a small energy shift (0.1 eV) at the L_2 edge. Differences also exist in the intensity ratios of the different features for the two samples. As seen from Fig. 6.1, the normalized absorption intensity from the BaTiO₃(100)/Pt(100) is found to be higher than the other two samples. Similarly, the intensity of pre-edge features is found to be prominent in the BaTiO₃(100)/SrTiO₃(100) compared to other samples.

The corresponding transitions at the Ti $L_{2,3}$ edges are attributed to the Ti $3d$ band which is split into t_{2g} and e_g subbands according to the multiplet theory. Hence, any changes in the features indicate changes in the corresponding unoccupied electronic structure. This leads to the assumption that their preparation has caused deviations in the Ti environment which gets reflected in the spectral contributions.

The e_g states consist of d_{z^2} and $d_{x^2-y^2}$ orbitals and are usually directed towards ligand anions which makes them sensitive to changes from Ti octahedral symmetry [134]. De Groot and co-workers studied TiO₂ compounds and attributed the splitting/broadening of peaks to distortions in the octahedral symmetry around the Ti atom [135]. This would indicate that the distortion can be caused by the presence of oxygen vacancies around Ti resulting in a reduced state of Ti. However, Crocombette and co-workers argued that the existence of peak splitting in TiO₂ compounds cannot be ascribed to differences between the titanium oxides in the first coordination shell of the cation, instead they attributed it to the medium-range order effect originating from

at least-second-neighbor interactions [136]. By going with this analysis, the splitting can be understood as originating from the distortions around the Ti atom, either first or second nearest neighbors.

The Ba $M_{4,5}$ edges absorption spectra from the different samples are shown in Fig. 6.1 (b). The pre-edge feature at 779.8 eV in BaTiO₃(001) is seen to be slightly shifted to lower energies for both BaTiO₃(100)/Pt(100) and BaTiO₃(100)/SrTiO₃(100) samples. The $M_{4,5}$ features from BaTiO₃(100)/Pt(100) are similar to those of the BaTiO₃(001). However, the $M_{4,5}$ peaks from BaTiO₃(100)/SrTiO₃(100) are shifted to lower energies compared to the BaTiO₃(001) single crystal. The Ba L_3 edge shows additional peak splitting for the BaTiO₃(100)/SrTiO₃(100) sample. This indicates that even the Ba atom is affected by changes in Ti.

At the O K edge, presented in Fig. 6.1 (c), the different contributions are labelled from A to E in accordance with the calculated XA spectrum from [64] to enable an easy comparison. All main features from BaTiO₃(001) are reproduced in BaTiO₃(100)/Pt(100) and BaTiO₃(100)/SrTiO₃(100). The different features observed at the O K edge are the result of transitions from O 1s core levels to unoccupied 2p states which are also hybridized with the 3d and 4sp bands of Ti. Figure 6.1 (c) reveals differences in the energy region between features A and B. Particularly for BaTiO₃(100)/SrTiO₃(100), the feature A' is shifted to lower energies. However, the energy separation between all other features is consistent with BaTiO₃(001). The region from A to B in BaTiO₃(100)/Pt(100) sample matches well with that of the BaTiO₃(001) sample, except for a small energy shift (0.1 eV), indicating that the surface oxygen composition and configuration are very similar to the BaTiO₃(001). The highest absorption intensity is observed for BaTiO₃(001) and the lowest is found for BaTiO₃(100)/Pt(100). From a comparison to bulk BaTiO₃ spectra, the BaTiO₃(100)/Pt(100) appears to be only slightly reduced.

The spectral modifications in the energy region between features A and B can be explained using the concept of orbital hybridisation as interpreted for Pb_{0.5}Ca_{0.5}TiO₃ and Pb_{1-x}La_xTiO₃ compounds [137, 138]. The presence of a reduced Ti could lead to a similar effect for the BaTiO₃ layers investigated resulting in the reduction of hybridisation between O 2p and Ti 3d and 4sp levels.

The lattice mismatch for the BaTiO₃ layers is different for SrTiO₃(100) (2.2%) and Pt(100) (1.8%). This lattice mismatch is calculated by considering the lattice parameters as: $a_{\text{SrTiO}_3(100)} = 3.905 \text{ \AA}$ and $a_{\text{Pt}(100)} = 3.92 \text{ \AA}$ and $a_{\text{BaTiO}_3(100)} = 3.991 \text{ \AA}$. Hence, the strain due to the lattice mismatch can be thought of as another reason for the observed spectral changes. Lattice mismatch and the resultant compressive and expansive strain between the layer and the underlying substrate might lead to a tetragonal distortion of Ti octahedral symmetry. This in turn would lift the degeneracy of the d_{z^2} and $d_{x^2-y^2}$ orbitals. However, the difference in strain might be very small and hence if observed, the spectral changes must also be small.

Hence, from XAS investigations, more agreement is found between the BaTiO₃(100)/Pt(100) layers and BaTiO₃(001) electronic structure. The lattice mismatch

is also smaller in the BaTiO₃(100)/Pt(100) layers than the BaTiO₃(100)/SrTiO₃(100) layers and makes them well suited for further measurements.

6.3 Investigation of interface stability

The changes at the Fe/BaTiO₃(100)/Pt(100) interface, after Fe evaporation have been investigated by means of XAS. Figure 6.2 shows the normalized XA spectra at the Ti $L_{2,3}$, Ba $M_{4,5}$, O K and Fe $L_{2,3}$ edges measured in the TEY mode with linear polarized light in grazing incidence.

Figure 6.2 (a) shows the Ti $L_{2,3}$ edges absorption spectrum measured from a 7 MLE Fe/BaTiO₃/Pt compared to the BaTiO₃ and the BaTiO₃/Pt absorption spectra. At the Ti $L_{2,3}$ edges of BaTiO₃/Pt, a small energy shift (0.1 eV) of the L_2 and L_3 features is observed. However, all features, including the pre-edge peaks are present without any obvious splitting. These XA spectra indicate the absence of distortion on the titanium site. Even if the Ti is distorted, the extent is so small that the concerned changes are not discernible.

The Ba $M_{4,5}$ edges XA spectra are shown in Fig. 6.2 (b) after evaporating a 7 MLE Fe film. After evaporation of Fe, the peaks are similar to those of the BaTiO₃ and the BaTiO₃/Pt samples. All features including the pre-edge feature are present. In addition, no splitting of peaks or shift in energy is noted.

The O K edge XA spectra are presented in Fig. 6.2 (c). The intensity of peaks in the O K edge absorption spectrum goes down exponentially with an increase in Fe thickness. Hence, the O K edge spectra shown in Fig. 6.2 (c) are measured after evaporating 1 MLE of Fe. Modifications are observed especially in features A, A', B and C. This points to the changes in orbital hybridisations such as $O\ 2p \rightarrow Ti\ 3d, 4sp$ although no major changes to the Ti site are visible in Fig. 6.2 (a).

In order to study the electronic and the magnetic properties from a broad range of thickness, the Fe $L_{2,3}$ edges XA spectra have been measured from the Fe thin films of thickness ranging from 1 MLE to 18 MLE. Starting from 1 MLE, the Fe $L_{2,3}$ XAS revealed typical features of metallic Fe with L_2 and L_3 edge peaks at all thicknesses. The FWHM at the Fe L_3 edge is found to be 3.2 eV which is in agreement with the values obtained from the Fe layers on the BaTiO₃ single crystal substrates. The XA spectrum of a 7 MLE Fe film on BaTiO₃/Pt measured using linear polarized light is presented in Fig. 6.2 (d). The absence of splitting of peaks or shift in energies indicate the absence of oxidation in the Fe films at the interface contrary to that reported for Fe films on BaTiO₃/SrTiO₃ [49].

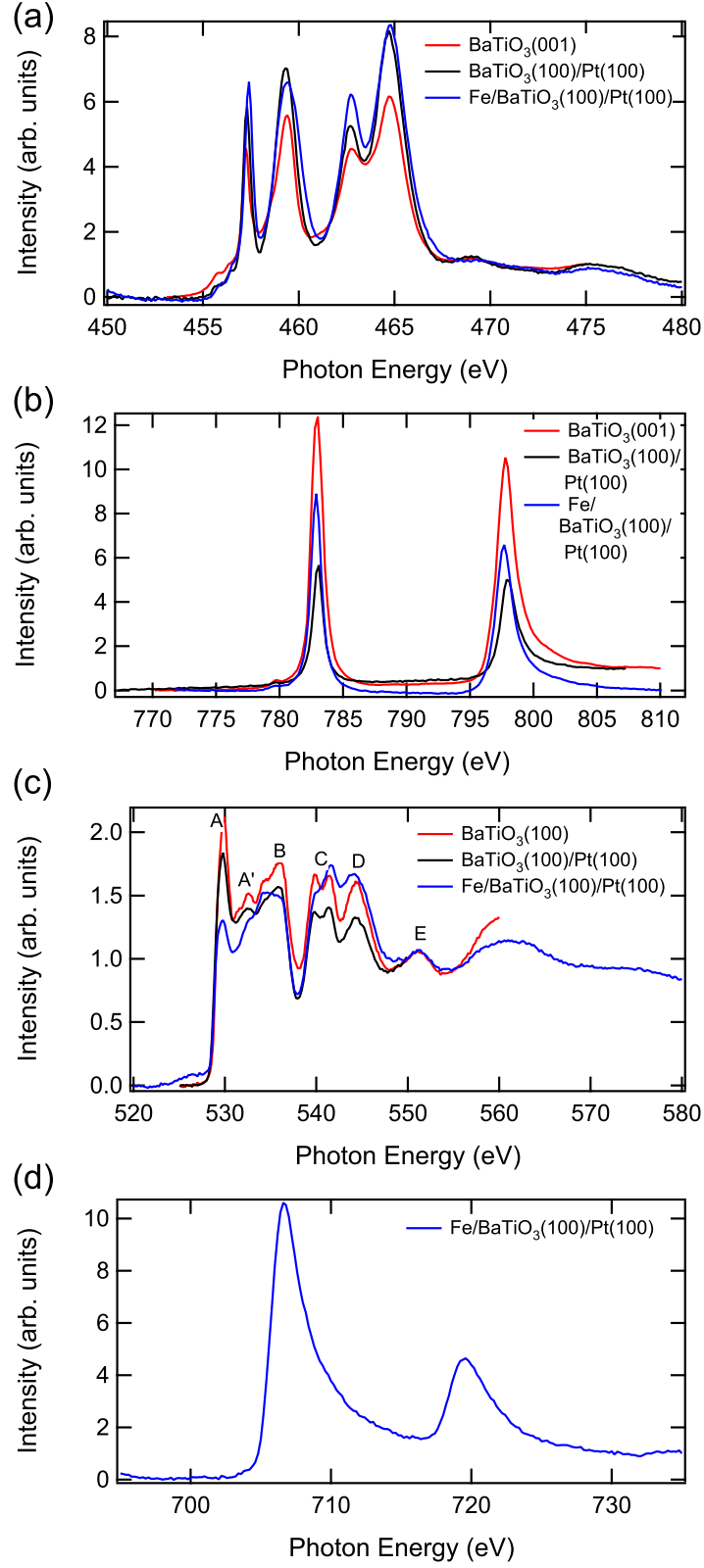


Figure 6.2: The XA spectra measured at the Ti $L_{2,3}$, Ba $M_{4,5}$, O K and Fe $L_{2,3}$ edges after evaporation of Fe layers on BaTiO_3/Pt . The spectra are measured at room temperature in the TEY mode using linear polarized light in grazing incidence. They are compared to the corresponding edge spectra from BaTiO_3 and BaTiO_3/Pt .

In particular, the XA spectrum at the Fe $L_{2,3}$ edges indicates the absence of oxidation. Hence, the presence of a sharp interface (starting from 1 MLE Fe) is confirmed. The non-mixing at the interface can be interpreted with the consideration of thermodynamic factors such as heat of formation of metal oxide being lower for Fe compared to Ti and Ba, as explained already in chapter 4. The slightly reduced BaTiO₃ layers might also lower the possibility of oxidizing the Fe further since the amount of free oxygen at the layer surface might be too small to cause further changes in the Fe oxidation state.

6.4 Magnetic properties of Fe films on BaTiO₃(100)/Pt(100)

The focus of this section is the intriguing magnetic properties of the Fe films on the BaTiO₃(100)/Pt(100) examined after evaporating uniform thin films and wedge film samples of Fe. The deposition of Fe wedge film and uniform film are described in chapter 3. And the correspondence of wedge data to that of a continuous film is already established in chapter 4. The evaporation has been done at room temperature and the film was later annealed to 373 K for 10 min. The Fe films have been characterised by means of Auger electron spectroscopy and XAS. The magnetic properties have been investigated with XMCD spectroscopy. All measurements have been done with the sample at room temperature.

6.4.1 Thickness dependence

The thickness dependence of the magnetic properties has been studied using a wedge-shaped Fe film. Figure 6.3 (a) shows the normalized Fe $L_{2,3}$ edges absorption spectra and the corresponding XMCD (in Fig. 6.3 (b)) of an 8 MLE Fe film on BaTiO₃ layers measured in the [110] direction of Fe. Similar to the XAS spectra, the XMCD line shapes from all Fe thicknesses are identical, overlap with each other and show no spectral features due to oxidation. The Fe films show an in-plane magnetic anisotropy for all thicknesses investigated. The XMCD spectra did not show any peaks until a thickness of 5.5 MLE indicating the absence of ferromagnetism below 5.5 MLE. This corresponds to the non-ferromagnetic region as observed in the case of Fe layers on BaTiO₃. The reason for the absence of magnetism is not well studied in this case. However, it can be attributed to the formation of either superparamagnetic islands or small islands where the long range order is absent owing to the similarities to the Fe film on a BaTiO₃ single crystal substrate. Ferromagnetism sets in at a point where the coalesced island size exceeds the critical length required for ferromagnetism.

The Fe $L_{2,3}$ edges XMCD spectra measured from the Fe films are shown in Fig. 6.4 (a). The signal to noise ratio is found to improve with increasing thickness. The XMCD spectra obtained from all thicknesses show bulklike features with a negative peak at the L_3 edge and a positive peak at the L_2 edge. The splitting of the L_3 peak observed

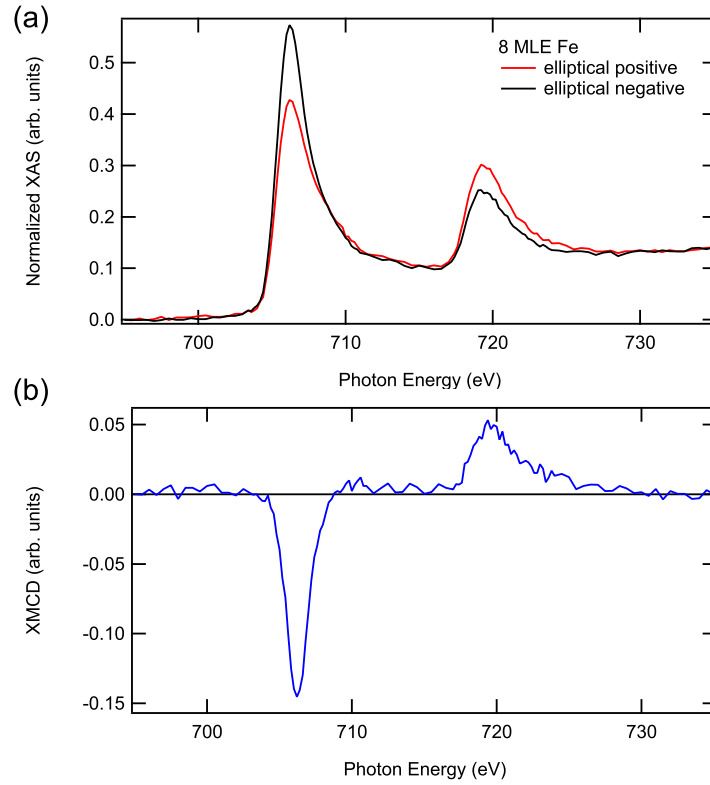


Figure 6.3: Normalized (a) XAS and (b) XMCD spectra measured at the Fe $L_{2,3}$ edges of an 8 MLE Fe film on BaTiO₃(100)/Pt(100) in the [100] direction of BaTiO₃(100).

for the thin layers (5.5 and 6 MLE) stems from a lower signal to noise ratio compared to thick layers. As the thickness of the Fe layers increase, the peak intensities also increase. A very small positive feature is observed at 710.2 eV. This feature has been observed for the Fe layers on BaTiO₃ single crystal substrates and has been discussed in chapter 4. The clear cascading behavior of the XMCD peak intensities points to the evolution of ferromagnetism as the film thickness increases.

In order to clearly understand the effect of thickness on the magnetic properties, the variation of the normalized XMCD asymmetry obtained from the XMCD spectra is plotted in Fig. 6.4 (b) as a function of the Fe film thickness. After the ferromagnetic onset at 5.5 MLE, the XMCD peak intensity increases steadily upto a thickness of about 8 MLE. This corresponds to an intermediate region where the magnitude of the XMCD is less than that of bulk. With further increase in Fe thickness, the XMCD intensity reaches saturation, in other words, bulk Fe-like values. In this region, the XMCD intensity stays constant with further increase in thickness.

Hence, similar to Fe films on BaTiO₃, the ferromagnetism evolves through two phases, namely, a non-magnetic phase below 5.5 MLE and a ferromagnetic phase (consisting of an intermediate region and fully saturated region) afterwards. The intermediate region corresponds to the region of asymmetry increase due to the coalition of islands. At the saturation thickness, the islands are large enough to pertain a long range order. The intermediate region where the magnetism increases as the thickness

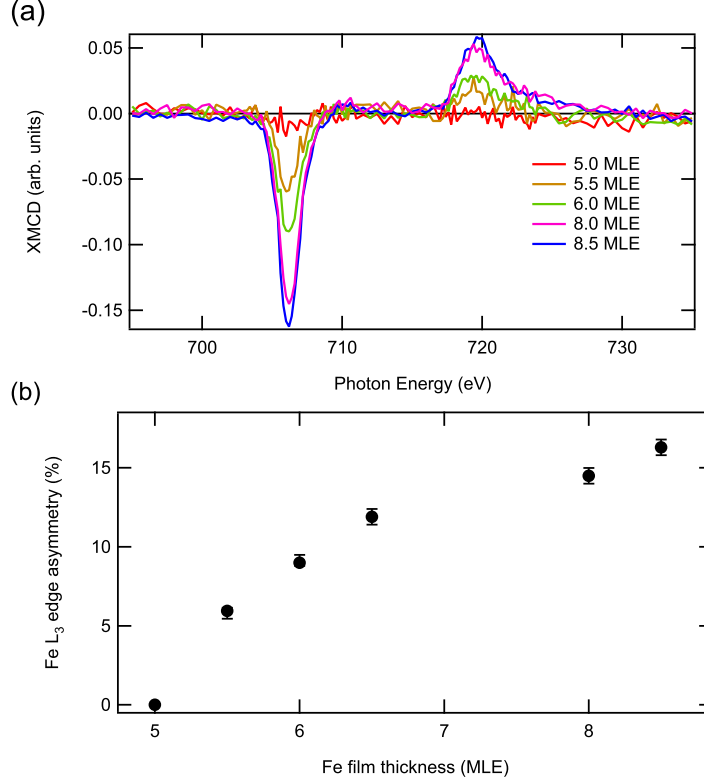


Figure 6.4: The normalized (a) XMCD spectra and (b) Fe L_3 edge XMCD asymmetry values of Fe films on BaTiO₃/Pt studied as a function of film thickness. The asymmetry values are obtained by normalizing the L_3 edge maxima to unity as described in the text. The error bars represent deviations obtained due to experimental errors and spectral analysis.

is increased, is found to be about 2.5 MLE wide. This is slightly wider than (wider by 0.5 MLE) the intermediate region for Fe thin films on BaTiO₃. This difference could result from a difference in growth and morphology of Fe on top of BaTiO₃ layers.

Absolute values of orbital moment (m_l), spin moment (m_s) and total magnetic moment (m_{Tot}) have been estimated by the application of sum rules [5] as discussed in chapter 2. Table 6.4 summarizes the values of the L_3 edge asymmetry, m_l , m_s , m_{Tot} and m_l/m_s obtained from the Fe $L_{2,3}$ XAS and XMCD spectra for different thicknesses of Fe.

Table 6.4: The magnetic moments (in Bohr magnetons) calculated from the $L_{2,3}$ XAS and XMCD spectra of Fe films on BaTiO₃/Pt in the [100] direction of BaTiO₃. (Values are given in units of $\mu_B/\text{atom.}$)

Thickness (MLE)	L_3 asymmetry (%)	m_s	m_l	m_l/m_s	m_{Tot}
6.0	9	0.84	0.09	0.107	0.93
8.5	16.3	1.65	0.12	0.075	1.77
Fe bulk [5]		1.98	0.086	0.043	2.07

From Tab. 6.4, the observed spin moment (m_s) for the thick Fe films is $1.65 \mu_B/\text{atom}$,

which is lower than that of bulk bcc Fe [5, 42]. However, the orbital moment (m_l) is $0.12 \mu_B/atom$ which shows an enhancement compared to the bulk value, $0.086 \mu_B/atom$. Due to the higher noise, the estimated moments have a maximum error of 20%. It is expected in thin film surfaces due to the reduced dimensionality and hence the symmetry breaking at the interface as described in reference [84]. The decrease in orbital moment with increase in thickness can be understood similar to that observed in the case of Fe clusters where the cluster-cluster interactions cause a decrease in orbital moment due to the increase in the average atomic coordination [87]. The spin moment is less affected by the cluster-cluster interactions. The magnetic moments obtained are found to be in agreement with the Fe/BaTiO₃ system as shown in chapter 4.

The orbital to spin moment ratio (m_l/m_s) is higher for all thin films investigated in comparison to the reported bulk Fe values. From Tab. 6.4, we can figure out the variation of m_l/m_s ratio which is closely associated with the change of electronic structure in thin films [42]. The ratio is larger for smaller thicknesses implying that as the coordination increases, the ratio decreases.

The m_{Tot} values of Fe shown in Tab. 6.4 are lower than the reported bulk Fe values [5, 42]. This decrement indicates the presence of a magnetic anisotropy in the thin films. More investigations of direction specific magnetic properties are described in the next section.

To conclude, the magnetic properties of the Fe films on BaTiO₃ layers resemble those on the single crystal BaTiO₃. This proves the point that the BaTiO₃ layers can be advantageously employed as a substitution instead of single crystals in multiferroic switching applications.

6.4.2 Azimuthal angle dependence

For Fe films on BaTiO₃, a spin reorientation transition (SRT) is described in chapter 4. In order to study the effect of the BaTiO₃ thickness on the SRT, the angle dependence of XMCD has been measured with Fe layers of two different thicknesses on BaTiO₃/Pt.

The normalized XA spectra at the Fe $L_{2,3}$ edges from the Fe films with 6.5 and 8.5 MLE thickness, acquired with two different azimuthal sample orientations relative to the photon propagation vector are shown in Fig. 6.5 (a), (b), (d) and (e). The resultant XMCD spectrum of a 6.5 MLE thick Fe film is shown in Fig. 6.5 (c) and that of an 8.5 MLE film is shown in Fig. 6.5 (f). The XAS and XMCD spectra do not show any change in line shape upon changing the azimuthal angle. However, the magnitude of the XMCD asymmetry varies in accordance to the changes in azimuthal angle.

For the thin film (6.5 MLE), the XMCD magnitude is higher in the Fe [110] orientation than in the [100], thereby indicating that the magnetization easy axis is closer to the [110]. Whereas for the thick film (8.5 MLE), the XMCD signal is more along the Fe [100] orientation, which is similar to bulk Fe behavior. The XMCD asymmetry

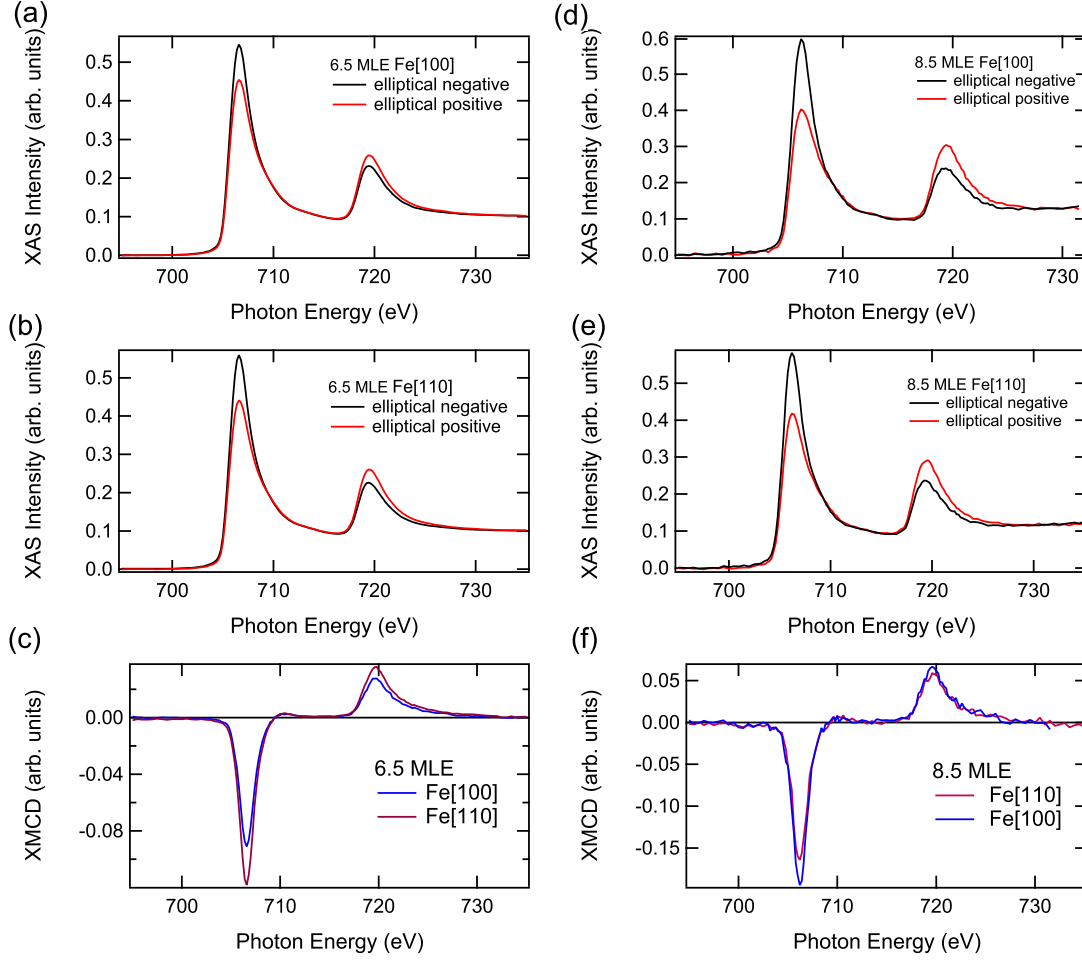


Figure 6.5: Normalized XAS and XMCD spectra measured at the Fe $L_{2,3}$ edges of 6.5 and 8.5 MLE Fe films on BaTiO₃(100)/Pt(100) acquired in different azimuthal angles with respect to the Fe[100] direction. The directions are specified in the figure legend.

along the [100] direction is found to be only 76% of that along the [110]. Thus, for thin films, an easy axis is observed along the Fe[110] direction which rotates in-plane to the [100] direction of Fe for thick films. Hence, an SRT within this thickness regime (6.5 to 8.5 MLE) is observed. The thickness at which the SRT occurs in the Fe films on BaTiO₃/Pt is very similar to that of the Fe film on BaTiO₃ substrate.

In order to verify the observations quantitatively, the orbital, spin and total magnetic moments have been calculated using sum rules. The calculated values of m_S , m_L , m_L/m_S and m_{Tot} for 6.5 and 8.5 MLE Fe films measured in the different azimuthal directions are summarized in Tab. 6.5 and Tab. 6.6.

From Tab. 6.5 and Tab. 6.6, it can be clearly seen that for the 6.5 MLE Fe film, the m_S , m_L and m_{Tot} values in the [110] direction of Fe are high compared to the [100] direction. The m_L/m_S ratio remains the same in both directions indicating the uniformity of the film in two directions and essentially a similar electronic structure in the film. Compared to bulk Fe values [5], the m_S and m_{Tot} values are found to be smaller. However, the orbital moment shows an enhancement in the [110] direction which could be

Table 6.5: The magnetic moments calculated from the Fe $L_{2,3}$ edges XAS and XMCD measured on a 6.5 MLE Fe/BaTiO₃/Pt in different directions. (Values are given in units of $\mu_B/\text{atom.}$)

Direction	L_3 asymmetry (%)	m_S	calculated m_l	corrected m_l	m_l/m_S	m_{Tot}
[110]	11.9	1.13	0.127	0.119	0.105	1.24
[100]	9.1	0.86	0.098	0.092	0.107	0.95

Table 6.6: The magnetic moments calculated from the Fe $L_{2,3}$ edges XAS and XMCD measured on an 8.5 MLE Fe/BaTiO₃/Pt in different directions. (Values are given in units of $\mu_B/\text{atom.}$)

Direction	L_3 asymmetry (%)	m_S	calculated m_l	corrected m_l	m_l/m_S	m_{Tot}
[110]	16.4	1.65	0.157	0.148	0.090	1.80
[100]	19.4	1.85	0.190	0.179	0.097	2.03

attributed to the contribution from the reduction of the coordination numbers at the surface [84]. The ratio is also higher than the reported bulk Fe values, however, comparable to some of the reported values for the Fe thin films as well as nanoclusters [5, 87, 88, 89].

In contrast to the 6.5 MLE film, the angular distribution of m_S , m_l and m_{Tot} values calculated for the 8.5 MLE Fe film, shows higher values in the [100] direction of Fe compared to the [110] direction. The m_l/m_S ratio of the 8.5 MLE film shows a small deviation in these directions. This deviation could be attributed to the uncertainties in measurements, and not to changes in the electronic structure. However, the m_l/m_S of the 8.5 MLE film is slightly smaller than that of the 6.5 MLE film. The m_S and m_{Tot} values calculated from the 8.5 MLE data in the [100] direction resemble the Fe bulk values with a very small reduction. An enhancement in the m_l values is found owing to the ultrathin limit of the film and the unquenched surface contribution to the total orbital moment [84].

A quantitative description for the reduction of magnetic moments along different directions is as follows. The magnetization along the easy axis is given by, $M_s \cos \phi$ [101], where ϕ is the angle between the applied field and magnetic easy axis. Thus for an easy axis along the [110] direction, the magnetization along the [100] is obtained by substituting 45° and in principle, along the [100], a reduction of 29% of the magnetization can be expected. This is closer to the 24% reduction observed for the 6.5 MLE Fe, when the easy axis is parallel to the [110] and the measurement direction is the [100]. The 11% reduction in the case of 8.5 MLE can be accounted by a scenario where the easy axis is not completely parallel to the [100], but has an angle from [100]. Very small differences in these values stem from the possible experimental differences in setting the angle.

The results of azimuthal angle dependent magnetic measurements can be qualita-

tively compared to that of other systems which exhibit a thickness dependent in-plane SRT, for instance, Fe/BaTiO₃(001) (discussed in chapter 4), Fe(110)/GaAs(110) and Fe(001)/MgO(001) [98, 99]. We arrive at the following assumptions: the BaTiO₃ thickness does not have much influence on the SRT since the thickness of SRT remains the same (within experimental errors) for BaTiO₃ single crystal substrate as well as layers. In comparison to the Fe/MgO system, which has a higher lattice mismatch, the SRT thickness is strikingly similar. Hence, we can conclude that the strain does not hold a key role in the SRT. The magnetic properties as well as the SRT observed in this system indicate a similar structure, growth and magnetism of Fe layers on BaTiO₃/Pt and single crystal BaTiO₃ substrates.

In general, the SRT is attributed to the surface anisotropy which originates due to interface Fe-Ti interactions and spin-orbit coupling, with an indication of spin-orbit coupling in the present system coming from the increased orbital moment values as well as m_l/m_s ratios. The m_l/m_s in the thin films is enhanced by almost 100% in comparison to the bulk Fe.

A small positive XMCD feature after the Fe L_3 edge has been experimentally realized in Ga_xFe_{1-x} and attributed to transitions from the $2p$ core level to the unoccupied majority spin band [93] which has also been supported by earlier theoretical studies [94, 95]. Arenholz and co-workers correlated the magnetoelastic energy to the electronic states located near the Fermi level [93]. Hence, in the present case, the small positive XMCD at 710.2 eV can be correlated to an unoccupied majority spin band. However, before and after the SRT, the feature does not change sign indicating absence of changes in the majority spin band. Therefore, the role of magnetoelastic energy as a main contribution for the SRT may be excluded with the help of the present measurements. This is in agreement with the earlier reports suggesting that magnetoelastic interactions do not play a key role in SRT [97].

The magnetic properties of Fe layers on BaTiO₃(100)/Pt(100) can also be compared to Fe layers on Pt(100) [139]. The structural and the magnetic investigations of the Fe layers on Pt(100) reveal the formation of a disordered alloy film due to the exchange of Fe atoms with the substrate Pt atoms. Remarkably, an SRT from the out-of-plane to in-plane direction is observed in 600 K annealed Fe films above a thickness of 5.2 MLE, which is attributed to the formation of Fe-Pt ordered alloys [139]. However, the XA spectra measured from the Fe/BaTiO₃(100)/Pt(100) do not suggest the formation of an Fe-Pt alloy and therefore this can be rejected as the reason for the SRT.

In short, with the angle dependent XMCD measurements of the Fe films on BaTiO₃ layers, an in-plane rotation of the magnetic easy axis from the [110] to the [100] direction is observed as the thickness of Fe increases. The measurements of anisotropy constants with MOKE or other similar experiments will help to understand the surface anisotropy contribution to the SRT due to a spin-orbit coupling and also to establish the reason of such transitions as anisotropy driven or dimensionality driven (due to the effect of the crystal field).

6.5 Conclusions

The BaTiO₃(100) layers on two different substrates, Pt(100) and SrTiO₃(100), have been characterized using X-ray absorption spectroscopy. The XA spectra measured at the Ti $L_{2,3}$, Ba $M_{4,5}$ and O K edges from the BaTiO₃(100) layers on Pt(100) agree well with the corresponding spectra from single crystals. For BaTiO₃(100) layers on SrTiO₃(100), a splitting of the spectral features is observed at the Ti $L_{2,3}$ and Ba $M_{4,5}$ edges as well as changes in the O K edge spectra indicating a difference in electronic structure compared to single crystal substrates. This is attributed to the tetragonal distortion around the Ti atom.

Fe films have been evaporated onto the BaTiO₃(100) layers on Pt(100) and the interface stability has been investigated with XAS. The interface is found to be sharp due to the absence of spectral changes. The magnetic properties of the Fe film on BaTiO₃(100)/Pt(100) have been studied using XMCD. The thickness and azimuthal angle dependence of XMCD are demonstrated. The Fe films did not show an out-of plane magnetism. The onset of in-plane ferromagnetism is observed at 5.5 MLE. Then the XMCD asymmetry gradually increases until around 8.5 MLE and reach saturation values thereafter. Magnetic moments calculated according to the sum rules reveal an enhancement in orbital moment compared to the bulk Fe. The spin moments of thick films are found to be similar to the Fe bulk values. The orbital to spin moment ratio values are in agreement to those reported for the Fe thin films on other substrates. The measurements on the azimuthal angle dependence revealed an in-plane spin reorientation transition as a function of film thickness. For thin layers, the Fe[110] direction is found to be the easy axis which changes to the [100] for thicker films. This SRT is attributed to the spin-orbit coupling driven magnetic anisotropy change at the interface. The experiments help to figure out that the major contribution to the SRT is not caused by magnetoelastic interactions. To conclude, the measurements described in this chapter demonstrates the magnetic properties of Fe films on BaTiO₃ layers and these properties are in agreement to those of Fe on BaTiO₃ single crystals. Hence, the BaTiO₃ layers can be effectively used as substitute for BaTiO₃ single crystals in polarization switching studies as well as multiferroic applications.

7 Growth and magnetic properties of ultrathin Fe_3O_4 films on $\text{BaTiO}_3(001)$

Fe_3O_4 is a mixed valence oxide (Fe^{2+} and Fe^{3+}) which exhibits interesting properties such as half metallicity, spin polarization and is widely used for a variety of applications like spintronics [140, 141].

This chapter discusses the characterisation and magnetic properties of Fe_3O_4 thin films on $\text{BaTiO}_3(001)$ deposited by means of reactive metal evaporation. The chapter begins with an introduction in section 7.1 followed by the XAS characterisation of the Fe_3O_4 thin films and the $\text{Fe}_3\text{O}_4/\text{BaTiO}_3(001)$ interface in section 7.2. The magnetic properties of the as prepared thin films will be elucidated in section 7.3 where the dependence of annealing temperature on the formation of Fe_3O_4 will be explained in subsection 7.3.1. The magnetic properties investigated as a function of azimuthal angle and the thickness of films are expressed in subsections 7.3.2 and 7.3.3 respectively. The XMLD measurements are described in 7.3.4 followed by conclusions drawn from this work presented in section 7.4.

7.1 Introduction

First principles calculations by Niranjana et al. [14] predict a magnetoelectric effect at the $\text{Fe}_3\text{O}_4/\text{BaTiO}_3$ interface, which stems from interface bonding. This prediction opens up the possibility of utilizing these materials for multifunctional device applications. The manipulation of such structures needs the understanding of the interface and the magnetic properties of this system since they have predicted the existence of two interface structures of Fe_3O_4 and calculated that the strength of the magnetoelectric coupling depends on the interface structure. In addition, the important influence of the surface and the interface on the magnetic properties of ultrathin films fuels the need for further investigations.

In a study of BaTiO_3 -Fe-oxide nanoparticles, Kim and co-workers employed XAS and XMCD experiments to investigate the interface electronic structure [48]. They found that the valence states of the Fe ions in the shells are in agreement with bulk. They also performed XMCD measurements at the Ti L edge and the results indicated that the induced spin polarization is negligibly weak at the interface.

Ultrathin Fe_3O_4 films are usually fabricated by post oxidation of Fe films [142, 143, 144]. However, the Fe_3O_4 films fabricated through post oxidation of Fe films suffer

from certain disadvantages. One of them is the coexistence of other Fe oxide phases such as FeO and Fe_2O_3 as discussed in [142]. The magnetic properties of the Fe_3O_4 film will change due to the coexistence of ferromagnetic Fe_2O_3 or antiferromagnetic FeO. Under these circumstances, growth of iron oxide films by reactive Fe evaporation where the metal is evaporated in an oxygen atmosphere and annealed in-situ is preferred. In this context, the characterisation of the as grown film, the interface as well as the investigation of the magnetic properties are essential to achieve control over desired properties.

The magnetic properties of the ultrathin films are sensitive to the growth conditions. The magnetic easy axis in Fe_3O_4 single crystal is reported to be along the [111] direction [145]. However, Lu and co-workers found that the Fe_3O_4 films on $\text{GaAs}(100)$ show an in-plane uniaxial anisotropy and the magnetic easy axis rotates from the $[1\bar{1}0]$ direction to the [001] direction with increasing film thickness [144]. Also, the Fe_3O_4 films grown on $\text{SrTiO}_3(001)$ were found to have a weak four fold anisotropy with the easy axis parallel to the [100] and the [010] directions [146]. Magnetic measurements on the Fe_3O_4 films on $\text{GaAs}(100)$ have indicated that the in-plane four fold anisotropy coexists with a uniaxial anisotropy [143].

Apart from the studies on BaTiO_3 -Fe oxide nanoparticles, the surface electronic structure, interface as well as the magnetic properties of the Fe_3O_4 ultrathin films (<4 nm thickness) on $\text{BaTiO}_3(001)$ substrates have not been well studied so far, although the magnetic properties of thick Fe_3O_4 films (80 nm) prepared by pulsed laser deposition have been investigated [147]. The role of interface oxygen has been emphasized in the study by Berdunov and co-workers [148] where they observed a magnetic contrast corresponding to the variations in the local surface states induced by oxygen vacancies and concluded that the spin-transport properties are altered due to the presence of surface defects. Especially, the predictions of a magnetoelectric effect [14] and a spin reorientation at the phase transitions of BaTiO_3 in $\text{Fe}_3\text{O}_4/\text{BaTiO}_3$ heterostructures discussed in terms of strain variations [149], point to the need of further detailed investigations. The understanding of the electronic as well as magnetic properties also helps in the studies of other isostructural substituted ferrites such as CoFe_2O_4 , MnFe_2O_4 and ZnFe_2O_4 .

7.2 Fe_3O_4 thin films on $\text{BaTiO}_3(001)$ studied with XAS

The Fe-oxide layers have been deposited on a clean BaTiO_3 substrate by reactive Fe deposition in an oxygen atmosphere. The formation of an Fe-oxide film on BaTiO_3 and the interface effects have been studied using XAS. The measurements have been taken with the sample at room temperature.

Figure 7.1 depicts the XA spectra at the Fe $L_{2,3}$ and O K edges of an Fe-oxide thin film measured using linear polarization of light. All spectra are normalized to an edge jump of unity. For the Fe $L_{2,3}$ spectrum, a singlet absorption peak at 708 eV and a

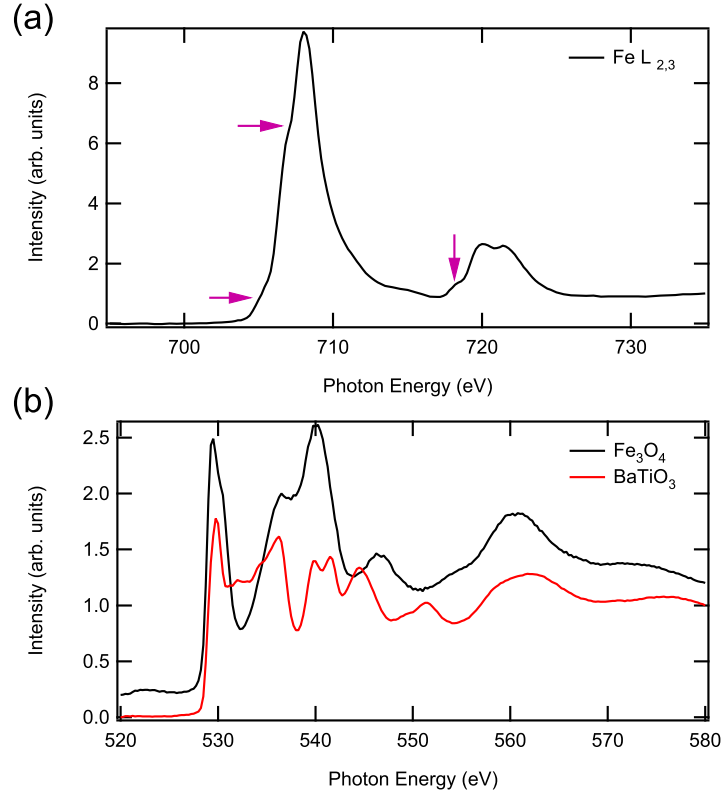


Figure 7.1: X-ray absorption spectra at the (a) Fe $L_{2,3}$ and (b) O K edges from an Fe₃O₄ film measured using linear polarization of light. For comparison, the O K edge spectrum from a BaTiO₃ single crystal is shown along with which is offset in the Y-axis for clarity. All spectra are normalized to an edge jump of 1. The characteristic shoulder features of Fe₃O₄ at the Fe $L_{2,3}$ edges are marked with arrows.

doublet with peaks at 720 and 721.4 eV constitute the L_3 and L_2 edges respectively. The characteristic shoulder like features of Fe₃O₄ are also observed at 704.6 and 706.8 eV and 718 eV. These features are marked in Fig. 7.1 (a) with arrows.

The XAS characterisation of the Fe $L_{2,3}$ edges in Fe oxides has been reported [152, 153]. The absorption spectra of Fe₃O₄ is found to be different from other Fe oxides such as Fe₂O₃. The absorption spectra of iron oxides- FeO, Fe₂O₃ and Fe₃O₄ are shown in Fig. 7.2 along with the XA spectra of metallic Fe which is published in [150, 151]. From Fig. 7.2, it is clear that the L_3 edge peak maxima of Fe₂O₃ and Fe₃O₄ are shifted in comparison to Fe and FeO [150, 151]. The general line shape and features of the spectra shown in Fig. 7.1 match well with those of Fe₃O₄ in Fig. 7.2 and to the Fe₃O₄ XAS published in [154, 145, 142] and differ considerably from other Fe oxides. Hence, the thin film can be unambiguously identified as Fe₃O₄.

According to [155], the characteristic electronic transitions resulting in the features at the Fe $L_{2,3}$ edges are as follows. Due to the presence of mixed valences i.e., Fe²⁺ and Fe³⁺, the electronic configuration of the Fe₃O₄ ground state has $3d^n$, $3d^{n+1}L_c^{-1}$ and $3d^{n+2}L_c^{-2}$ contributions ($n=5$ for Fe³⁺ and 6 for Fe²⁺, and L_c is the ligand core hole). In the final state, the electronic configuration is $2p^3d^{n+1}$ and $2p^3d^{n+2}L_c$. These final state configurations are specific to the features since a broad band feature is obtained as a

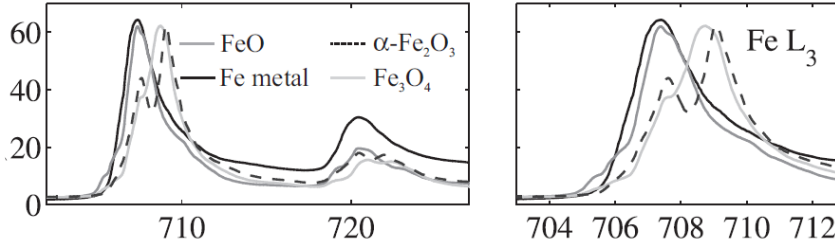


Figure 7.2: X-ray absorption spectra at the Fe $L_{2,3}$ edges from Fe and Fe oxides reported in [150, 151]. These figures are presented with permission from authors.

result of the $2p^3d^{n+2}L_c$ configuration and the $2p^3d^{n+1}$ configuration results in a multiplet structure [155]. In particular, the shoulders at the lower energies are attributed to transitions at Fe $^{2+}$ ions [153].

The BaTiO₃ single crystal O K edge spectrum is shown along with the Fe₃O₄ O K edge spectrum in Fig. 7.1 (b) to enable an easy comparison. The BaTiO₃ O K edge spectrum is offset in the intensity axis for clarity. The oxygen K edge absorption spectrum shows characteristic features of Fe₃O₄ with peaks at 529.5, 536.5, 540.25 eV, a shoulder at 530 eV and broad features at 546.5 and 560.5 eV. Well developed spectral features obtained in the thin film O K edge agree with the reports for Fe₃O₄ [142]. The clear presence of the shoulder at 530 eV can be utilized as a fingerprint in the confirmation of the stoichiometry as Fe₃O₄ compared to other compositions.

The absorption spectra at the Ti $L_{2,3}$ and Ba $M_{4,5}$ edges measured from a 2.4 nm Fe₃O₄ film are shown in Fig. 7.3 along with the corresponding spectra from a BaTiO₃ single crystal. A small shift of 0.2 eV is observed at the Ti L_3 edge between the spectra measured from the Fe₃O₄ film and the BaTiO₃ single crystal. However, all other features and associated energies of the Ti $L_{2,3}$ and Ba $L_{4,5}$ edges absorption spectra agree well with that of the single crystal indicating the absence of electronic changes at the interface. Hence, the above mentioned experiments rule out the possibility of a reduction of BaTiO₃, since it would change the oxidation state of Ti ion as +3 which will get reflected in the absorption spectra.

Hence, the analysis of the XA spectra leads to the conclusion that since all the multiplet features in the absorption spectrum result from the characteristic electronic structure of Fe₃O₄, the thin film is indeed Fe₃O₄ and the interface electronic structure of BaTiO₃ remains unaltered.

7.3 Magnetic properties of Fe₃O₄ films

The magnetic properties of the as prepared films have been investigated by means of room temperature XMCD and XMLD measurements.

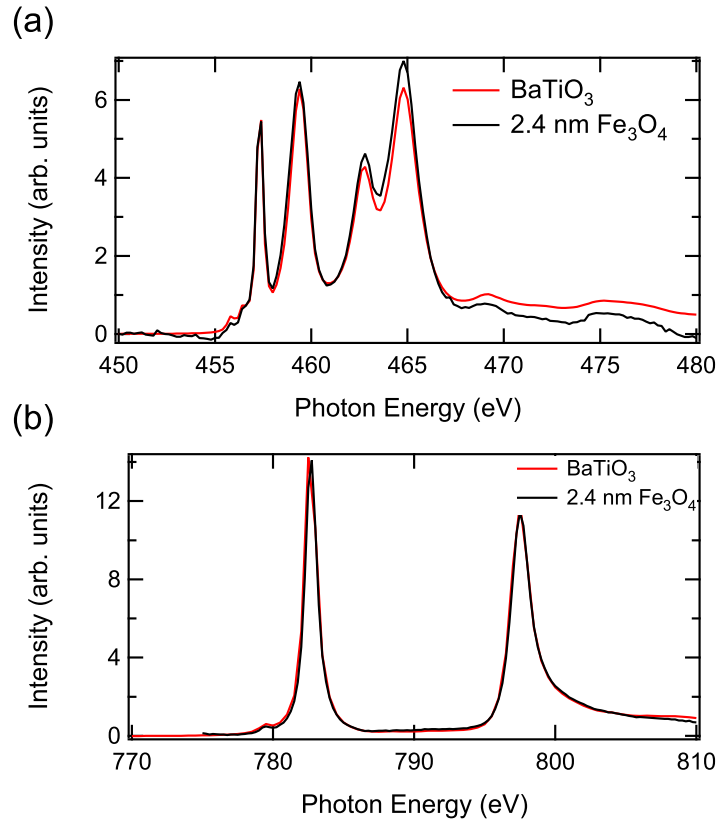


Figure 7.3: X-ray absorption spectra at the (a) Ti $L_{2,3}$ and (b) Ba $L_{4,5}$ edges measured from a 2.4 nm Fe_3O_4 film using linear polarization of light. For comparison, the Ti $L_{2,3}$ and Ba $L_{4,5}$ edges absorption spectra from a BaTiO_3 single crystal are shown along with. All measurements were performed with the sample at room temperature.

7.3.1 Effect of annealing and oxygen pressure

Annealing temperature and oxygen pressure play a significant role in the oxidation process of thin films. The dependence of the magnetic properties of Fe_3O_4 ultrathin films on the annealing and oxygen pressure have been studied by measuring the XAS and XMCD spectra of films evaporated at 573 K and post annealed to 673 K and 873 K. The oxygen pressure was kept constant at 1×10^{-6} mbar during evaporation and post annealing.

The evolution of the oxidation for a 3 nm thick Fe_3O_4 film as a function of annealing temperature is shown in Fig. 7.4. The XAS ((a) and (b)) and the XMCD ((c) and (d)) spectra measured from the film annealed to two different temperatures 673 and 873 K show typical multiplet features expected for the Fe_3O_4 . The different spectral features are discussed before and the XA spectra after both post annealing treatments show similar features.

The XMCD spectral features differ in their intensity ratios and peak heights for different oxidation stages as observed in Fig. 7.4. The L_2 edge intensity which is very low after the 673 K annealing, is found to increase upon annealing to 873 K. At the L_3 edge, clear differences are observed in the negative peaks. In the 673 K annealed film, the

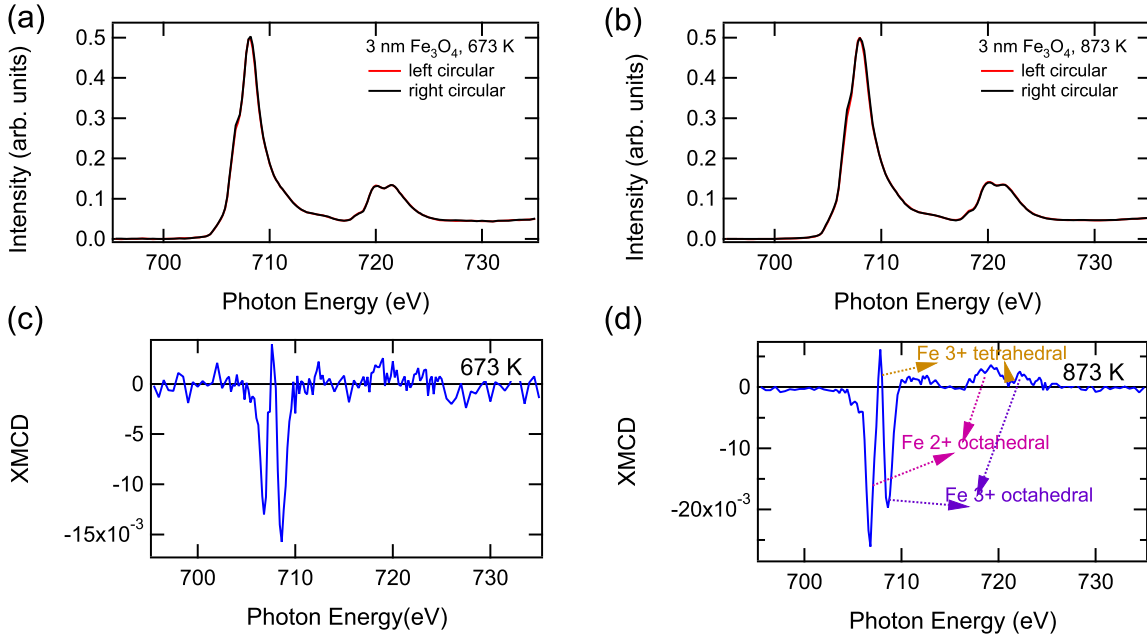


Figure 7.4: Effect of annealing on the magnetic properties of Fe_3O_4 films on BaTiO_3 depicted with XAS ((a) and (b)) and XMCD ((c) and (d)) spectra of films annealed to 673 K and 873 K respectively. The oxygen pressure was 1×10^{-6} mbar.

low energy L_3 edge negative feature is smaller compared to the higher energy L_3 edge negative feature, whereas after the 873 K annealing, this tendency reverses.

The XMCD at the $\text{Fe } L_{2,3}$ edges of Fe oxides has also been widely reported [154, 145, 156, 157, 144, 155]. The different contributions in the XMCD spectra can be understood in comparison to the reported theoretical and experimental spectra of Fe_3O_4 [154, 157], even though the assignment of XMCD spectral features is not free from controversies. According to the literature, the low energy negative peak at the L_3 edge and the low energy positive peak at the L_2 edge result from the contribution of Fe^{2+} in octahedral sites. The higher energy negative feature at the L_3 edge and the higher energy positive feature at the L_2 edge are attributed to Fe^{3+} spin up ions. The contributions from the Fe^{3+} spin down ions present in tetrahedral sites show up as a positive peak at the L_3 edge and a negative peak at the L_2 edge. The XMCD peaks are labelled in Fig. 7.4 (d) according to this assignment.

By assuming the above mentioned site occupancies, it can be seen that the contribution from Fe_{Oh}^{2+} increases in comparison to Fe_{Oh}^{3+} after higher temperature post annealing. The presence of more Fe^{2+} points to an imperfect oxidation. This in turn indicates the formation of a stoichiometrically comparable film to Fe_3O_4 after annealing to 873 K. From the evident differences of the site occupancies of our XMCD spectra, it is understood that the 673 K annealing is not sufficient to oxidize the film completely and further annealing to 873 K, helps in improving the stoichiometry. The changes in stoichiometry may be achieved by the improvement of the long range structural order in the film, since the structural order may have influences on the site occupancies of the Fe^{2+} and Fe^{3+} ions and any deviation from the perfect structural order is expected

to cause changes in the magnetic properties. A cation redistribution due to increased annealing temperature can be thought of as a reason for the better long range structural order. Thermodynamics driven cation redistribution, for example, has been obtained for CoFe_2O_4 by varying the cooling rate between 0.01 and 1000°C/s [158]. Valuable information regarding the stoichiometry of the film can also be obtained by calculating XMCD spectra by assuming different site occupancies as shown in [157].

Reports suggesting a fluctuating mixed valence state question the validity of the charge ordering as Fe^{2+} and Fe^{3+} [29, 30]. But, since the time of XMCD measurements is less than the hopping of Fe ions in two different sites [16], the XMCD peak assignment to Fe^{2+} and Fe^{3+} ions should be correct. However, considering state of the art interpretation of the XMCD spectra, our spectra after 873 K annealing match very well with those reported for Fe_3O_4 [48, 142, 155]. Even considering the small uncertainty in the estimation of different contributions, the agreement for both XAS and XMCD spectra is apparently so good over the entire energy range that the oxidation state after 873 K annealing can be obviously identified as Fe_3O_4 .

7.3.2 Magnetic anisotropy

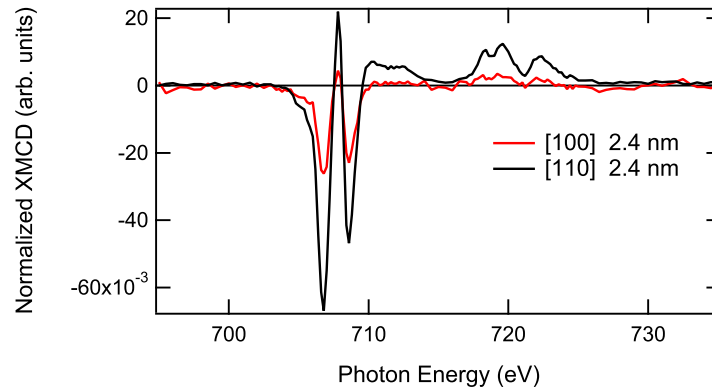


Figure 7.5: Anisotropy in the Fe $L_{2,3}$ XMCD for the Fe_3O_4 layers on $\text{BaTiO}_3(001)$. The measurement directions specified in the figure legend are with respect to BaTiO_3 .

The magnetic properties of the thin films are anisotropic i.e., the magnetization along a particular direction is preferred. To understand this effect in Fe_3O_4 films, the XMCD spectra have been measured in different azimuthal directions. Figure 7.5 illustrates the direction dependence of the XMCD in the Fe_3O_4 films grown on $\text{BaTiO}_3(001)$. It shows the normalized Fe $L_{2,3}$ edge XMCD of a 2.4 nm thick Fe_3O_4 film, measured in two different azimuthal directions, the [100] and the [110], with respect to BaTiO_3 .

From Fig. 7.5, it can be seen that the intensity of all Fe $L_{2,3}$ features along the [110] direction of BaTiO_3 is larger than along the [100] direction. The change in azimuthal direction does not give rise to new features. From an almost doubling of intensity along the [110] direction, it is evident that the preferred magnetization direction lies parallel to the [110] direction of BaTiO_3 .

It is expected that the growth of thin films can have a strong influence on the magnetic properties. The anisotropic XMLD of Fe₃O₄ on SrTiO₃(001) was studied by Arenholz and co-workers and they reported a weak four fold anisotropy with an easy axis parallel to the [100] and the [010] directions for the Fe₃O₄ thin films grown on SrTiO₃(001) [146]. The epitaxial relation for Fe₃O₄ on BaTiO₃(001) for a pulsed laser deposited thick film was found to be Fe₃O₄ [004] \parallel BaTiO₃[002] [147]. Hence if we assume an epitaxial relation of Fe₃O₄(001) \parallel BaTiO₃(001), we observe a deviation in the magnetic easy axis from that observed for Fe₃O₄ on SrTiO₃. One possible reason for this deviation could be the presence of a uniaxial anisotropy and the MOKE measurements in different directions might be helpful in this regard to confirm this. The presence of a uniaxial anisotropy is reported for the thin Fe₃O₄ layers on GaAs [143]. In the present case, the changes in the magnetic anisotropy of the Fe₃O₄ thin films might be induced by a strain from the BaTiO₃ substrate and the resultant magnetoelastic interactions.

Hence, the azimuthal angle dependent Fe $L_{2,3}$ edges XMCD spectra reveal a magnetic anisotropy in the thin Fe₃O₄ films. This magnetic anisotropy might be caused by a strain from the BaTiO₃ substrate. The presence of a uniaxial anisotropy also cannot be excluded.

7.3.3 Thickness dependence

In this section, the evolution of XMCD spectral features is studied as a function of film thickness. The Fe $L_{2,3}$ XMCD spectra of thin Fe₃O₄ films measured from a wedge shaped sample in the [100] direction of BaTiO₃ are presented in Fig. 7.6. For the whole range of film thickness investigated, the magnetisation is found to lie in the film plane. Perpendicular magnetisation is not observed for any thickness.

As evident from the normalized XMCD spectra shown in Fig. 7.6 (a), the XMCD intensity increases as a function of thickness within the thickness range of 1.4 to 2.9 nm. Moreover, this intensity enhancement is observed in the L_2 as well as L_3 edge features. Our investigations started from a 1.4 nm thick Fe₃O₄ film and the sample is found to be magnetic from thereon. Therefore, the presence of a nonmagnetic region below 1.4 nm (average thickness of 1.7 unit cells) and the formation of a thin nonmagnetic FeO layer at the interface cannot be excluded by our measurements. However, the small XMCD signal at 1.4 nm and its increase with thickness indicates the presence of a non-magnetic layer below 1.4 nm.

A careful analysis of spectral features indicates some changes in the intensity ratio of the XMCD peaks especially at the L_3 edge. To see the trend more clearly, the lower energy negative XMCD feature of all films are normalized to 1. These normalized spectra are presented in Fig. 7.6 (b). After this normalization procedure, evident differences are obtained in the peak intensities. Following the above mentioned XMCD feature assignment, this variation is closely related to differences in Fe²⁺ and Fe³⁺ site

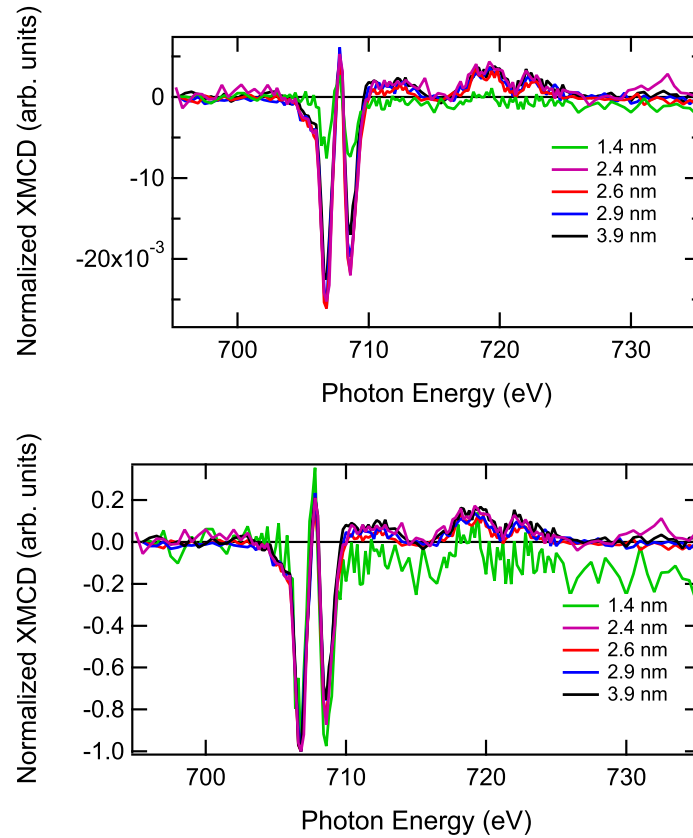


Figure 7.6: Normalized Fe $L_{2,3}$ XMCD spectra measured as a function of Fe_3O_4 film thickness. The measurements were taken from a wedge shaped $\text{Fe}_3\text{O}_4/\text{BaTiO}_3(001)$ film in the $[100]$ direction of BaTiO_3 . Film thickness is indicated in the figure legend.

occupancies. Ideally, since all measurements were taken from the same wedge shaped sample, equal site occupancies can be expected throughout the wedge at any thickness. However, this is not the case. The thin layer (1.4 nm) shows an almost 1:1 ratio of the L_3 edge negative peaks which decreases as the thickness increases. The peak ratios of the 2.4 and 2.6 nm films are found to be similar. The ratios of 2.9 and 3.9 nm films are also similar and agree with the published Fe_3O_4 XMCD data, but, they are lower than the other peak ratios. Hence, for the 1.4 nm film, assuming the site occupancies as discussed earlier, indicates the presence of more Fe^{3+} ions. This difference could stem from a higher oxidation of the film due to a longer time oxidation or a higher oxidation temperature. The presence of another iron oxide such as Fe_2O_3 at the surface can lead to an increase in Fe^{3+} ions. Hence, the annealing might have resulted in changes in the surface of the thin film which gets reflected in the XMCD spectra.

The increase in XMCD intensity even at a thickness of 3.9 nm of Fe_3O_4 which was the highest thickness investigated in the present study, hints that the film has not reached complete magnetic saturation. The magnetic field generated by the pulse coils is only 0.05 mT, which might not be sufficient to magnetically saturate these films because oxides usually require higher fields to reach saturation [159]. Any measurement to record a hysteresis loop like MOKE and SQUID would be helpful to know if this is the

case.

Information regarding the spin and the orbital magnetic moments of Fe₃O₄ can be extracted by applying XMCD sum rules. However, contradicting results are obtained for magnetic moments of Fe₃O₄ calculated using the sum rules in literature [145, 156]. Hence the validity of sum rules in a mixed valence system such as Fe₃O₄ remains an open question to date.

Although the extraction of magnetic moments doesn't seem to be straightforward, the magnetic moments from the XMCD spectra from Fig. 7.5 are calculated according to the conventional sum rules in the [110] direction from the thick film (since the thin film might also have other oxides and the spectra are noisy) and the results are tabulated in Tab. 7.1.

Table 7.1: The magnetic moments (in Bohr magnetons) per Fe atom calculated from the $L_{2,3}$ XAS and XMCD spectra of Fe₃O₄ layers on BaTiO₃ in the [110] direction of BaTiO₃. Film thickness is given in nm.

Thickness (nm)	m_S	m_l	m_l/m_S
2.4	0.47	0.048	0.10
2.9	0.46	0.11	0.24

Compared to the earlier reports of magnetic moments of 100 nm thick Fe₃O₄ on MgO and Al₂O₃ [160], the m_S and m_l/m_S values per Fe atom shown in Tab. 7.1 are smaller. A possible reason could be the deviation of the measurement direction from the magnetic easy axis. Moreover, the measurement thickness can still be in the intermediate saturation regime and might not have reached saturation magnetization thickness. This can contribute to the observed reduction in magnetic moments.

7.3.4 XMLD

The combination of XMCD and XMLD spectra serve as a good method to distinguish the stoichiometry of Fe oxides due to the different angular and magnetisation dependency of XMLD expected in different oxide systems [146]. The XMLD measurements have been taken for Fe₃O₄ film by magnetically saturating the film along the easy axis and by rotating the E-vector relative to the film (and the film relative to the E-vector).

The results of XMLD measurements performed on a 2.6 nm thick Fe₃O₄ film are presented in Fig. 7.7. The absorption spectra measured in the [100] direction of BaTiO₃ are shown in the top panel and the resultant XMLD spectrum in the bottom panel. The absorption spectra itself clearly demonstrate differences between the features while measuring with linear vertical and horizontal light, especially in the lower energy shoulders at the L_3 edge. Linear vertical and horizontal light correspond to two perpendicular directions within the surface plane. A comparison of XMLD and XMCD

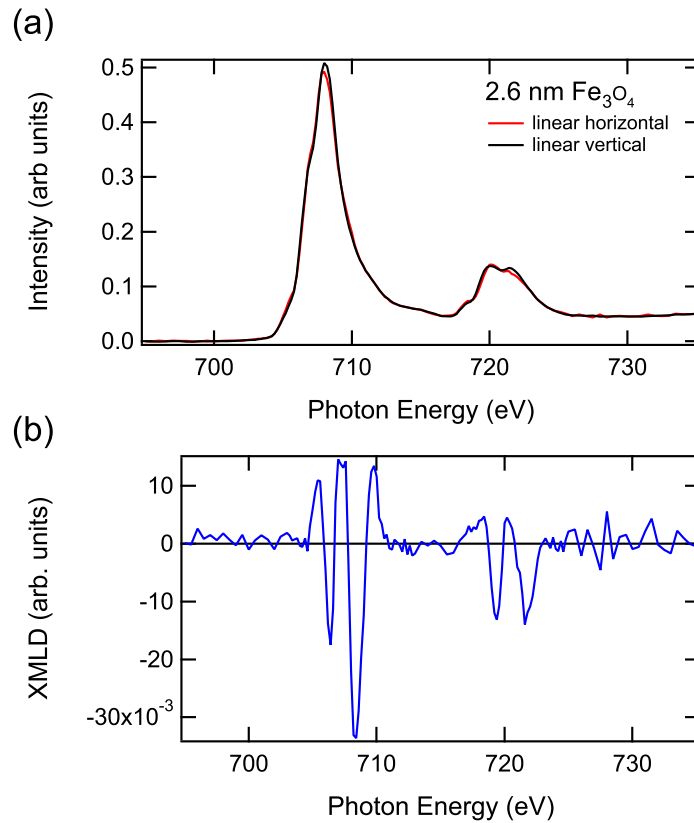


Figure 7.7: The Fe $L_{2,3}$ XAS and XMLD spectra of a 2.6 nm Fe_3O_4 film on BaTiO_3 measured with constant magnetization and two different polarizations of light.

intensities in the same film shows that the XMLD intensity is of similar magnitude in comparison to XMCD.

The magnetic XMLD effect in Fe_3O_4 arises from the preferential alignment of the ferrimagnetically coupled spins perpendicular to the film surface. However, with the present measurement type, it is impossible to exactly comment whether the signal is magnetic or due to X-ray natural linear dichroism (XNLD), an effect which stems from the dependence of the X-ray absorption intensity on E-vector orientation which is entirely determined by the spatial distribution of the empty valence states [16]. In order to confirm that the signal is magnetic, measurements using a fixed polarization along the hard or easy axis and the rotation of the magnetic axis, will be helpful. However, if we assume a cubic symmetry for the film, the signal can be attributed to purely magnetic origin [16]. Since Fe_3O_4 is known to possess a cubic crystallographic symmetry, the XMLD signal shown in Fig. 7.7 can be attributed to purely magnetic origin and not to XNLD.

The XMLD spectrum shows characteristic features as those observed for Fe_3O_4 film on $\text{SrTiO}_3(001)$ [146]. It consists of multiplet features at the L_2 and L_3 edges which changes according to the anisotropy of the sample. Similarity in XMLD features with [146] helps to identify the film as Fe_3O_4 .

7.4 Conclusions

The formation of Fe_3O_4 thin films on $\text{BaTiO}_3(001)$ single crystal surfaces grown by reactive metal oxidation is demonstrated with the help of X-ray absorption spectroscopy. The Fe $L_{2,3}$ and O K edges XAS measurements reveal similar spectral features in the film as that of single crystal Fe_3O_4 . The interface effects monitored by Ti $L_{2,3}$ and Ba $M_{4,5}$ edges XAS also do not show pronounced differences in peaks indicating only negligible changes at the interface.

The magnetic properties of the as prepared thin films have been investigated using XMCD and XMLD. The XMCD spectra have been recorded after preparation at 573 K and the XMCD L_3 edge peak ratios of the Fe_3O_4 film annealed to 673 K are found to be reversed after annealing to 873 K. The peak ratios of 873 K post annealed Fe $L_{2,3}$ XMCD spectra resemble those of reported Fe_3O_4 layers. This is attributed to the redistribution of cation site occupancies and resultant structural order due to annealing. The presence of theoretical and experimental spectra of Fe_3O_4 on different substrates is used to understand the different site occupancies in the XMCD spectra.

The magnetic anisotropy measurements have been performed by changing the azimuthal angle which shows higher intensities of the XMCD features along the $[110]$ direction of BaTiO_3 compared to the $[100]$ direction. This is contrary to the thick Fe_3O_4 layers on $\text{SrTiO}_3(001)$, where a four fold anisotropy with an easy axis parallel to the $[100]$ and the $[010]$ directions is obtained. This difference may be contributed by the growth mode, a uniaxial anisotropy for the thin films or strain induced magnetoelastic interactions. The evolution of magnetism with thickness is demonstrated by the increase in the XMCD intensity within the range 1.4- 2.6 nm. The analysis of the thickness dependent XMCD signal indicates the possible presence of another iron oxide layer such as Fe_2O_3 at the surface formed due to a higher oxygen pressure. The magnetic moments were calculated for the measurements in the $[110]$ direction of BaTiO_3 . The spin moment is $0.47\mu_B/\text{Fe atom}$, which is less than the published value of $0.8\mu_B/\text{Fe atom}$ for thick films. This reduction is ascribed to the measurements away from the magnetization saturation as well as measurements being away from the magnetic easy axis. The XMLD spectra complement the results from XMCD measurements which helps in the confirmation of the layer stoichiometry as Fe_3O_4 .

8 Summary and future perspectives

The magnetic properties, the growth and the interface effects of Fe and Fe₃O₄ ultrathin films on BaTiO₃(001) substrates are investigated within the framework of this thesis.

The first part of the thesis focuses on the investigations of growth, changes to the interface and the magnetic properties of ultrathin Fe films on well characterized BaTiO₃(001) single crystal surfaces. Fe ultrathin films have been grown on a well ordered, slightly oxygen deficient surface of BaTiO₃(001) obtained after the surface preparations. A sharp interface between BaTiO₃ and Fe is observed owing to the presence of oxygen vacancies at the BaTiO₃ surface. The thickness and the angle dependent investigations of the magnetic properties unravel three distinct regions of ferromagnetic evolution, namely a non-ferromagnetic region, an intermediate ferromagnetic region and a fully saturated ferromagnetic region. The non-ferromagnetic region (upto 6 MLE) is correlated to the possible growth mode of Fe as islands which agrees well with the absence of LEED spots and long range order in that region. An in-plane spin reorientation transition from the [110] to the [100] direction of Fe is observed at a film thickness of 6.7 MLE. This SRT is described by a simple approach which takes the interface interaction of Fe-Ti and the spin-orbit coupling into consideration. The effect of the substrate on the magnetic properties of Fe ultrathin films is hence established through these results. The spin as well as the orbital moments estimated for different directions show an enhancement of the orbital moment especially in the thin layers which is attributed to the reduction in symmetry at surfaces. These results also prove that the XMCD spectroscopy can be successfully employed to identify the magnetic contributions such as the anisotropy and the magnetic moments.

In the second part of the thesis, the investigations of the magnetic properties and the film morphology as a function of annealing temperature are carried out. Annealing of the as grown Fe films result in the formation of ordered, directional nanoislands having a diameter 150 nm through self assembly. The reduction of the BaTiO₃ surface helps to understand the absence of the interface oxidation after annealing. The magnetic properties reveal changes in the coercivity which rises from 6.4 Oe to 115 Oe upon annealing to 973 K, the magnetization which decreases to 50% of the value after 973 K annealing and the magnetic moment which reduces to 40% upon annealing to 773 K. These changes are discussed based on the assumption of the presence of fine structures such as vortices. In addition to the changes in magnitude, the shape of the MOKE loop became rounded which is correlated to the distribution in the particle size. The importance of initial film thickness and annealing temperature on the faceting of metal

films on oxide substrates is demonstrated. It is revealed that control over the desired morphology and properties can be achieved in the self assembly process by controlling the annealing temperature, the duration of annealing and the initial film thickness.

The third part describes the magnetic properties of Fe ultrathin films on BaTiO₃(100) layers which possess a bulk-like electronic structure. Fe films have been grown on BaTiO₃(100) layers on Pt(100) by e-beam evaporation. Similar to the single crystal BaTiO₃(001) substrates, the interface between Fe and BaTiO₃ layers is found to be an abrupt one, possibly owing to the slight reduction of the BaTiO₃ surface layers. The thickness and the azimuthal angle dependent investigations of magnetic properties of these Fe films demonstrate an in-plane magnetic anisotropy with a ferromagnetic onset from 5.5 MLE onwards. Ferromagnetism evolves through three regions, a non-ferromagnetic region below 5.5 MLE, an intermediate ferromagnetic region till 8.5 MLE and a saturation ferromagnetic region thereafter. Similar to the Fe layers on BaTiO₃(001) single crystal substrates, an in-plane SRT from [110] to [100] direction of Fe is observed with increasing Fe layer thickness. Magnetic moments calculated according to the sum rules reveal an enhancement in the orbital moment compared to bulk Fe which helps in ascribing the SRT to a spin-orbit coupling driven magnetic anisotropy change at the interface due to Fe-Ti interactions. To conclude, the magnetic properties of Fe on BaTiO₃ layers are found to be in agreement with those from the Fe on BaTiO₃ single crystals.

In the fourth and final part, the growth of Fe₃O₄ thin films on the BaTiO₃(001) single crystal surfaces by reactive metal oxidation and the magnetic properties of the as grown layers are elucidated. The dependence of perfect stoichiometry of the Fe₃O₄ on the annealing temperature as well as the oxygen pressure is demonstrated and reveals a redistribution of the cation site occupancies and resultant structural order due to annealing. The azimuthal angle and the thickness dependent magnetic measurements indicate the presence of a magnetic anisotropy in the thin layers with a preference to the [110] direction of BaTiO₃ compared to the [100] direction. Magnetism is seen to evolve through a non-magnetic region followed by a ferrimagnetic region. The magnetic moments were calculated for the measurements in the [110] direction of BaTiO₃. A reduction in the spin moment compared to the published values of bulk Fe₃O₄ is obtained and is ascribed to the measurements away from the magnetization saturation thickness as well as measurements away from the magnetic easy axis.

On the whole, these results help to identify the strong influence of morphology, growth and substrates on the magnetic properties by quantifying the orbital and the spin magnetic moments. This thesis also succeeds in establishing the magnetic properties of the ferromagnetic and the ferrimagnetic ultrathin films on the ferroelectric substrates. A thorough characterization of the BaTiO₃ helps in understanding the interface effects, for example, oxidation. The effect of the substrate and the dimensionality factors play a major role in the magnetic properties which is demonstrated by the in-plane spin reorientation transition in the Fe ultrathin films and the magnetic anisotropy in

the Fe_3O_4 thin films.

To conclude, the investigations discussed in this thesis have established the fundamental understanding of the interface and the magnetic properties of systems which hold a strong promise for further applications. The knowledge of the interface and magnetic properties can be successfully employed towards future investigations involving these systems for applications. For instance, BaTiO_3 layers can be effectively used for polarization switching studies using small voltages as well as for multiferroic applications.

Appendix : Units

The use of SI units is generally preferred. However, in literature, the magnetic field has been expressed in various units. The SI unit of magnetic-field strength or magnetic-flux density (B) is Tesla, denoted as T. Sometimes, this unit is used to express the magnetic field H . In CGS system of units, Oersted, denoted as Oe, is the unit of magnetic field H . To enable an easy comparison of the results in this thesis with literature, Oersted as well as Tesla are used to express the magnetic field.

Literature

- [1] G. SCHÜTZ, W. WAGNER, W. WILHELM, P. KIENLE, R. ZELLER, R. FRAHM, and G. MATERLIK: *Absorption of circularly polarized X- rays in iron*, Phys. Rev. Lett., 58:737–740, 1987. [11](#)
- [2] C. T. CHEN, N. V. SMITH, and F. SETTE: *Exchange, spin-orbit, and correlation effects in the soft X-ray magnetic-circular-dichroism spectrum of nickel*, Phys. Rev. B, 43:6785–6787, 1991. [11](#)
- [3] Y. WU, J. STÖHR, B. D. HERMSMEIER, M. G. SAMANT, and D. WELLER: *Enhanced orbital magnetic moment on Co atoms in Co/Pd multilayers: A magnetic circular x-ray dichroism study*, Phys. Rev. Lett., 69:2307–2310, 1992. [11](#)
- [4] J. STÖHR: *X-ray magnetic circular dichroism spectroscopy of transition metal thin films*, J. Electron. Spectrosc. Relat. Phenom., 75(0):253 – 272, 1995. [11](#)
- [5] C. T. CHEN, Y. U. IDZERDA, H.-J. LIN, N. V. SMITH, G. MEIGS, E. CHABAN, G. H. HO, E. PELLEGRIN, and F. SETTE: *Experimental Confirmation of the X-Ray Magnetic Circular Dichroism Sum Rules for Iron and Cobalt*, Phys. Rev. Lett., 75:152–155, 1995. [11](#), [22](#), [23](#), [50](#), [54](#), [55](#), [56](#), [57](#), [61](#), [85](#), [86](#), [98](#), [99](#), [100](#), [101](#)
- [6] D. WELLER, J. STÖHR, R. NAKAJIMA, A. CARL, M. G. SAMANT, C. CHAPPERT, R. MÉGY, P. BEAUVILLAIN, P. VEILLET, and G. A. HELD: *Microscopic Origin of Magnetic Anisotropy in Au/Co/Au Probed with X-Ray Magnetic Circular Dichroism*, Phys. Rev. Lett., 75:3752–3755, 1995. [11](#), [60](#)
- [7] J. STÖHR: *Exploring the microscopic origin of magnetic anisotropies with X-ray magnetic circular dichroism (XMCD) spectroscopy*, J. Magn. Magn. Mater., 200(1-3):470 – 497, 1999. [11](#)
- [8] C.-G. DUAN, S. S. JASWAL, and E. Y. TSYMBAL: *Predicted Magnetoelectric Effect in Fe/BaTiO₃ Multilayers: Ferroelectric Control of Magnetism*, Phys. Rev. Lett., 97:047201, 2006. [11](#), [38](#), [40](#), [48](#), [62](#), [68](#)
- [9] S. SAHOO, S. POLISETTY, C.-G. DUAN, S. S. JASWAL, E. Y. TSYMBAL, and C. BINEK: *Ferroelectric control of magnetism in BaTiO₃/Fe heterostructures via interface strain coupling*, Phys. Rev. B, 76:092108, 2007. [11](#), [33](#), [38](#), [66](#), [86](#)

- [10] M. FECHNER, I. V. MAZNICHENKO, S. OSTANIN, A. ERNST, J. HENK, P. BRUNO, and I. MERTIG: *Magnetic phase transition in two-phase multiferroics predicted from first principles*, Phys. Rev. B, 78:212406, 2008. [12](#), [38](#), [39](#), [40](#), [44](#), [48](#), [58](#), [68](#)
- [11] S. BOREK, I. V. MAZNICHENKO, G. FISCHER, W. HERGERT, I. MERTIG, A. ERNST, S. OSTANIN, and A. CHASSÉ: *First-principles calculation of x-ray absorption spectra and x-ray magnetic circular dichroism of ultrathin Fe films on BaTiO₃(001)*, Phys. Rev. B, 85:134432, 2012. [12](#), [21](#), [38](#), [57](#), [58](#)
- [12] S. GEPRÄGS, A. BRANDLMAIER, M. OPEL, R. GROSS, and S. T. B. GOENNENWEIN: *Electric field controlled manipulation of the magnetization in Ni/BaTiO₃ hybrid structures*, Appl. Phys. Lett., 96(14):142509, 2010. [12](#), [89](#)
- [13] J. LEE, N. SAI, T. CAI, Q. NIU, and A. A. DEMKOV: *Interfacial magnetoelectric coupling in tricomponent superlattices*, Phys. Rev. B, 81:144425, 2010. [12](#), [90](#)
- [14] M. K. NIRANJAN, J. P. VELEV, C.-G. DUAN, S. S. JASWAL, and E. Y. TSYMBAL: *Magnetoelectric effect at the Fe₃O₄/BaTiO₃ (001) interface: A first-principles study*, Phys. Rev. B, 78:104405, 2008. [12](#), [35](#), [105](#), [106](#)
- [15] F. HIPPERT: *Neutron and X-ray Spectroscopy*, Grenoble Sciences, Springer, 2006. [16](#), [17](#), [18](#), [19](#), [20](#), [29](#)
- [16] J. STÖHR and H. SIEGMANN: *Magnetism: from fundamentals to nanoscale dynamics*, Springer series in solid-state sciences, Springer, 2006. [19](#), [20](#), [21](#), [24](#), [54](#), [111](#), [115](#)
- [17] B. T. THOLE, P. CARRA, F. SETTE, and G. VAN DER LAAN: *X-ray circular dichroism as a probe of orbital magnetization*, Phys. Rev. Lett., 68:1943–1946, 1992. [21](#)
- [18] P. CARRA, B. T. THOLE, M. ALTARELLI, and X. WANG: *X-ray circular dichroism and local magnetic fields*, Phys. Rev. Lett., 70:694–697, 1993. [21](#), [22](#)
- [19] R. WU and A. J. FREEMAN: *Limitation of the Magnetic-Circular-Dichroism Spin Sum Rule for Transition Metals and Importance of the Magnetic Dipole Term*, Phys. Rev. Lett., 73:1994–1997, 1994. [22](#), [55](#)
- [20] G. ERTL and J. KÜPPERS: *Low energy electrons and surface chemistry*, VCH, 1985. [30](#), [48](#), [76](#)
- [21] K. SAWHNEY, F. SENF, M. SCHEER, F. SCHÄFERS, J. BAHRDT, A. GAUPP, and W. GUDAT: *A novel undulator-based PGM beamline for circularly polarised synchrotron radiation at BESSY II*, Nucl. Instr. Meth. Phys. Res. Section A: Accelerators, Spectrometers, Detectors and Associated Equipment, 390(3):395 – 402, 1997. [31](#), [32](#)

- [22] T. MATSUMOTO, H. TANAKA, T. KAWAI, and S. KAWAI: *STM-imaging of a SrTiO₃(100) surface with atomic-scale resolution*, Surf. Sci., 278(3):L153 – L158, 1992. [34](#)
- [23] H. TANAKA, T. MATSUMOTO, T. KAWAI, and S. KAWAI: *Interaction of oxygen vacancies with O₂ on a reduced SrTiO₃(100) $\sqrt{5} \times \sqrt{5}$ -R26.6° surface observed by STM*, Surf. Sci., 318(1-2):29 – 38, 1994. [34](#)
- [24] S. FÖRSTER, M. HUTH, K.-M. SCHINDLER, and W. WIDDRA: *Epitaxial BaTiO₃(100) films on Pt(100): A low-energy electron diffraction, scanning tunneling microscopy, and x-ray photoelectron spectroscopy study*, J. Chem. Phys., 135(10):104701, 2011. [34](#), [90](#)
- [25] N. SPALDIN: *Magnetic Materials: Fundamentals and Device Applications*, Cambridge University Press, 2003. [34](#), [58](#)
- [26] M. WUTTIG and X. LIU: *Ultrathin Metal Films: Magnetic and Structural Properties*, Springer Tracts in Modern Physics, Springer, 2010. [34](#), [57](#), [61](#), [80](#)
- [27] E. J. W. VERWEY: *Electronic Conduction of Magnetite (Fe₃O₄) and its Transition Point at Low Temperatures*, Nature, 144:327–328, 1939. [35](#)
- [28] J. P. WRIGHT, J. P. ATTFIELD, and P. G. RADAELLI: *Charge ordered structure of magnetite Fe₃O₄ below the Verwey transition*, Phys. Rev. B, 66:214422, 2002. [35](#)
- [29] F. WALZ: *The Verwey transition - a topical review*, J. Phys.: Condens. Matter, 14(12):R285, 2002. [35](#), [111](#)
- [30] J. GARCÍA and G. SUBÍAS: *The Verwey transition-a new perspective*, J. Phys.: Condens. Matter, 16(7):R145, 2004. [35](#), [111](#)
- [31] R. PENTCHEVA, W. MORITZ, J. RUNDGREN, S. FRANK, D. SCHRUPP, and M. SCHEFFLER: *A combined DFT/LEED-approach for complex oxide surface structure determination: Fe₃O₄(001)*, Surf. Sci., 602(7):1299 – 1305, 2008. [36](#)
- [32] M. FONIN, R. PENTCHEVA, Y. S. DEDKOV, M. SPERLICH, D. V. VYALIKH, M. SCHEFFLER, U. RÜDIGER, and G. GÜNTHERODT: *Surface electronic structure of the Fe₃O₄(100): Evidence of a half-metal to metal transition*, Phys. Rev. B, 72:104436, 2005. [36](#)
- [33] H. SCHMID: *Multi-ferroic magnetoelectrics*, Ferroelectrics, 162(1):317–338, 1994. [37](#)
- [34] N. HUR, S. PARK, P. A. SHARMA, J. S. AHN, S. GUHA, and S.-W. CHEONG: *Electric polarization reversal and memory in a multiferroic material induced by magnetic fields*, Nature, 429(6990):392–395, 2004. [37](#), [89](#)

- [35] B. K. PONOMAREV, S. A. IVANOV, Y. F. POPOV, V. D. NEGRIL, and B. S. RED'KIN: *Magnetoelectric properties of some rare earth molybdates*, *Ferroelectrics*, 161(1):43–48, 1994. [37](#)
- [36] W. EERENSTEIN, N. D. MATHUR, and J. F. SCOTT: *Multiferroic and magnetoelectric materials*, *Nature*, 442(7104):759–765, 2006. [37](#)
- [37] P. DEBYE: *Z. Phys.*, 36:300, 1926. [37](#)
- [38] P. CURIE: *J. Physique*, 3:393, 1894. [37](#)
- [39] T. H. E. LAHTINEN, Y. SHIRAHATA, L. YAO, K. J. A. FRANKE, G. VENKATIAH, T. TANIYAMA, and S. VAN DIJKEN: *Alternating domains with uniaxial and biaxial magnetic anisotropy in epitaxial Fe films on BaTiO₃*, *Appl. Phys. Lett.*, 101(26):262405, 2012. [38](#), [43](#), [62](#), [65](#)
- [40] M. KAMARATOS, D. VLACHOS, and S. D. FOULIAS: *Development and characterization of Fe ultrathin films on the SrTiO₃ (100) surface*, *J. Phys.: Condens. Matter*, 20(31):315009, 2008. [38](#), [49](#), [51](#)
- [41] F. SILLY and M. R. CASTELL: *Fe nanocrystal growth on SrTiO₃(001)*, *Appl. Phys. Lett.*, 87(6):063106, 2005. [38](#), [52](#), [72](#), [76](#)
- [42] P. TORELLI, S. BENEDETTI, P. LUCHES, L. GRAGNANIELLO, J. FUJII, and S. VALERI: *Morphology-induced magnetic phase transitions in Fe deposits on MgO films investigated with XMCD and STM*, *Phys. Rev. B*, 79:035408, 2009. [38](#), [39](#), [49](#), [53](#), [54](#), [57](#), [61](#), [73](#), [99](#)
- [43] C. MARTÍNEZ BOUBETA, C. CLAVERO, J. M. GARCÍA-MARTÍN, G. ARMELLES, A. CEBOLLADA, L. BALCELLS, J. L. MENÉNDEZ, F. PEIRÓ, A. CORNET, and M. F. TONEY: *Coverage effects on the magnetism of Fe/MgO(001) ultrathin films*, *Phys. Rev. B*, 71:014407, 2005. [38](#)
- [44] C. TEODORESCU and D. LUCA: *Comparative study of magnetism and interface composition in Fe/GaAs(100) and Fe/InAs(100)*, *Surf. Sci.*, 600(18):4200 – 4204, 2006. [38](#)
- [45] L. HAO-LIANG, H. WEI, D. HAI-FENG, F. YA-PENG, W. QIONG, Z. XIANG-QUN, Y. HAI-TAO, and C. ZHAO-HUA: *Magnetic anisotropy and magnetization reversal of ultrathin iron films with in-plane magnetization on Si(111) substrates*, *Chin. Phys. B*, 21, No. 7:077503, 2012. [38](#)
- [46] P. LUCHES, S. BENEDETTI, A. DI BONA, and S. VALERI: *Magnetic couplings and exchange bias in Fe/NiO epitaxial layers*, *Phys. Rev. B*, 81:054431, 2010. [38](#), [49](#), [53](#)
- [47] A. ARRANZ, V. PÉREZ-DIESTE, and C. PALACIO: *Growth, electronic properties and thermal stability of the Fe/Al₂O₃ interface*, *Surf. Sci.*, 521(1–2):77 – 83, 2002. [38](#)

- [48] D. H. KIM, H. J. LEE, G. KIM, Y. S. KOO, J. H. JUNG, H. J. SHIN, J.-Y. KIM, and J.-S. KANG: *Interface electronic structures of BaTiO₃@X nanoparticles (X= γ -Fe₂O₃, Fe₃O₄, α -Fe₂O₃, and Fe) investigated by XAS and XMCD*, Phys. Rev. B, 79:033402, 2009. [38](#), [105](#), [111](#)
- [49] S. BRIVIO, C. RINALDI, D. PETTI, R. BERTACCO, and F. SANCHEZ: *Epitaxial growth of Fe/BaTiO₃ heterostructures*, Thin Solid Films, 519(17):5804 – 5807, 2011. [38](#), [52](#), [71](#), [90](#), [94](#)
- [50] A. ZENKEVICH, R. MANTOVAN, M. FANCIULLI, M. MINNEKAEV, Y. MATVEYEV, Y. LEBEDINSKII, S. THIESS, and W. DRUBE: *Fe/BaTiO₃ interface: Band alignment and chemical properties*, Appl. Phys. Lett., 99(18):182905, 2011. [38](#), [52](#), [71](#)
- [51] S. SAKSHATH, S. V. BHAT, P. S. A. KUMAR, D. SANDER, and J. KIRSCHNER: *Enhancement of uniaxial magnetic anisotropy in Fe thin films grown on GaAs(001) with an MgO underlayer*, J. Appl. Phys., 109(7):07C114, 2011. [39](#), [65](#)
- [52] Y. SHIRAHATA, T. NOZAKI, G. VENKATAIAH, H. TANIGUCHI, M. ITOH, and T. TANIYAMA: *Switching of the symmetry of magnetic anisotropy in Fe/BaTiO₃ heterostructures*, Appl. Phys. Lett., 99(2):022501, 2011. [39](#), [86](#)
- [53] C. YU, M. J. PECHAN, S. SRIVASTAVA, C. J. PALMSTROM, M. BIEGASLSKI, C. BROOKS, and D. SCHLOM: *Ferromagnetic resonance in ferromagnetic/ferroelectric Fe/BaTiO₃/SrTiO₃(001)*, J. Appl. Phys., 103(7):07B108, 2008. [39](#)
- [54] C. HAGENDORF: *Oberflächenphysikalische Untersuchungen an ein- und polykristallinem BaTiO₃: Morphologie, atomare und elektronische Struktur*, Universitäts- und Landesbibliothek, 2000. [40](#), [44](#), [45](#)
- [55] A. M. KOLPAK, D. LI, R. SHAO, A. M. RAPPE, and D. A. BONNELL: *Evolution of the Structure and Thermodynamic Stability of the BaTiO₃(001) Surface*, Phys. Rev. Lett., 101:036102, 2008. [40](#), [41](#)
- [56] H. L. MEYERHEIM, A. ERNST, K. MOHSENI, I. V. MAZNICHENKO, S. OSTANIN, F. KLIMENTA, N. JEDRECY, W. FENG, I. MERTIG, R. FELICI, and J. KIRSCHNER: *BaTiO₃(001)-(2hbf \times 1): Surface Structure and Spin Density*, Phys. Rev. Lett., 108:215502, 2012. [40](#), [41](#)
- [57] N. ILES, F. FINOCCHI, and K. D. KHODJA: *A systematic study of ideal and double layer reconstructions of ABO₃ (001) surfaces (A = Sr, Ba; B = Ti, Zr) from first principles*, J. Phys.: Condens. Matter, 22(30):305001, 2010. [40](#), [41](#)
- [58] H. BANDO, T. SHIMITSU, Y. AIURA, Y. HARUYAMA, K. OKA, and Y. NISHIHARA: *Structure and electronic states on reduced BaTiO₃ (100) surface observed by*

- scanning tunneling microscopy and spectroscopy*, volume 14, pages 1060–1063, AVS, 1996. [41](#)
- [59] T. SHIMIZU, H. BANDO, Y. AIURA, Y. HARUYAMA, K. OKA, and Y. NISHIHARA: *Scanning Tunneling Microscopy and Spectroscopy Observation of Reduced BaTiO₃(100) Surface*, Jpn. J. Appl. Phys., 34(Part 2, No. 10A):L1305–L1308, 1995. [41](#)
- [60] J. M. P. MARTIREZ, E. H. MORALES, W. A. SAIDI, D. A. BONNELL, and A. M. RAPPE: *Atomic and Electronic Structure of the BaTiO₃(001) ($\sqrt{5} \times \sqrt{5}$) R26.6° Surface Reconstruction*, Phys. Rev. Lett., 109:256802, 2012. [41](#)
- [61] M. FECHNER, S. OStanIN, and I. MERTIG: *Effect of the surface polarization in polar perovskites studied from first principles*, Phys. Rev. B, 77:094112, 2008. [41](#)
- [62] B. CORD and R. COURTHS: *Electronic study of SrTiO₃(001) surfaces by photoemission*, Surf. Sci., 162(1–3):34 – 38, 1985. [41](#)
- [63] Y. LIN, A. E. BECERRA-TOLEDO, F. SILLY, K. R. POEPELMEIER, M. R. CASTELL, and L. D. MARKS: *The (2×2) reconstructions on the SrTiO₃(001) surface: A combined scanning tunneling microscopy and density functional theory study*, Surf. Sci., 605(17–18):L51 – L55, 2011. [41](#)
- [64] A. CHASSÉ, S. BOREK, K.-M. SCHINDLER, M. TRAUTMANN, M. HUTH, F. STEUDEL, L. MAKHOVA, J. GRÄFE, and R. DENECKE: *High-resolution x-ray absorption spectroscopy of BaTiO₃: Experiment and first-principles calculations*, Phys. Rev. B, 84:195135, 2011. [41](#), [42](#), [93](#)
- [65] F. M. F. DE GROOT, J. C. FUGGLE, B. T. THOLE, and G. A. SAWATZKY: *2p x-ray absorption of 3d transition-metal compounds: An atomic multiplet description including the crystal field*, Phys. Rev. B, 42:5459–5468, 1990. [41](#)
- [66] F. M. F. DE GROOT, J. FABER, J. J. M. MICHIELS, M. T. CZYŻYK, M. ABBATE, and J. C. FUGGLE: *Oxygen 1s x-ray absorption of tetravalent titanium oxides: A comparison with single-particle calculations*, Phys. Rev. B, 48:2074–2080, 1993. [41](#)
- [67] L. SORIANO, M. ABBATE, J. VOGEL, J. FUGGLE, A. FERNÁNDEZ, A. GONZÁLEZ-ELIPE, M. SACCHI, and J. SANZ: *Chemical changes induced by sputtering in TiO₂ and some selected titanates as observed by X-ray absorption spectroscopy*, Surf. Sci., 290(3):427 – 435, 1993. [41](#)
- [68] K. OKADA and A. KOTANI: *Theory of core level X-ray photoemission and photoabsorption in Ti compounds*, J. Electron Spectrosc. Relat. Phenom., 62(1–2):131 – 140, 1993. [41](#)

- [69] J. C. WOICIK, E. L. SHIRLEY, C. S. HELLBERG, K. E. ANDERSEN, S. SAMBASIVAN, D. A. FISCHER, B. D. CHAPMAN, E. A. STERN, P. RYAN, D. L. EDERER, and H. LI: *Ferroelectric distortion in SrTiO₃ thin films on Si(001) by X-ray absorption fine structure spectroscopy: Experiment and first-principles calculations*, Phys. Rev. B, 75:140103, 2007. [41](#), [43](#)
- [70] F. COTTON: *Chemical applications of group theory*, Interscience Publishers, 1963. [41](#)
- [71] L. SORIANO, M. ABBATE, A. FERNÁNDEZ, A. R. GONZÁLEZ-ELIPE, and J. M. SANZ: *Chemical Analysis of Ternary Ti Oxides using Soft X-ray Absorption Spectroscopy*, Surf. Interface Anal., 25(10):804–808, 1997. [43](#)
- [72] K. HORN, W. THEIS, J. J. PAGGEL, S. R. BARMAN, E. ROTENBERG, P. EBERT, and K. URBAN: *Core and valence level photoemission and photoabsorption study of icosahedral Al–Pd–Mn quasicrystals*, J. Phys.: Condens. Matter, 18(2):435, 2006. [44](#)
- [73] L. T. HUDSON, R. L. KURTZ, S. W. ROBEY, D. TEMPLE, and R. L. STOCKBAUER: *Photoelectron spectroscopic study of the valence and core-level electronic structure of BaTiO₃*, Phys. Rev. B, 47:1174–1180, 1993. [44](#), [45](#)
- [74] S. HÜFNER: *Photoelectron spectroscopy: principles and applications*, Springer series in solid-state sciences, Springer, 2003. [44](#)
- [75] A. G. THOMAS, W. R. FLAVELL, A. K. MALICK, A. R. KUMARASINGHE, D. TSOUTSOU, N. KHAN, C. CHATWIN, S. RAYNER, G. C. SMITH, R. L. STOCKBAUER, S. WARREN, T. K. JOHAL, S. PATEL, D. HOLLAND, A. TALEB, and F. WIAME: *Comparison of the electronic structure of anatase and rutile TiO₂ single-crystal surfaces using resonant photoemission and x-ray absorption spectroscopy*, Phys. Rev. B, 75:035105, 2007. [44](#)
- [76] E. BERTEL, R. STOCKBAUER, and T. E. MADEY: *Resonant electron emission in Ti and TiO₂*, Phys. Rev. B, 27:1939–1942, 1983. [45](#)
- [77] K. C. PRINCE, V. R. DHANAK, P. FINETTI, J. F. WALSH, R. DAVIS, C. A. MURYN, H. S. DHARIWAL, G. THORNTON, and G. VAN DER LAAN: *2p resonant photoemission study of TiO₂*, Phys. Rev. B, 55:9520–9523, 1997. [45](#), [46](#)
- [78] S. BENEDETTI, P. TORELLI, P. LUCHES, A. ROTA, and S. VALERI: *Morphology and chemical activity at the Au/NiO interface*, Surf. Sci., 600(18):4251 – 4255, 2006. [49](#)
- [79] X. GAO, D. QI, S. C. TAN, A. S. WEE, X. YU, and H. O. MOSER: *Thickness dependence of X-ray absorption and photoemission in Fe thin films on Si(001)*, J. Electron Spectrosc. Relat. Phenom., 151(3):199 – 203, 2006. [51](#)
- [80] S. TOUGAARD: *Universality Classes of Inelastic Electron Scattering Cross-sections*, Surf. Interface Anal., 25(3):137–154, 1997. [51](#)

- [81] R. NAKAJIMA, J. STÖHR, and Y. U. IDZERDA: *Electron-yield saturation effects in L-edge x-ray magnetic circular dichroism spectra of Fe, Co, and Ni*, Phys. Rev. B, 59:6421–6429, 1999. [52](#)
- [82] M. DÁVILA, D. ARVANITIS, J. DUNN, N. MÅRTENSSON, P. SRIVASTAVA, F. WILHELM, and K. BABERSCHKE: *Magnetic circular X-ray dichroism of metastable epitaxial Fe on Cu(1 0 0)*, J. Magn. Magn. Mater., 196-197:120 – 122, 1999. [52](#), [57](#)
- [83] I. VOBORNIK, U. MANJU, J. FUJII, F. BORGATTI, P. TORELLI, D. KRIZMANCIC, Y. S. HOR, R. J. CAVA, and G. PANACCIONE: *Magnetic Proximity Effect as a Pathway to Spintronic Applications of Topological Insulators*, Nano Letters, 11(10):4079–4082, 2011. [54](#)
- [84] Y. B. XU, M. TSELEPI, C. M. GUERTLER, C. A. F. VAZ, G. WASTLBAUER, J. A. C. BLAND, E. DUDZIK, and G. VAN DER LAAN: *Giant enhancement of orbital moments and perpendicular anisotropy in epitaxial Fe/GaAs(100)*, J. Appl. Phys., 89(11):7156–7158, 2001. [57](#), [66](#), [86](#), [99](#), [101](#)
- [85] A. FREEMAN and R. QUIAN WU: *Electronic structure theory of surface, interface and thin-film magnetism*, J. Magn. Magn. Mater., 100(1–3):497 – 514, 1991. [57](#)
- [86] J. H. DUNN, D. ARVANITIS, and N. MÅRTENSSON: *Magnetism of thin Fe films on Cu(100)*, Phys. Rev. B, 54:R11157–R11160, 1996. [57](#)
- [87] K. W. EDMONDS, C. BINNS, S. H. BAKER, S. C. THORNTON, C. NORRIS, J. B. GOEDKOOP, M. FINAZZI, and N. B. BROOKES: *Doubling of the orbital magnetic moment in nanoscale Fe clusters*, Phys. Rev. B, 60:472–476, 1999. [57](#), [99](#), [101](#)
- [88] J. T. LAU, A. FÖHLISCH, M. MARTINS, R. NIETUBYC, M. REIF, and W. WURTH: *Spin and orbital magnetic moments of deposited small iron clusters studied by x-ray magnetic circular dichroism spectroscopy*, New J. Phys., 4(1):98, 2002. [57](#), [101](#)
- [89] P. OHRESSER, G. GHIRINGHELLI, O. TJERNBERG, N. B. BROOKES, and M. FINAZZI: *Magnetism of nanostructures studied by x-ray magnetic circular dichroism: Fe on Cu(111)*, Phys. Rev. B, 62:5803–5809, 2000. [57](#), [101](#)
- [90] H. A. DÜRR, G. VAN DER LAAN, and B. T. THOLE: *Comment on “Microscopic Origin of Magnetic Anisotropy in Au/Co/Au Probed with X-Ray Magnetic Circular Dichroism”*, Phys. Rev. Lett., 76:3464–3464, 1996. [60](#)
- [91] L. R. SHELFORD, T. HESJEDAL, L. COLLINS-MCINTYRE, S. S. DHESI, F. MACCHEROZZI, and G. VAN DER LAAN: *Electronic structure of Fe and Co magnetic adatoms on Bi₂Te₃ surfaces*, Phys. Rev. B, 86:081304, 2012. [61](#)

-
- [92] J.-S. LEE, J. T. SADOWSKI, H. JANG, J.-H. PARK, J.-Y. KIM, J. HU, R. WU, and C.-C. KAO: *Interfacial nanostructure induced spin-reorientation transition in Ni/Fe/Ni/W(110)*, Phys. Rev. B, 83:144420, 2011. [61](#)
 - [93] E. ARENHOLZ, G. VAN DER LAAN, A. MCCLURE, and Y. IDZERDA: *Electronic and magnetic structure of Ga_xFe_{1-x} thin films*, Phys. Rev. B, 82:180405, 2010. [62](#), [102](#)
 - [94] G. VAN DER LAAN: *The role of the spin polarization in x-ray magnetic circular dichroism spectra of itinerant magnets*, J. Phys.: Condens. Matter, 9(18):L259, 1997. [62](#), [102](#)
 - [95] G. VAN DER LAAN: *Microscopic origin of magnetocrystalline anisotropy in transition metal thin films*, J. Phys.: Condens. Matter, 10(14):3239, 1998. [62](#), [102](#)
 - [96] L. BERGER: *Evidence for split bands in Ni-Fe from specific heat, g-factor, and magnetostriction data*, Physica B+C, 91(0):31 – 36, 1977. [62](#)
 - [97] G. BAYREUTHER, M. DUMM, B. UHL, R. MEIER, and W. KIPFERL: *Magnetocrystalline volume and interface anisotropies in epitaxial films: Universal relation and Néel's model (invited)*, J. Appl. Phys., 93(10):8230–8235, 2003. [62](#), [65](#), [102](#)
 - [98] R. HOLLINGER, M. ZOLFL, R. MOOSBUHLER, and G. BAYREUTHER: *In-plane spin reorientation transitions in epitaxial Fe(110)/GaAs(110) films*, J. Appl. Phys., 89(11):7136–7138, 2001. [62](#), [102](#)
 - [99] M. BROCKMANN, S. MIETHANER, R. ONDERKA, M. KOHLER, F. HIMMELHUBER, H. REGENSBURGER, F. BENSCH, T. SCHWEINBOCK, and G. BAYREUTHER: *In-plane spin reorientation transition in ultrathin epitaxial Fe(001) films*, J. Appl. Phys., 81(8):5047–5049, 1997. [62](#), [102](#)
 - [100] H. NISHIKAWA, E. HOUWMAN, H. BOSCHER, M. MATHEWS, D. H. A. BLANK, and G. RIJNDERS: *Rotation of the magnetic easy axis in $La_{0.67}Sr_{0.33}MnO_3$ thin film on $NdGaO_3(112)$* , Appl. Phys. Lett., 94(4):042502, 2009. [62](#)
 - [101] E. C. STONER and E. P. WOHLFARTH: *A Mechanism of Magnetic Hysteresis in Heterogeneous Alloys*, Phil. Trans. R. Soc. A, Mathematical and Physical Sciences, 240(826):599–642, 1948. [63](#), [101](#)
 - [102] V. H. BABU, R. K. GOVIND, M. WELKE, K.-M. SCHINDLER, and R. DENECKE: *Interfacial uniaxial magnetic anisotropy and anisotropic spin-orbit coupling in ultrathin Fe layers on $BaTiO_3(001)$* , 2013, to be published. [63](#)
 - [103] STAMPANONI, M., VATERLAUS, A., AESCHLIMANN, M., MEIER, F., and PESCIA, D.: *Magnetic Properties of Epitaxial Iron films*, J. Phys. Colloques, 49:C8–1661–C8–1662, 1988. [65](#)

- [104] Y. Y. HUANG, C. LIU, and G. P. FELCHER: *Magnetization of ultrathin bcc Fe films on MgO*, Phys. Rev. B, 47:183–189, 1993. [65](#)
- [105] I. M. L. BILLAS, J. A. BECKER, A. CHÂTELAIN, and W. A. DE HEER: *Magnetic moments of iron clusters with 25 to 700 atoms and their dependence on temperature*, Phys. Rev. Lett., 71:4067–4070, 1993. [66](#)
- [106] N. ASHCROFT and N. MERMIN: *Solid state physics*, Science: Physics, Saunders College, 1976. [67](#)
- [107] J. GARCIA-BARRIOCANAL, J. CEZAR, F. BRUNO, P. THAKUR, N. BROOKES, C. UTFELD, A. RIVERA-CALZADA, S. GIBLIN, J. TAYLOR, J. DUFFY, S. DUGDALE, T. NAKAMURA, K. KODAMA, C. LEON, S. OKAMOTO, and J. SANTA-MARIA: *Spin and orbital Ti magnetism at LaMnO₃/SrTiO₃ interfaces*, Nat. Commun., 1:82–, 2010. [67](#)
- [108] H. CHOI, Y. HWANG, E.-K. LEE, and Y.-C. CHUNG: *Interface-dependent magnetic anisotropy of Fe/BaTiO₃: A first principles study*, J. Appl. Phys., 109(7):07D909, 2011. [68](#)
- [109] S. VALENCIA, A. CRASSOUS, L. BOCHER, V. GARCIA, X. MOYA, R. O. CHERIFI, C. DERANLOT, K. BOUZEHOUE, S. FUSIL, A. ZOBELLI, A. GLOTER, N. D. MATHUR, A. GAUPP, R. ABRUDAN, F. RADU, A. BARTHÉLÉMY, and M. BIBES: *Interface-induced room-temperature multiferroicity in BaTiO₃*, Nature Mater., 10(10):753–758, 2011. [68](#)
- [110] X.-Z. DING, L. HUANG, X. ZENG, S. LAU, B. TAY, W. CHEUNG, and S.P.WONG: *Catalytic chemical vapor deposition of vertically aligned carbon nanotubes on iron nanoislands formed from Fe⁺-implanted SiO₂ films*, Carbon, 42(14):3030 – 3033, 2004. [71](#)
- [111] S.-J. PARK, S. KIM, S. LEE, Z. G. KHIM, K. CHAR, and T. HYEON: *Synthesis and Magnetic Studies of Uniform Iron Nanorods and Nanospheres*, J. Am. Chem. Soc., 122(35):8581–8582, 2000. [71](#)
- [112] R. TANNER, I. GOLDFARB, M. CASTELL, and G. BRIGGS: *The evolution of Ni nanoislands on the rutile TiO₂(110) surface with coverage, heating and oxygen treatment*, Surf. Sci., 486(3):167 – 184, 2001. [71](#)
- [113] N. ROUGEMAILLE and A. K. SCHMID: *Self-organization and magnetic domain microstructure of Fe nanowire arrays*, J. Appl. Phys., 99(8):08S502, 2006. [72](#)
- [114] O. FRUCHART, M. ELEOUI, J. VOGEL, P. O. JUBERT, A. LOCATELLI, and A. BALLESTRAZZI: *Nanometers-thick self-organized Fe stripes: bridging the gap between surfaces and magnetic materials*, Appl. Phys. Lett., 84(8):1335–1337, 2004. [72](#)

- [115] P.-O. JUBERT, O. FRUCHART, and C. MEYER: *Growth and magnetism of epitaxial self-assembled Fe nanostructures on a Mo(110) surface*, J. Magn. Magn. Mater., 226-230, Part 2(0):1842 – 1844, 2001. [72](#), [87](#)
- [116] S. R. SPURGEON, J. D. SLOPPY, R. TAO, R. F. KLIE, S. E. LOFLAND, J. K. BALDWIN, A. MISRA, and M. L. TAHERI: *A study of the effect of iron island morphology and interface oxidation on the magnetic hysteresis of Fe-MgO (001) thin film composites*, J. Appl. Phys., 112(1):013905, 2012. [72](#), [87](#)
- [117] P. PALMBERG and P. E. INDUSTRIES: *Handbook of Auger electron spectroscopy: a reference book of standard data for identification and interpretation of Auger electron spectroscopy data*, Physical Electronics Industries, 1972. [73](#)
- [118] V. HENRICH: *Metal-oxide surfaces*, Progress in Surface Science, 50(1–4):77 – 90, 1995. [79](#)
- [119] V. E. HENRICH and P. COX: *The Surface Science of Metal Oxides*, Cambridge University Press, 1996. [79](#)
- [120] L. VITOS, A. RUBAN, H. SKRIVER, and J. KOLLÀR: *The surface energy of metals*, Surf. Sci., 411(1–2):186 – 202, 1998. [80](#)
- [121] U. DIEBOLD, J.-M. PAN, and T. E. MADEY: *Ultrathin metal film growth on TiO₂(110): an overview*, Surf. Sci., 331-333, Part B(0):845 – 854, 1995. [82](#)
- [122] J. SHEN, M.-T. LIN, J. GIERGIEL, C. SCHMIDTHALS, M. ZHARNIKOV, C. SCHNEIDER, and J. KIRSCHNER: *Annealing effect on morphology and magnetism of ultrathin films of Fe and Ni on Cu(100)*, J. Magn. Magn. Mater., 156(1-3):104 – 106, 1996. [86](#)
- [123] A. P. GUIMARÃES: *Principles of Nanomagnetism*, number 69 in NanoScience and Technology, Springer, Dordrecht, 2009. [86](#)
- [124] S. AGGARWAL, S. B. OGALE, C. S. GANPULE, S. R. SHINDE, V. A. NOVIKOV, A. P. MONGA, M. R. BURR, R. RAMESH, V. BALLAROTTO, and E. D. WILLIAMS: *Oxide nanostructures through self-assembly*, Appl. Phys. Lett., 78(10):1442–1444, 2001. [87](#)
- [125] M. DESAI, S. PRASAD, N. VENKATARAMANI, I. SAMAJDAR, A. K. NIGAM, N. KELLER, R. KRISHNAN, E. M. BAGGIO-SAITOVITCH, B. R. PUJADA, and A. ROSSI: *Anomalous variation of coercivity with annealing in nanocrystalline NiZn ferrite films*, J. Appl. Phys., 91(10):7592–7594, 2002. [87](#)
- [126] W. WULFHEKEL, F. ZAVALICHE, R. HERTEL, S. BODEA, G. STEIERL, G. LIU, J. KIRSCHNER, and H. P. OEPEN: *Growth and magnetism of Fe nanostructures on W(001)*, Phys. Rev. B, 68:144416, 2003. [87](#)

- [127] Y. ZHANG, J. LIU, X. H. XIAO, T. C. PENG, C. Z. JIANG, Y. H. LIN, and C. W. NAN: *Large reversible electric-voltage manipulation of magnetism in NiFe/BaTiO₃ heterostructures at room temperature*, J. Phys. D: Appl. Phys., 43(8):082002, 2010. [89](#)
- [128] J. K. G. PANITZ and C.-C. HU: *Radio-frequency-sputtered tetragonal barium titanate films on silicon*, J. Vac. Sci. Technol., 16(2):315–318, 1979. [90](#)
- [129] K. SREENIVAS and A. MANSINGH: *RF-sputtered transparent ferroelectric thin-films of barium-titanate (BaTiO₃)*, IEEE Trans. Ultrason., Ferroelectr., Freq. Control, 33(6):821, 1986. [90](#)
- [130] E. LEE, F. PONTES, E. LEITE, E. LONGO, J. VARELA, E. ARAUJO, and J. EIRAS: *Preparation and properties of ferroelectric BaTiO₃ thin films produced by the polymeric precursor method*, J. Mater. Sci. Lett., 19:1457–1459, 2000. [90](#)
- [131] M.-C. WANG, F.-Y. HSIAO, C.-S. HSI, and N.-C. WU: *Crystal structure and ferroelectricity of nanocrystalline barium titanate thin films*, J. Cryst. Growth, 246(1–2):78–84, 2002. [90](#)
- [132] Y. MATSUI, M. OKUYAMA, M. NODA, and Y. HAMAKAWA: *A study of electronic states near the interface in ferroelectric - semiconductor heterojunction prepared by RF sputtering of PbTiO₃*, Appl. Phys. A Mater. Sci. Process., 28(3):161–166, 1982. [90](#)
- [133] T. L. ROSE, E. M. KELLIHER, A. N. SCOVILLE, and S. E. STONE: *Characterization of rf-sputtered BaTiO₃ thin films using a liquid electrolyte for the top contact*, J. Appl. Phys., 55(10):3706–3714, 1984. [90](#)
- [134] P. NACHIMUTHU, S. THEVUTHASAN, V. SHUTTHANANDAN, E. M. ADAMS, W. J. WEBER, B. D. BEGG, D. K. SHUH, D. W. LINDLE, E. M. GULLIKSON, and R. C. C. PERERA: *Near-edge x-ray absorption fine-structure study of ion-beam-induced phase transformation in Gd₂(Ti_{1-y}Zr_y)₂O₇*, J. Appl. Phys., 97(3):033518, 2005. [92](#)
- [135] F. M. F. DE GROOT, J. C. FUGGLE, B. T. THOLE, and G. A. SAWATZKY: *L_{2,3} x-ray-absorption edges of d⁰ compounds: K⁺, Ca²⁺, Sc³⁺, and Ti⁴⁺ in O_h (octahedral) symmetry*, Phys. Rev. B, 41:928–937, 1990. [92](#)
- [136] J. P. CROCOMBETTE and F. JOLLET: *Ti 2p X-ray absorption in titanium dioxides (TiO₂): the influence of the cation site environment*, J. Phys.: Condens. Matter, 6(49):10811, 1994. [93](#)
- [137] J. C. JAN, K. P. K. KUMAR, J. W. CHIOU, H. M. TSAI, H. L. SHIH, H. C. HSUEH, S. C. RAY, K. ASOKAN, W. F. PONG, M.-H. TSAI, S. Y. KUO, and W. F. HSIEH: *Effect of the Ca content on the electronic structure of Pb_{1-x}Ca_xTiO₃ perovskites*, Appl. Phys. Lett., 83(16):3311–3313, 2003. [93](#)

- [138] V. R. MASTELARO, P. P. NEVES, S. R. DE LAZARO, E. LONGO, A. MICHALOWICZ, and J. A. EIRAS: *Electronic structure of $Pb_{1-x}La_xTiO_3$ ferroelectric materials from Ti 2p and O 1s soft x-ray absorption spectroscopy*, J. Appl. Phys., 99(4):044104, 2006. [93](#)
- [139] K. HE, L. J. ZHANG, X. C. MA, J. F. JIA, Q. K. XUE, and Z. Q. QIU: *Growth and magnetism of ultrathin Fe films on Pt(100)*, Phys. Rev. B, 72:155432, 2005. [102](#)
- [140] J. J. VERSLUIJS, M. A. BARI, and J. M. D. COEY: *Magnetoresistance of Half-Metallic Oxide Nanocontacts*, Phys. Rev. Lett., 87:026601, 2001. [105](#)
- [141] S. A. WOLF, D. D. AWSCHALOM, R. A. BUHRMAN, J. M. DAUGHTON, S. VON MOLNÁR, M. L. ROUKES, A. Y. CHITCHELKANOVA, and D. M. TREGER: *Spintronics: A Spin-Based Electronics Vision for the Future*, Science, 294(5546):1488–1495, 2001. [105](#)
- [142] H.-J. KIM, J.-H. PARK, and E. VESCOVO: *Oxidation of the Fe(110) surface: An $Fe_3O_4(111)/Fe(110)$ bilayer*, Phys. Rev. B, 61:15284–15287, 2000. [105](#), [106](#), [107](#), [108](#), [111](#)
- [143] Y. ZHAI, Z. C. HUANG, Y. FU, C. NI, Y. X. LU, Y. B. XU, J. WU, and H. R. ZHAI: *Anisotropy of ultrathin epitaxial Fe_3O_4 films on GaAs(100)*, J. Appl. Phys., 101(9):09D126, 2007. [105](#), [106](#), [112](#)
- [144] Y. X. LU, J. S. CLAYDON, Y. B. XU, S. M. THOMPSON, K. WILSON, and G. VAN DER LAAN: *Epitaxial growth and magnetic properties of half-metallic Fe_3O_4 on GaAs(100)*, Phys. Rev. B, 70:233304, 2004. [105](#), [106](#), [110](#)
- [145] D. J. HUANG, C. F. CHANG, H.-T. JENG, G. Y. GUO, H.-J. LIN, W. B. WU, H. C. KU, A. FUJIMORI, Y. TAKAHASHI, and C. T. CHEN: *Spin and Orbital Magnetic Moments of Fe_3O_4* , Phys. Rev. Lett., 93:077204, 2004. [106](#), [107](#), [110](#), [114](#)
- [146] E. ARENHOLZ, G. VAN DER LAAN, R. V. CHOPDEKAR, and Y. SUZUKI: *Anisotropic x-ray magnetic linear dichroism at the Fe $L_{2,3}$ edges in Fe_3O_4* , Phys. Rev. B, 74:094407, 2006. [106](#), [112](#), [114](#), [115](#)
- [147] H. F. TIAN, T. L. QU, L. B. LUO, J. J. YANG, S. M. GUO, H. Y. ZHANG, Y. G. ZHAO, and J. Q. LI: *Strain induced magnetoelectric coupling between magnetite and $BaTiO_3$* , Appl. Phys. Lett., 92(6):063507, 2008. [106](#), [112](#)
- [148] N. BERDUNOV, S. MURPHY, G. MARIOTTO, and I. V. SHVETS: *Atomically Resolved Spin-Dependent Tunneling on the Oxygen-Terminated $Fe_3O_4(111)$* , Phys. Rev. Lett., 93:057201, 2004. [106](#)

- [149] G. E. STERBINSKY, B. W. WESSELS, J.-W. KIM, E. KARAPETROVA, P. J. RYAN, and D. J. KEAVNEY: *Strain-driven spin reorientation in magnetite/barium titanate heterostructures*, Appl. Phys. Lett., 96(9):092510, 2010. [106](#)
- [150] T. J. REGAN: *XAS and microscopy study of ferro and antiferromagnetic films*, Dissertation, Stanford University, 2001. [107](#), [108](#)
- [151] T. J. REGAN, H. OHLDAG, C. STAMM, F. NOLTING, J. LÜNING, J. STÖHR, and R. L. WHITE: *Chemical effects at metal/oxide interfaces studied by x-ray-absorption spectroscopy*, Phys. Rev. B, 64:214422, 2001. [107](#), [108](#)
- [152] J. P. CROCOMBETTE, M. POLLAK, F. JOLLET, N. THROMAT, and M. GAUTIER-SOYER: *X-ray-absorption spectroscopy at the Fe $L_{2,3}$ threshold in iron oxides*, Phys. Rev. B, 52:3143–3150, 1995. [107](#)
- [153] K. KUEPPER, I. BALASZ, H. HESSE, A. WINIARSKI, K. C. PRINCE, M. MATTEUCCI, D. WETT, R. SZARGAN, E. BURZO, and M. NEUMANN: *Electronic and magnetic properties of highly ordered Sr_2FeMoO_6* , Phys. Status Solidi A, 201(15):3252–3256, 2004. [107](#), [108](#)
- [154] P. KUIPER, B. SEARLE, L.-C. DUDA, R. WOLF, and P. VAN DER ZAAG: *Fe $L_{2,3}$ linear and circular magnetic dichroism of Fe_3O_4* , J. Electron Spectrosc. Relat. Phenom., 86(1–3):107 – 113, 1997. [107](#), [110](#)
- [155] P. THAKUR, W. CHOI, K. CHAE, J.-Y. KIM, R. CHOUDHARY, S. TIWARI, R. PRAKASH, D. PHASE, and R. KUMAR: *X-ray Absorption Spectroscopic Studies of Pulsed-Laser-Deposited Thin Films of Fe_3O_4 on Si(111) Substrate*, J. Korean Phys. Soc., 53:3694–3698, 2008. [107](#), [108](#), [110](#), [111](#)
- [156] E. GOERING, M. LAFKIOTI, and S. GOLD: *Comment on “Spin and Orbital Magnetic Moments of Fe_3O_4 ”*, Phys. Rev. Lett., 96:039701, 2006. [110](#), [114](#)
- [157] P. MORRALL, F. SCHEDIN, G. S. CASE, M. F. THOMAS, E. DUDZIK, G. VAN DER LAAN, and G. THORNTON: *Stoichiometry of $Fe_{3-\delta}O_4(111)$ ultrathin films on Pt(111)*, Phys. Rev. B, 67:214408, 2003. [110](#), [111](#)
- [158] M. R. D. GUIRE, R. C. O’HANDLEY, and G. KALONJI: *The cooling rate dependence of cation distributions in $CoFe_2O_4$* , J. Appl. Phys., 65(8):3167–3172, 1989. [111](#)
- [159] P. HU, S. ZHANG, H. WANG, D. PAN, J. TIAN, Z. TANG, and A. A. VOLINSKY: *Heat treatment effects on Fe_3O_4 nanoparticles structure and magnetic properties prepared by carbothermal reduction*, J. Alloys Compd., 509(5):2316 – 2319, 2011. [113](#)
- [160] M. KALLMAYER, K. HILD, H. J. ELMERS, S. K. ARORA, H.-C. WU, R. G. S. SOFIN, and I. V. SHVETS: *Magnetic moment investigations of epitaxial magnetite thin films*, J. Appl. Phys., 103(7):07D715, 2008. [114](#)

Erklärung

Hiermit erkläre ich, dass ich gemäß dem § 5, Absatz 2b der Promotionsordnung der Mathematisch-Naturwissenschaftlichen-Fakultät der Martin-Luther-Universität Halle-Wittenberg vom 15.06.2008, die vorliegende Arbeit selbstständig und ohne fremde Hilfe verfasst, andere als die von mir angegebenen Quellen und Hilfsmittel nicht benutzt und die den benutzten Werken wörtlich oder inhaltlich entnommenen Stellen als solche kenntlich gemacht habe.

Halle (Saale), 08. Juli 2013

Remya Kunjuveettil Govind

Curriculum Vitae

Personal Details

Name:	Remya Kunjuveetil Govind
Date of birth:	06.03.1984
Place of birth:	Thiruvalla, Kerala, India
Nationality:	Indian
Marital status:	Single

Education

06/2008- present	PhD at Martin-Luther-Universität Halle-Wittenberg, Institut für Physik, Surface Science Group
12/2007-03/2008	M.Phil Nanoscience and Nanotechnology, University of Kerala (Discontinued)
06/2005-05/2007	M.Sc. Hydrochemistry, Cochin University of Science and Technology, Thesis title: Synthesis of ferromagnetic and ferroelectric nanoparticles, self-assembly and the study of their physical properties
07/2001-04/2004	B.Sc. Chemistry with Physics and Mathematics, University of Kerala
06/1999 -04/2001	Pre-Degree (12th), University of Calicut
06/1989-03/1999	S.S.L.C (10th), Board of Public Examinations, Kerala

Scholarships/Awards won

1. National Merit Scholarship under Government of India National Scholarship Scheme (1999 – 2000)
2. Summer Research Fellowship, Indian Academy of Sciences, 2006, Thesis title: A study of Dimethyl sulphide and dimethyl sulphoniopropionate in sediments
3. Second rank in M.Sc. course, Cochin University of Science and Technology, 2007
4. Indira Gandhi National Scholarship for Single Girl Child, 2005
5. International Max Planck Research School Halle PhD student

Conference contributions

1. The International Mittelwihl School on Synchrotron Radiation and Magnetism, 2012 (Poster)
2. DPG Spring meeting, Dresden 2011 (Talk)
3. International Workshop on Functionality of Oxide Interfaces and Multiferroic Materials, Monastery Irsee, 2010 (Poster)
4. IMPRS-SFB Workshop in Wittenberg, Fall 2009 (Poster)
5. DPG Spring meeting, Dresden 2009
6. IMPRS Workshop in Helfta, Fall 2008

Publications

1. R. K. Govind, V. Hari Babu, C.-T. Chiang, E. Magnano, F. Bondino, R. Denecke, K.-M. Schindler, Magnetic properties of self-assembled Fe nanoislands on BaTiO₃(001), J. Magn. Magn. Mater. (accepted)
2. R. K. Govind, Multiferroic and magnetoelectric thin films: Synthesis to Applications, (Patent review) Recent Patents on Materials Science, Bentham Science Publishers, 2013 (accepted)
3. V. H. Babu, R. K. Govind, M. Welke, K.-M. Schindler, R. Denecke, Interfacial uniaxial magnetic anisotropy and anisotropic spin-orbit coupling in ultrathin Fe layers on BaTiO₃(001), to be published

Halle (Saale), 08. July 2013

Acknowledgement

Although I am short of words to express my deep sense of gratitude to all those who have directly or indirectly contributed to this thesis, I am trying to figure out some of those persons who have influenced me a lot and left their footsteps for me to follow.

I am indebted to PD Dr. Karl-Michael Schindler, my research supervisor, without whose consent I would have never been able to do this project. I express my deep sense of gratitude to him for his excellent scientific support, valuable guidance, constant encouragement and advice. His craving for perfection and precision have inspired and influenced me.

I express my sincere gratitude to Prof. Dr. Wolf Widdra, Head of Surface Science Group, for giving me the opportunity to pursue the project in his research group. His excellent research attitude, vast knowledge and scientific discussions have helped me a lot. I am immensely thankful to Prof. Dr. J. Kirschner for providing the UHV chamber and all other facilities for research. He has set a model for youngsters with his in depth knowledge and uncompromising scientific precision. I am extremely grateful to Prof. Dr. Reinhard Denecke, for his constant help and support for the project. I have learned a lot of science from you and I highly appreciate this collaboration. Your energy levels and enthusiasm have inspired me.

I am sincerely thankful to Dr. V. Hari Babu for his help and support during the experiments and data analysis. I highly appreciate his passion and devotion to research. I am thankful to Dr. A. Chassè for the collaboration and scientific discussions. I thank all beamline staff, specially Willy Mahler, Birgit Zada, Federica Bondino, Elena Magnano, Marco Malvestuto and Gunnar Öhrwall, for their help and support during measurements. I am thankful to Martin Welke, Martin Trautmann, Joachim Graefe, Eric Kohl and L. Makhova for their association and co-operation during measurements. I am thankful to Stephan Borek for the scientific association. I thank Fikret Yildiz for his support during my initial days in lab.

I am very thankful to Stefan Förster for providing the BaTiO₃ thin film samples and his constant support whenever I was in trouble. I thank Cheng-Tien Chiang for his help for SEM measurements and scientific association. I am very grateful to Prof. Dr. H. Neddermeyer, Dr. Klaus Meinel and all past and present members of the surface science research group for the pleasant atmosphere, particularly to Benjamin Bochmann who was always ready to help me in troubleshooting network related problems.

The immense help in the preparation of samples is highly acknowledged and I thank Ralf Kulla, Mrs. H. Menge and F. Weiss for their technical assistance, help and support. The help from the workshops at MPI, Halle and MLU, Halle is also acknowledged.

I thank the former and present co-ordinators of IMPRS, Halle and my PhD mentor Dr. Arthur Ernst for their support. I wish to thank all members of IMPRS Halle for the friendly environment and my colleagues at MPI, Halle and MLU, Halle for the stimulating scientific discussions.

On a personal level, I thank all my teachers, friends and relatives for supporting me throughout these days. Special mention to Gaurav Gupta who readily performed XRD measurements for my samples. I am extremely thankful to my first standard teacher, Ms. Bhanumathy, who loved and encouraged me a lot. I wish to thank my parents - achan & amma and my grandfather - achachan for their blessings, love, care, support, encouragement and above all, for being with me through all my ups and downs. I remember my achan for his faith and confidence in me and I am sure that your values and morals will continue to guide me. Finally, I thank God Almighty, for the infinite invaluable gifts that have come to me.

Thank you ...